PANE Journal of Physics

Volume 02, Number 01, April 2026

ISSN: 3107-9342 (Online)

A Peer-reviewed Open Access Journal
Published by

Physics Academy of the North East

Editorial Board of PANE Journal of Physics

Table of Contents

1. *Robust strain-tolerant metallic phase in Cs-based halide perovskite $CsAsBr_3$* by Satyananda Chabungbam, Nathaniel Wansuk Majaw, Liang Bacheng Marak and Ibapyntngen Shyrkon 01

2. *Synthesis and characterization of oxide nanoparticles for its application in memristive devices* by Jyoti Prasad Roy Choudhury, Barnali Pathak, Nayan Mani Nath and Bikash Borah 07

3. *Light Scattering investigation of Black Turmeric (Curcuma caesia): a comparative study with established Mie theory* by Farhana Hussain and Sanchita Roy 15

4. *Multifunctional performance of PVA-PVP/ZnO nanocomposites: Optical, dielectric and AC conductivity analysis* by T. Suma Chanu, K. Jugeshwar Singh, K. Nomita Devi 22

5. *Enhanced photocatalytic actvity of MOF-derived ZnO nanoparticles for dye degradation* by Salam Jogita Chanu, L. Anju Chanu and K. Nomita Devi 33

6. *Etching characteristics of LR-115 type II films using percentage–track density* by Yubaraj Sharma, Budmiki Talang, Deveshwori Maibam and Aibanjop Pyngrope 42

7. *Exploring patterns in nuclear binding energy: isotopic, isotonic and isobaric variations* by Yubaraj Sharma 47

8. *Synthesis and Dielectric Properties Analysis of Polythiophene Nanoparticles* by Paragjyoti Chutia 62

ROBUST STRAIN-TOLERANT METALLIC PHASE IN Cs-BASED HALIDE PEROVSKITE $CsAsBr_3$

Satyananda Chabungbam*[1], Nathaniel Wansuk Majaw[1], Liang Bacheng Marak[1], and Ibapyntngen Shyrkon[1]

[1]*Department of Physics, Assam Don Bosco University, Tapesia Gardens - 782402, Assam, India*

*Corresponding Author: csatya11@gmail.com

(Received 25 September 2025; revised 8 November 2025; accepted 11 November 2025; published 6 April 2026)

Abstract: Halide perovskites have emerged as a class of materials with exceptional optoelectronic properties. While most research has focused on their semiconducting nature, the exploration of metallic states in these materials is a burgeoning field. This study investigates the electronic properties of the halide perovskite $CsAsBr_3$ for the first time, which is predicted to exhibit a metallic character. Using first-principles calculations based on Density Functional Theory (DFT), we analyze the stability of this metallic state under the application of uniaxial external strain along [100] crystallographic directions. Our results demonstrate that the metallic nature of $CsAsBr_3$ is remarkably robust, persisting under both compressive and tensile strains of up to 10%. The band structure and density of states (DOS) show that the states crossing the Fermi level, primarily composed of As 4p and Br 4p orbitals, are not significantly perturbed by the applied strain. This intrinsic stability suggests that $CsAsBr_3$ is a promising candidate for flexible and strain-tolerant electronic applications where a stable metallic conductivity is required.

Keywords: Halide-Perovskites; Strain-engineering; Electronic properties
PACS: 71.15.Mb, 71.20.-b, 68.35.Gy

1 Introduction

Over the last two decades, halide perovskites, materials adopting the ABX_3 crystal structure, have transitioned from a niche academic curiosity to the forefront of materials science research [1, 2]. Their rise to prominence was ignited by the pioneering work of Kojima et al. in 2009, which demonstrated their potential in photovoltaics [3], leading to a rapid surge in power conversion efficiencies that now exceed 25% for single-junction solar cells [4]. This remarkable performance stems from a unique combination of exceptional optoelectronic properties, including strong panchromatic light absorption, long charge-carrier diffusion lengths, and high defect tolerance [5, 6]. These attributes have also made them leading candidates for a wide range of other applications, such as light-emitting diodes (LEDs), photodetectors, and thermoelectric devices [7, 8].

The archetypal halide perovskite, methylammonium lead iodide ($CH_3NH_3PbI_3$), and its inorganic counterpart, $CsPbI_3$, have been the most extensively studied [9]. However, the presence of lead (Pb) in these high-performance materials raises significant concerns regarding environmental toxicity and long-term stability, hindering their path toward widespread commercialization [10, 11]. The inherent instability of these materials in the presence of moisture, oxygen, and heat further complicates their practical application [12]. Consequently, a major thrust of current research is the exploration of lead-free halide perovskites. Several strategies have been proposed, including the use of aliovalent cation substitution to create double perovskites ($A_2B'B''X_6$) or the replacement of the divalent Pb^{2+} with other non-toxic, isoelectronic group 14 cations like Tin (Sn^{2+}) or Germanium (Ge^{2+}) [13, 14].

An alternative and compelling strategy involves replacing the divalent group 14 cation with a trivalent group 15 cation, such as Bismuth (Bi^{3+}) or Arsenic (As^{3+}) [15]. This substitution fundamentally alters the electronic configuration from a B-site ns^2 to ns^0, which can result in novel and unexpected electronic structures. While many of these trivalent cation-based systems are predicted to be semiconductors, this theoretical study have intriguingly suggested that $CsAsBr_3$ possess a metallic ground state. The emergence of metallicity in a halide perovskite is

a significant departure from their conventional semiconducting character and opens a new design paradigm for this class of materials. A stable, solution-processable, and transparent metallic perovskite could find applications as a transparent conductor, potentially replacing indium tin oxide (ITO), or as a novel catalyst or thermoelectric material.

For any material to be considered for practical implementation, particularly in modern technologies like flexible or wearable electronics, its functional properties must be stable against mechanical stress and strain [16]. Strain engineering has become a powerful tool to tune the electronic properties of materials, often used to modify band gaps or induce phase transitions. However, in the context of a metallic material, it is crucial that the metallic state persists under operational strain. An unintended strain-induced metal-insulator transition would be detrimental to device performance and reliability. Therefore, understanding the response of the electronic structure of metallic $CsAsBr_3$ to mechanical deformation is of both fundamental and technological importance.

This paper presents a comprehensive theoretical investigation into the stability of the metallic state in $CsAsBr_3$. Using first-principles calculations, we systematically analyze the evolution of its electronic band structure and density of states under the application of uniaxial external strain. We demonstrate that the metallic nature is exceptionally robust, withstanding significant compressive and tensile strains. This finding underscores the potential of As-based perovskites as a new family of resilient metallic materials suitable for demanding electronic applications.

2 Computational Method

All first-principles calculations were performed using Density Functional Theory (DFT) [17], a powerful quantum mechanical modeling method for investigating the electronic structure of materials. We employed the Quantum ESPRESSO (version 6.8) software suite for all simulations [18, 19]. The interactions between the core and valence electrons were modeled using projector augmented-wave (PAW) pseudopotentials, which provide a balance between computational efficiency and accuracy [20]. The specific valence electron configurations considered in the pseudopotentials were Cs ($5s^2$, $5p^6$, $6s^1$), As ($4s^2$, $4p^3$), and Br ($4s^2$, $4p^5$). The exchange-correlation effects were described using the Perdew-Burke-Ernzerhof (PBE) functional, which is based on the generalized gradient approximation (GGA) [21]. This functional was chosen as it has been shown to provide reliable predictions for the structural and electronic properties of a wide range of halide perovskite systems. A kinetic energy cutoff of 50 Ry (approximately 680 eV) was applied for the plane-wave basis set to ensure convergence of the total energy. The Brillouin zone was sampled using a Monkhorst-Pack scheme with a dense $8 \times 8 \times 8$ k-point grid for structural relaxations and self-consistent calculations [22]. To handle the occupation of electronic states near the Fermi level in this metallic system, a Gaussian smearing of 0.02 Ry was applied.

The initial crystal structure of $CsAsBr_3$ was assumed to be the ideal cubic perovskite phase (space group Pm-3m, No. 221). A full geometry optimization was first performed on this unit cell, where both the lattice constant and the internal atomic positions were allowed to relax until the forces on each atom were less than 0.01 eV/Åand the total energy change between successive steps was below 10^{-5} eV. Uniaxial strain (ϵ) was subsequently applied along the $[100]$ crystallographic direction, a common method to simulate mechanical deformation in theoretical studies. The strain is defined as $\epsilon = (a - a_0)/a_0$, where 'a' is the strained lattice constant along the applied direction and 'a_0' is the fully relaxed equilibrium lattice constant from our initial optimization. The external uniaxial strain was applied to the x-direction of the unit cell at -10 % (compressive strain) to +10% (tensile strain). Finally, the electronic band structure and projected density of states (PDOS) were calculated for each relaxed, strained structure to systematically track the evolution of the electronic properties.

3 Results and Discussion

3.1 Electronic Properties of Unstrained $CsAsBr_3$

First, we optimized the crystal structure of $CsAsBr_3$ in its cubic perovskite phase (space group Pm-3m). The stable structure was predicted by energy minimization technique i.e. computing the lowest energy state as a function of equilibrium volume. The calculated equilibrium lattice constant was found to be 6.75 Å.

The electronic band structure and projected density of states (PDOS) for the unstrained, fully relaxed $CsAsBr_3$ are shown in Figure 1 and Figure 2. The band structure clearly shows that several bands cross the Fermi level, which is a definitive signature of metallic behavior. Unlike typical semiconducting perovskites which have a distinct band gap, $CsAsBr_3$ exhibits no gap, allowing for electronic conduction.

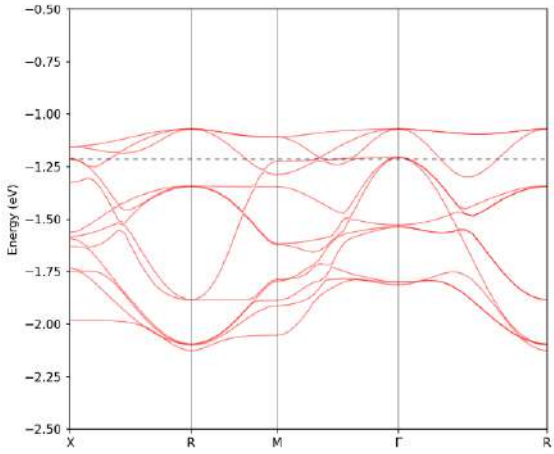

Figure 1: Bandstructure of pristine $CsAsBr_3$

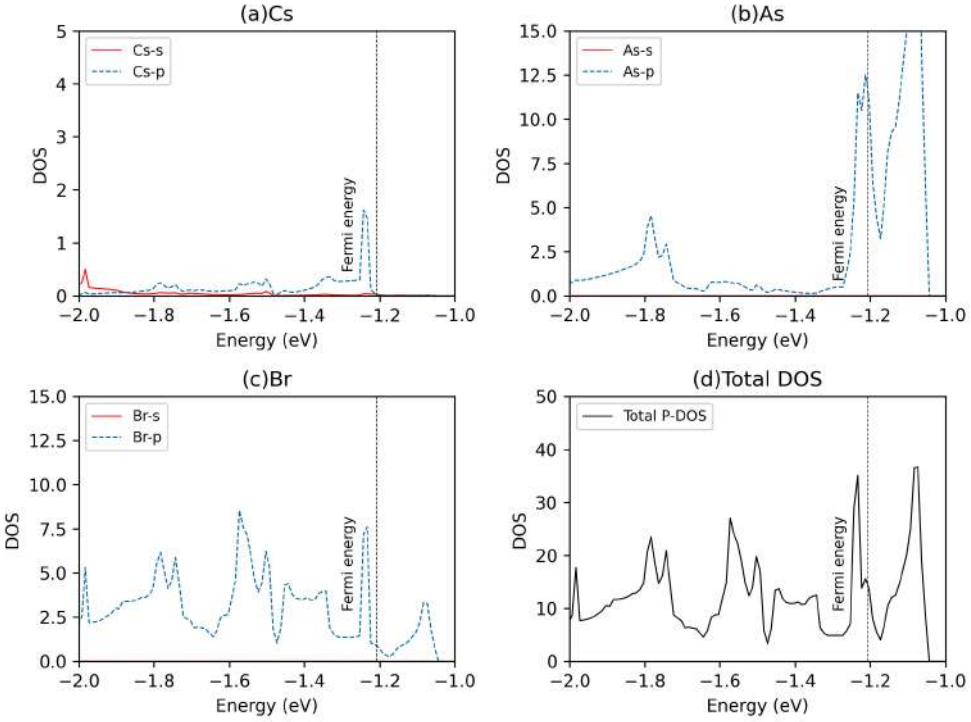

Figure 2: (a-c) PDOS and (d) DOS of pristine $CsAsBr_3$.

Analysis of the PDOS reveals the orbital contributions to the electronic states around the Fermi level. The states responsible for the metallic character arise primarily from the hybridization of As 4p and Br 4p orbitals. The conduction and valence bands are not separated, but rather overlap significantly, forming the metallic state. The Cs ions are found to have a negligible contribution to the states near the Fermi level, acting primarily as charge-donating species that stabilize the crystal structure.

3.2 Effect of Uniaxial Strain

To investigate the stability of this metallic state, we applied uniaxial strain along the [100] direction. The electronic band structures were calculated for compressive strains of -10% and tensile strains of +10%. Remarkably, the

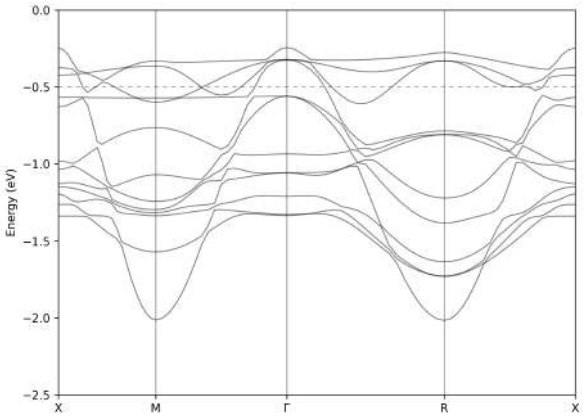

Figure 3: Bandstructure of 10% compressive strained $CsAsBr_3$

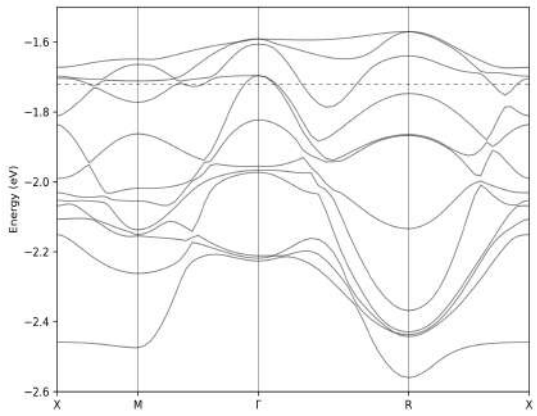

Figure 4: Bandstructure of 10% tensile strained $CsAsBr_3$

metallic character of $CsAsBr_3$ is preserved across the entire range of applied strain as shown in Figure 3 and Figure 4. In all cases, the bands continue to cross the Fermi level, indicating that a strain-induced metal-insulator transition does not occur within this range. While the applied strain does cause minor shifts in the band energies and alters their dispersion, these changes are not significant enough to open up a band gap.

Under compressive strain, the lattice constant in the applied direction is reduced, leading to increased overlap between the As 4p and Br 4p orbitals as shown in Figure 5. This slightly broadens the bands, but the fundamental metallic nature remains unchanged. Conversely, under tensile strain, the lattice is elongated, slightly reducing the orbital overlap as shown in Figure 6. This leads to a minor narrowing of the bands, but again, the overlap at the Fermi level is maintained.

The metallic conductivity arises from the strong overlap and mixing (hybridization) of the As 4p orbitals and the Br 4p orbitals.These hybridized p-orbitals form a continuous, three-dimensional (3D) framework throughout the crystal lattice. This 3D connectivity allows electrons to move freely in all directions, creating the material's metallic band structure (specifically, the Fermi level is crossed by these bands, indicating no band gap).

The robustness of the metallic state can be attributed to the intrinsic electronic structure of $CsAsBr_3$. The states at the Fermi level are derived from strong covalent interactions within the $[AsBr_3]^-$ framework. The three-dimensional nature of the perovskite structure and the p-orbital character of the relevant bands provide sufficient electronic pathways for conduction. When uniaxial strain (stretching or compression) is applied, the lattice dimensions change. However, because the electron-conducting orbitals are connected in three dimensions, the deformation along [100] axis is effectively compensated or distributed throughout the entire lattice. This strong 3D connectivity prevents the moderate lattice distortion from significantly altering the orbital overlap needed for hybridization. The p-orbital energy levels and their crossing of the Fermi level remain largely intact. Our DFT calculations essentially show that even under 10% strain, the metallic bands around the Fermi level do not separate to form a band gap. This confirms that the structural integrity of the electron-conducting channels is maintained, ensuring that the material remains metallic.

A stable, transparent, and strain-tolerant metallic perovskite like $CsAsBr_3$ is uniquely positioned for applications that require high electrical conductivity combined with mechanical flexibility and environmental durability. The most direct and high-impact application will be as a transparent conductive electrode (TCE) or charge transport layer in photovoltaic devices, addressing the limitations of existing materials like Indium Tin Oxide (ITO). Traditional ITO is brittle and cracks under strain, limiting the lifetime of flexible solar cells. $CsAsBr_3$'s stable metallic nature and strain tolerance (up to 10%) ensures the TCE maintains low resistance even when bent or stretched. It's transparency allows light to reach the active layer, crucial for high-efficiency tandem cells and transparent devices. It can also serve as the transparent, conductive layer in flexible OLEDs (Organic Light-Emitting Diodes) or capacitive touchscreens.

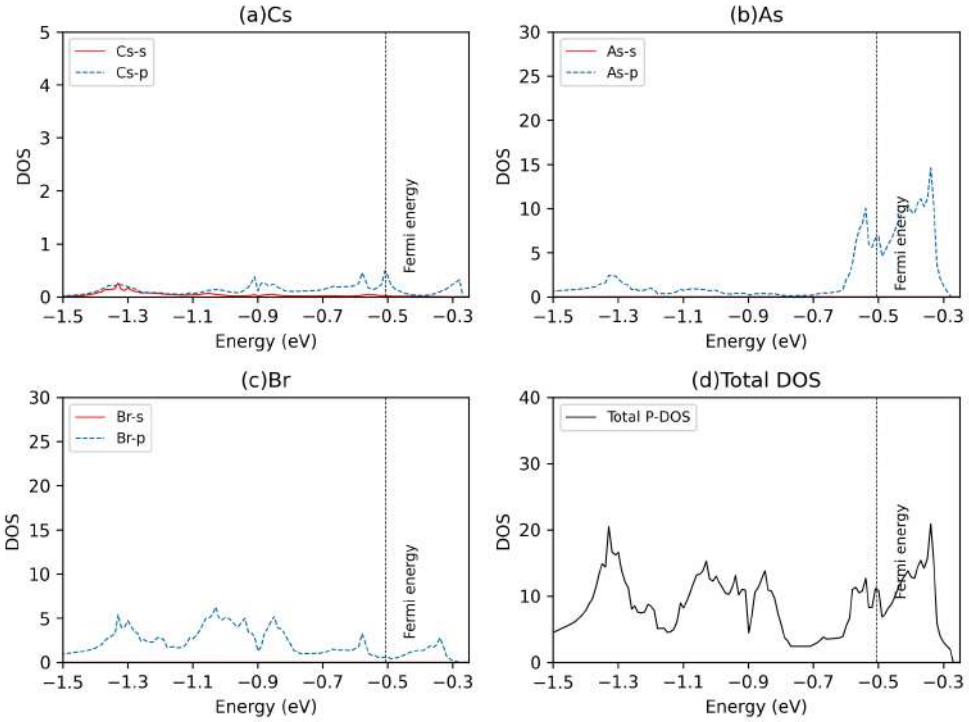

Figure 5: (a-c) pDOS and (d) DOS of 10 % compressive strained $CsAsBr_3$.

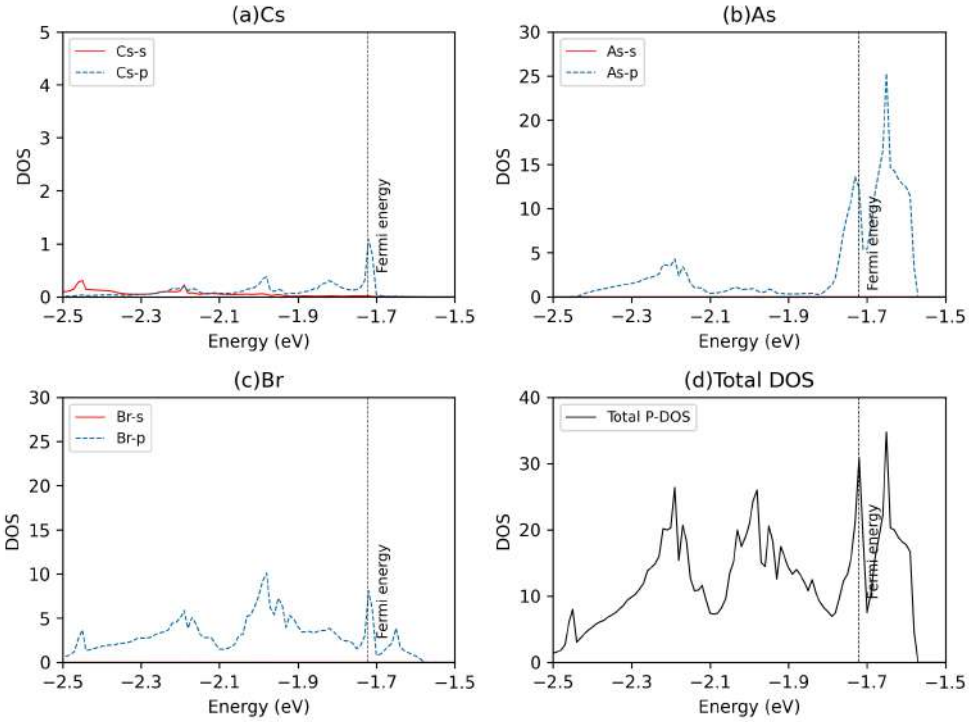

Figure 6: (a-c) pDOS and (d) DOS of 10 % tensile strained $CsAsBr_3$.

4 Conclusions

In summary, this study demonstrates through first-principles DFT calculations that the halide perovskite $CsAsBr_3$ possesses a stable metallic ground state. This metallic character, which arises from the hybridization of As 4p and Br 4p orbitals, is shown to be exceptionally robust against external uniaxial strain. The material maintains its metallic nature under both compressive and tensile strains of up to 10% applied along the [100] crystallographic direction. The resilience of the metallic state is attributed to the strong covalent framework and the three-dimensional connectivity of the electron-conducting orbitals, which are not easily disrupted by moderate lattice distortions.

The intrinsic and stable metallic nature of $CsAsBr_3$, a lead-free and relatively simple compound, makes it a highly promising material for novel electronic applications. Its robustness against mechanical strain is particularly advantageous for flexible electronics, strain sensors, and durable conductive films. This work broadens the potential functional scope of halide perovskites beyond their traditional semiconducting applications and motivates further experimental investigation into the synthesis and characterization of this intriguing class of metallic perovskites.

References

[1] M. A. Green, A. Ho-Baillie, and H. J. Snaith, Nature Photonics **8**, 506 (2014).

[2] H. J. Snaith, The Journal of Physical Chemistry Letters **4**, 3623 (2013).

[3] A. Kojima, K. Teshima, Y. Shirai, and T. Miyasaka, Journal of the American Chemical Society **131**, 6050 (2009).

[4] National Renewable Energy Laboratory (NREL), Best research-cell efficiency chart (2024).

[5] S. D. Stranks *et al.*, Science **342**, 341 (2013).

[6] R. E. Brandt, V. Stevanović, D. S. Ginley, and T. Buonassisi, MRS Communications **5**, 265 (2015).

[7] Z.-K. Tan *et al.*, Nature Nanotechnology **9**, 687 (2014).

[8] L. Dou, Y. M. Yang, J. You, and Y. Yang, Nature Communications **8**, 1470 (2017).

[9] C. C. Stoumpos, C. D. Malliakas, and M. G. Kanatzidis, Inorganic Chemistry **52**, 9019 (2013).

[10] A. Babayigit, A. Ethirajan, M. Muller, and B. Conings, Nature Materials **15**, 247 (2016).

[11] F. Giustino and H. J. Snaith, ACS Energy Letters **1**, 1233 (2016).

[12] T. Leijtens, G. E. Eperon, S. Pathak, A. Abate, M. M. Lee, and H. J. Snaith, Nature Communications **4**, 2885 (2013).

[13] Z. Xiao and Y. Yan, Advanced Energy Materials **7**, 1701136 (2017).

[14] C. C. Stoumpos *et al.*, Journal of the American Chemical Society **137**, 6804 (2015).

[15] M. R. Filip, S. Hillman, A. A. Haghighirad, H. J. Snaith, and F. Giustino, The Journal of Physical Chemistry Letters **7**, 2579 (2016).

[16] J. A. Rogers, T. Someya, and Y. Huang, Science **327**, 1603 (2010).

[17] W. Kohn and L. J. Sham, Physical Review **140**, A1133 (1965).

[18] P. Giannozzi *et al.*, Journal of Physics: Condensed Matter **21**, 395502 (2009).

[19] P. Giannozzi *et al.*, Journal of Physics: Condensed Matter **29**, 465901 (2017).

[20] P. E. Blöchl, Physical Review B **50**, 17953 (1994).

[21] J. P. Perdew, K. Burke, and M. Ernzerhof, Physical Review Letters **77**, 3865 (1996).

[22] H. J. Monkhorst and J. D. Pack, Physical Review B **13**, 5188 (1976).

SYNTHESIS AND CHARACTERIZATION OF OXIDE NANOPARTICLES FOR ITS APPLICATION IN MEMRISTIVE DEVICES

Jyoti Prasad Roy Choudhury[*a,b], Barnali Pathak[a], Nayan Mani Nath[c], and Bikash Borah[b]

[a]*Department of Physics, B.H.College, Howly, 781316, Assam, India*
[b]*Department of Physics, Assam Don Bosco University, Sonapur, 784028, Assam, India*
[c]*Department of Physics, Barnagar College, Sorbhog, 781317, Assam, India*

[*]Corresponding Author: jyotirc62@gmail.com

(Received 6 September 2025; revised 12 November 2025; accepted 17 November 2025; published 6 April 2026)

Abstract: Zinc and lead oxide (ZnO & PbO) nanoparticles synthesis was carried out using a low-cost chemical precipitation technique with polyvinylpyrrolidone (PVP) as the stabilizer. These semiconducting metal oxides were chosen because of their distinct electronic characteristics and their wide applications in upcoming generation as memory devices. Structural and morphological analyses were carried out using XRD and HRTEM study, verifying the formation of crystalline ZnO with a hexagonal wurtzite structure and PbO with an orthorhombic phase. The average crystallite sizes were calculated and found to be approximately 28.93 and 63.11 nm for ZnO and PbO respectively, indicating successful nanoscale synthesis. Electrical characterization was performed using a planar electrode configuration and a Keithley 2450 SourceMeter to evaluate the current-voltage (VI) behavior. Both samples exhibited a prominent zero-crossing pinched hysteresis loop in their VI curves which is a hallmark of a pure memristive behavior. The switching between High and Low Resistance State i.e. HRS and LRS respectively is governed by SET and RESET voltages, was stable and repeatable across multiple cycles, demonstrating strong potential for non-volatile memory applications. The results suggest that ZnO and PbO thin films can act as reliable memristive elements capable of storing and retaining binary information. Their stable resistive switching behavior makes them promising candidates for use in resistive random-access memory (RRAM) and neuromorphic computing systems. This work not only validates the memristive properties of these materials but also paves the way for their integration into low-cost, high-performance electronic devices.

Keywords: Zinc Oxide, Lead Oxide nanoparticles, opto-electronics behavior, memristivity, pinched hysteresis curve.

PACS: 81.05.Hd

1 Introduction

For the past several years, metal oxide semiconductor nanoparticles have attracted significant research interest due to their remarkable physicochemical properties. These include tunable electrical conductivity, a high surface area with respect to its volume, and pronounced quantum confinement effects, which make them highly suitable for various advanced applications in almost every field. Among several nanoparticles, zinc oxide (ZnO) and lead oxide (PbO) stand out due to their distinct electronic characteristics. ZnO possesses a wide band gap of approx 3.37 eV and also exhibits a high exciton binding energy of nearly 60 MeV, which makes it particularly advantageous for optoelectronic and photonic devices [1]. On the other hand, the band gap of PbO is comparatively narrower which is about 2.59 eV [2] at room temperature, making it suitable for different applications that require lower energy thresholds. ZnO, in particular, is extensively utilized in biomedical and environmental fields because of its non-toxic, biocompatible, and eco-friendly nature, making it a widely available and versatile material [3].

The concept of memristive behavior in semiconducting materials was first introduced by Leon Chua in 1971, who theoretically proposed the presence of a fourth essential circuit element known as memristor alongside the well-established resistor, capacitor, and inductor [4]. The memristor, short for "memory resistor," is a device with two terminals that directly relates electric charge with magnetic flux [5]. Its key feature is its ability to retain information about the amount of electrical current that has previously passed through it. This non-volatile memory behavior helps the memristor to "remember" the most recent resistance that passed through it even after the power is turned off, making it a promising candidate for future memory storage and neuromorphic computing technologies [6, 7].

A significant breakthrough in this area came in 2008 as the scientists at HP Labs perform their first experiment that validate Chua's theoretical model by demonstrating memristive behavior in a thin film of titanium dioxide (TiO_2) [6]. Since then, the field has witnessed a surge in studies exploring memristive effects in various nanomaterials and metal oxide-based systems. In particular, oxide-based nanocomposites have been the subject of extensive investigation due to their stable and reproducible electrical switching characteristics. The VI characteristic of these materials shows a zero crossing pinched hysteresis curve, which is a signature of memristive behavior [8, 9]. In our study, the fabricated samples also demonstrated such a loop, indicating the presence of memristive properties.

Numerous researchers have explored similar findings across different material systems [10]. For example, in a study conducted by Barnes $et.al$ and colleagues during 2018, a ZnO-based memristor exhibited a clear hysteresis loop within a voltage sweep range of +20V to -20V, further confirming the suitability of ZnO in memristive device applications [11]. These findings highlight the potential of metal oxide nanostructures, particularly ZnO, as promising candidates for next-generation memory and logic devices, paving the way for advancements in nanoelectronics and artificial intelligence hardware.

In recent years, extensive research has been carried out on ZnO and PbO nanoparticles across various fields. However, the available studies remain inadequate for developing memristive devices that effectively utilize their promising optoelectronic properties. To bridge this research gap, ZnO and PbO nanoparticles were prepared by a simple and inexpensive chemical bath deposition technique, employing a PVP matrix to regulate particle growth. Although numerous studies have explored oxide-based nanocomposites, reports focusing specifically on the memristive behavior and its sensitivity $i.e.$ the Roff/Ron ratio of ZnO and PbO nanoparticles are lacking.

Unlike previous works that utilized complex and expensive synthesis methods for other oxide nanomaterials, this study demonstrates that ZnO and PbO nanoparticles, prepared through a straightforward and low-cost process, exhibit notable memristive properties. The structural, electrical, and morphological characteristics of these samples are analyzed and correlated with their mem-behavior, offering valuable insights for the design and development of next-generation mem-devices.

2 Synthesis of ZnO and PbO Nanoparticles

All the chemical reagents required for our experimental procedures were procured from Merck to ensure analytical-grade purity. The primary chemicals utilized in the synthesis process included Zinc Acetate Di-hydrate having chemical formula $Zn(CH_3COO)_2 \cdot 2H_2O$, Lead Acetate $i.e.$ $Pb(CH_3COO)_2 \cdot 4H_2O$, Sodium Hydroxide $i.e.$ NaOH & Polyvinylpyrrolidone which is PVP, which was used as a stabilizing and capping agent. To prepare the necessary reaction medium, a 3% PVP liquid solution was first made by adding an appropriate amount of PVP powder mixed in distilled water under constant magnetic stirring to ensure complete homogenization.

2.1 Production of ZnO Nanoparticles

To synthesize ZnO nanoparticles, a 0.3 M solution of $Zn(CH_3COO)_2 \cdot 2H_2O$ was made by dissolving Zn-salt into 50 mL of the preprepared 3% PVP solution at room temperature. The solution was stirred continuously until the Zinc Acetate was completely dissolved and uniformly dispersed in the polymer matrix. Once a clear and homogenous solution was obtained, 1 M of NaOH (50 mL) is added in drops to the solution maintaining the reaction temperature at approximately $90°C$. This addition was performed under continuous stirring to ensure controlled formation and development of the nanoparticles. After about 45 to 50 minutes of reaction time, the solution gradually turned milky white, which is a visual indication of the successful formation of ZnO nanoparticles. The resulting colloidal solution was then subjected to filtration to separate the solid product. The collected precipitate was subsequently dried in a hot air oven to remove residual moisture and obtain the dry ZnO nanopowder.

2.2 Production of PbO Nanoparticles

PbO nanoparticles were also prepared following a similar process. A solution of 0.3 M of $\mathrm{Pb(CH_3COO)_2 \cdot 4H_2O}$ was made by mixing the appropriate amount of Pb-salt in 50 mL PVP (3%) at ambient temperature. The solution was stirred until the salt was completely dissolved and uniformly incorporated into the PVP medium. Now, 50 mL of 1 M NaOH solution is introduced slowly in the reaction medium in a dropwise manner, while maintaining the system at $90^{\circ}C$ under vigorous stirring. Over a period of approximately 60 to 70 minutes, the solution began to change color from colorless to a pale yellow hue, signifying the formation of PbO nanoparticles. Following this color change, the reaction mixture was filtered to isolate the solid PbO product. The filtered nanoparticles were then dried in a hot air oven to remove any remaining moisture, yielding the final PbO nanopowder.

This synthesis approach, utilizing PVP as a stabilizing agent, helps in controlling the particle size and preventing agglomeration during the formation process. Both ZnO and PbO nanoparticles produced through this method were later used for further characterization and device fabrication studies.

2.3 Characterization Techniques

A variety of advanced techniques for characterization were employed that analyze the properties such as: structural properties, morphological properties, and electrical properties of the synthesized semiconducting nanomaterials. These techniques play a crucial role in determining key parameters such as crystal structure, particle size, surface morphology, elemental composition, and optical and electrical behavior. Among the methods used, XRD, HRTEM, and electrical characterization done using precision electrometers were central to our study.

The investigation of the crystallographic structure and also to study the purity phase of the prepared nanoparticles, XRD analysis was done using an ULTIMA IV X-Ray diffractometer. This technique gives all the information about the crystal system, lattice parameters, and average crystallite size through analysis of diffraction patterns. The XRD peaks also confirm the crystalline nature and formation of ZnO and PbO nanoparticles by studying the sharpness and intensity of the peaks.

For further insights into the microstructure and morphology study, HRTEM was utilized. This technique enabled visualization of the shape, size distribution, and particle boundaries with high spatial resolution. HRTEM also provided detailed lattice fringe images that is use to support the crystalline structure and to measure interplanar spacing, thereby validating the results obtained from XRD analysis.

2.4 Electrical Characterization

The electrical behaviors of the synthesized samples were analyzed using a Source-Meter, which allowed precise VI measurements. A planar electrode configuration with a defined gap was utilized for I-V measurement. The prepared sample is placed between two silver electrodes (Ag paste) which is finally placed in a glass substrate. Both the electrodes are then connected to a computer interfaced Keithley-2450 electrometer source for the measurement of required electrical data. The electrical response of the samples was measured by sweeping the voltage between –10V +10V. These VI measurements were critical in evaluating the memristive behavior of the samples and in identifying non-linear and hysteretic behavior in the current-voltage relationship, which is indicative of memory-resistance character.

Thus all these techniques gives a detail comprehensive understanding of all the structural and functional properties of the prepared ZnO and PbO nanomaterials, enabling further evaluation of their potential in memristive and other electronic applications.

3 Results and Discussion

Structural analysis of the as prepared ZnO and PbO semiconductor nanoparticles were thoroughly investigated with the help of X-ray Diffraction (XRD) analysis. This technique is essential for determining the crystallographic structure, lattice parameters, and average crystallite size of nanomaterials. The famous Bragg's Law is the basic principle behind XRD analysis, that relates the angle of diffraction to the interplanar spacing in a crystalline material [12, 13]. The Bragg equation is expressed as:

$$2d \sin\theta = n\lambda \tag{1}$$

Where,

λ known is wavelength of the X-ray beam used whose value is 1.5406 Å,
θ known as angle of diffraction,
d is called interplanar spacing, and
The diffraction order is used as n (taken as 1 for simplicity).

Upon analyzing the XRD spectra of the prepared samples Fig. 1, distinctive diffraction patterns were observed, confirming the crystalline nature of both ZnO and PbO nanoparticles. According to standard reference data from the JCPDS- 00 001 1136 and JCPDS- 00 003 0599, the diffraction peaks for ZnO correspond well with a hexagonal wurtzite crystal structure, while those for PbO match an orthorhombic structure respectively.

For ZnO nanoparticles, characteristic peaks were identified at the planes (100), (002), (101), and (110), indicative of a hexagonal phase. For PbO nanoparticles, the diffraction peaks observed at (002), (201), (003), and (131) confirm the orthorhombic crystalline phase. These observations validate the successful formation of the desired crystalline structures for both materials.

Using the peak positions from the XRD patterns, the lattice constants were calculated. Lattice parameters of ZnO were found to be 3.238 & 5.200Åwhich are consistent with standard values for hexagonal ZnO structures. Whereas for PbO nanoparticles, the parameters were found to be 5.49, 4.73 & 5.86Åconfirming orthorhombic phase of PbO. To estimate the crystallite dimension, Debye–Scherrer formula was applied:

$$D = \frac{K\lambda}{\beta \cos\theta} \tag{2}$$

Where,
D known as crystallite dimension,
K is known as the shape factor whose value is 0.9,
λ known as X-ray wavelength (1.5406 Å),
β known as FWHM of diffraction peak (in radians), &
θ is known as the Bragg angle.

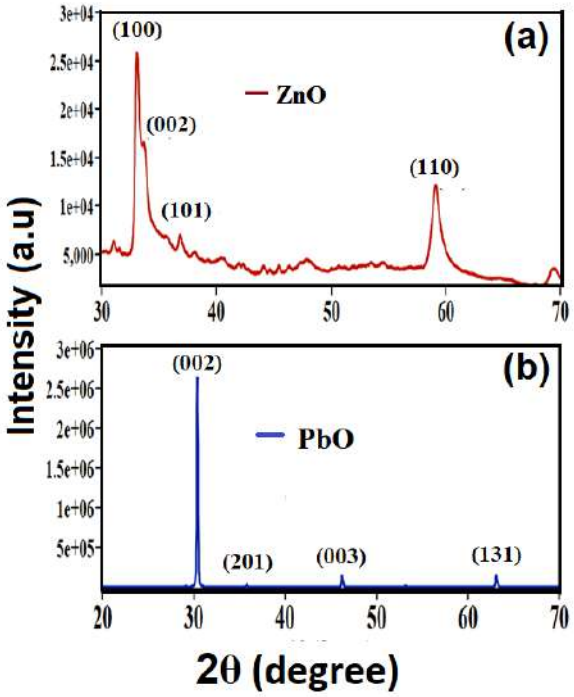

Figure 1: XRD pattern observed for prepared ZnO and PbO

Using this equation, the crystallite sizes of the synthesized nanoparticles were calculated. The crystallite dimension (size) was found to be approximately 28.93 and 63.11 nm for ZnO and PbO respectively, suggesting that the ZnO nanoparticles are finer and more narrowly distributed compared to PbO. These structural findings derived from XRD analysis established the successful formation of the crystalline ZnO and PbO nanomaterials

with their respective lattice structures and nanoscale dimensions. Detailed XRD data, including diffraction angles, FWHM, and size, are summarized in the table below.

Sample	2θ (degree)	FWHM	Size (nm)	Average size (nm)
ZnO	33	0.307	26.38243	28.934
	35.79	0.358	22.79518	
	38.1	0.409	20.08757	
	56.705	0.170	46.4701	
PbO	30.69	0.1535	52.00127	63.110
	36.343	0.1023	76.57744	
	46.535	0.1279	61.45046	
	63.204	0.1223	62.41900	

Table 1: Data obtained from XRD study

The structural and surface morphological features of the synthesized ZnO and PbO nanoparticle samples were thoroughly investigated using HRTEM. The micrographs, are shown in Fig. 2, clearly reveal that the ZnO nanoparticles exhibit a well-defined structure. This is evident from the uniform and periodic lattice fringes observed in the images. On the other hand, the PbO particles demonstrate a distinct morphology. These morphological features are consistent with the structural patterns observed in the XRD analysis, confirming the phase purity and crystallinity of the synthesized materials.

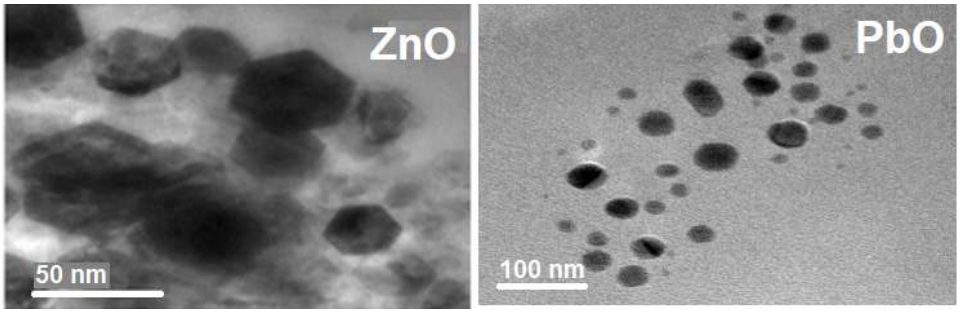

Figure 2: HRTEM images for ZnO and for PbO nanomaterials of different magnifications

A planar electrode configuration with a defined gap was utilized to investigate the VI graph of the thin film. This geometry allows for precise measurement of electrical behavior across the sample. The VI measurements are done by using a Keithley 2450 Source-Meter electrometer, which is well-suited for sourcing voltage and measuring the resulting current with high accuracy and sensitivity. This instrument enabled detailed analysis of the electrical response of the material under study. To aid in understanding the experimental setup, a simplified schematic diagram illustrating the measurement arrangement with the Keithley 2450 electrometer is presented below in Fig. 3. This setup ensures a good and reproducible technique for characterizing the electrical properties of thin films using the gap-type planar electrode structure.

The VI characteristic graph for both nanoparticles were plotted over a voltage range from -10V – +10V as shown in Fig. 4(a&b). These curves provide insight into the electrical behavior and conduction mechanisms of the materials under the applied voltage. The resulting plots, shows zero crossing hysteresis graph which is the prime characteristic of a memristor. This confirms that our prepare device can acts as a memristor.

4 Memristive Behavior of prepared nanoparticles

The VI characteristics obtained from the prepared samples demonstrate a distinct zero-crossing pinched hysteresis loop, a well-known and defining feature of memristive systems [14]. This pinched hysteresis behavior, where the I-V curve intersects the origin: is considered a key indicator of memristive functionality. In the context of our study, the loops observed clearly confirm the memristive nature of the devices, with the point of intersection (pinching) occurring precisely at the origin of the current-voltage plane.

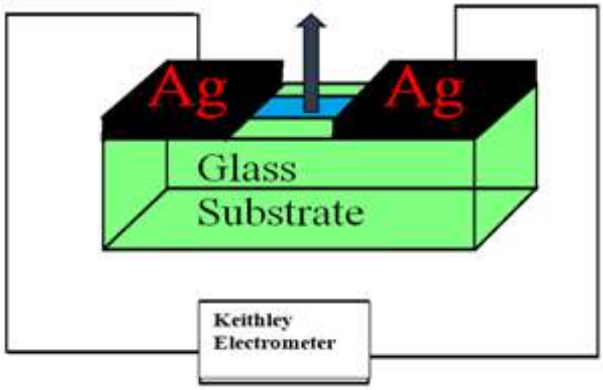

Figure 3: Electrical measurement done using source meter

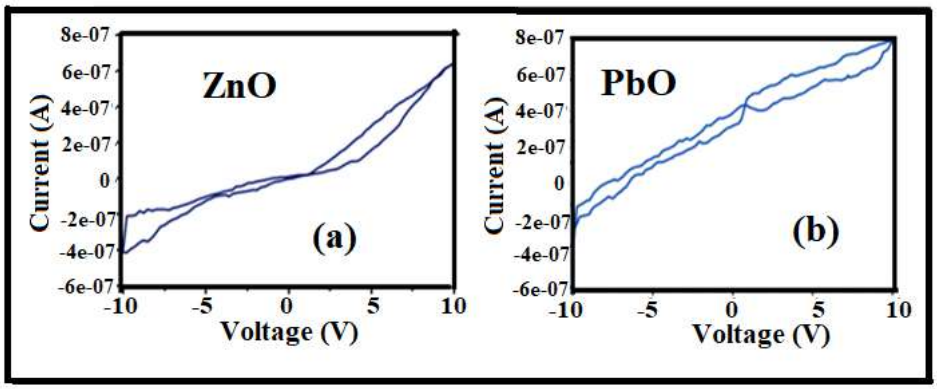

Figure 4: (a) VI graph of ZnO & (b) PbO

As shown in Fig. 5, the measurement sequence was carefully designed to observe this behavior. The voltage was swept in four stages: from 0 V t→ +10 V → 0 V → -10 V → 0 V. During the initial increase from 0 V → +10 V, the current in the device gradually increased, indicating that the device initially to be at in a High Resistance State (HRS). As the voltage reached around +10 V, a transition occurred that shift the device into the Low Resistance State (LRS), also referred to as the ON state. This voltage threshold at which the device goes from HRS to LRS is known as the SET voltage [15].

Once in the LRS, the device maintained this state as the voltage was swept toward the negative range. Upon reaching approximately -10 V, another transition was observed—this time from LRS back to HRS—marking the device's return to the OFF state. The voltage at which this transition occurs is termed the RESET voltage [16].

To give a clear picture of this resistive switching behavior, a representative I-V plot is included in Fig. 5, illustrating the change between HRS and LRS states. Multiple measurements were conducted to ensure the reliability of the obtained results. Across several cycles, the same pinched hysteresis pattern was consistently observed in both ZnO and PbO thin film-based memristive devices. This repeatability strongly suggests stable switching characteristics and reliable memristive behavior in the fabricated devices.

The zero-crossing pinched hysteresis loop typically consists of two distinct states: the LRS and the HRS. This state gives the fundamental switching behavior of memristive devices. The transition from HRS to LRS and from LRS back to HRS is crucial for memory-related applications, as it enables the storage and retrieval of binary information. This switching capability forms the basis for employing memristors in non-volatile memory technologies, where the two resistance states correspond to logical "0" and "1", thereby highlighting their potential in next-generation memory and neuromorphic computing systems.

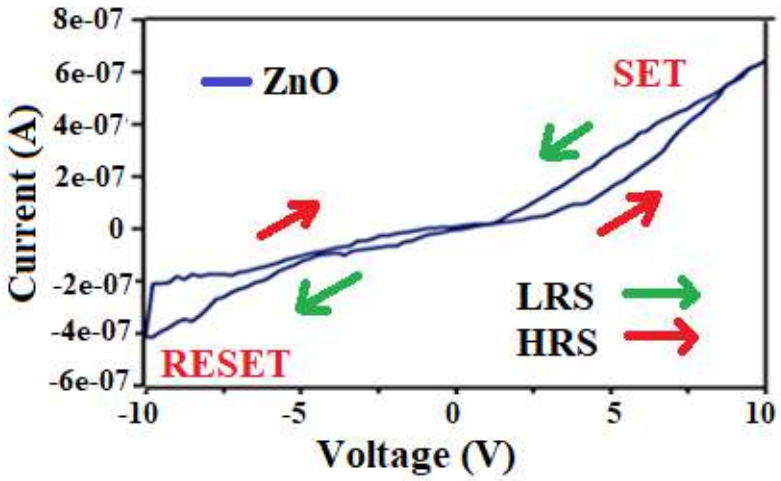

Figure 5: Zero crossing behavior of memristor with arrow indicating the direction of current.

5 Conclusion

Thus this study explains the preparation, characterization, and electrical behavior of ZnO and PbO nanoparticles, with a particular focus on their memristive properties. Using a straightforward chemical precipitation method aided by polyvinylpyrrolidone (PVP) as a stabilizing agent, both ZnO and PbO nanoparticles were synthesized under controlled conditions. The synthesis route proved effective in producing nanomaterials with desired phase purity, morphology, and crystallinity. Structural and morphological analysis confirmed the successful formation of the respective crystal structures—hexagonal wurtzite for ZnO and orthorhombic for PbO—as evidenced XRD and HRTEM. The crystallite dimension, calculated using the D-S equation, was found to be in the nanoscale range, approximately 28.93 and 63.11 nm for ZnO and PbO respectively. These findings affirm that the synthesis method employed was suitable for producing well-defined, nanosized semiconducting metal oxide particles. Electrical characterization was conducted using a gap-type planar electrode configuration in combination with a Keithley 2450 Source-Meter, allowing accurate VI measurements. Both ZnO and PbO thin films exhibited a clear zero-crossing pinched hysteresis loop in their I-V curves, which is a hallmark of memristive behavior. These loops indicate a reversible transition between a HRS and LRS, governed by SET and RESET voltages. The observed resistive switching behavior confirms the potential of these materials for application in non-volatile memory devices. Furthermore, the memristive characteristics showed good repeatability over multiple voltage cycles, demonstrating the devices' stability and consistency. This repeatable hysteresis loop implies that both ZnO and PbO thin films possess the essential features required for use in resistive random-access memory (RRAM) and neuromorphic systems, where the ability to switch and retain resistance states is critical. In summary, this work highlights the feasibility of using chemically synthesized ZnO and PbO nanoparticles in memristive device applications. Their favorable electrical behavior, combined with structural and morphological integrity, opens up promising avenues for their integration into future memory storage technologies and next-generation intelligent computing architectures.

Acknowledgement

We would like to thank SAIF Gauhati University for providing XRD facility, Department of Physics, Gauhati University and CIF IIT Guwahati for HRTEM facility.

References

[1] S. S. Kumar, P. Venkateswarlu, V. R. Rao, and G. N. Rao, International Nano Letters **3**, 30 (2013).

[2] D. H. Besisa, E. M. Ewais, and Y. M. Ahmed, Journal of Environmental Management **285**, 112094 (2021).

[3] H. Mirzaei and M. Darroudi, Ceramics International **43**, 907 (2017).

[4] T. Dao Thanh, V.-T. Pham, and C. Volos, in *Mem-elements for Neuromorphic Circuits with Artificial Intelligence Applications*, Advances in Nonlinear Dynamics and Chaos (ANDC), edited by C. Volos and V.-T. Pham (Academic Press, 2021) pp. 347–360.

[5] L. Chua, IEEE Transactions on Circuit Theory **18**, 507 (1971).

[6] D. B. Strukov, G. S. Snider, D. R. Stewart, and R. S. Williams, Nature **453**, 80 (2008).

[7] L. Wang, C. Yang, J. Wen, S. Gai, and Y. Peng, Journal of Materials Science: Materials in Electronics **26**, 4618 (2015).

[8] B. Pathak, P. Kalita, N. M. Nath, N. Aomoa, and J. Choudhury, Materials Science in Semiconductor Processing **149**, 106892 (2022).

[9] D. Yu, Y. Liang, H. H. C. Iu, and L. O. Chua, IEEE Transactions on Circuits and Systems II: Express Briefs **61**, 758 (2014).

[10] F. Gul and H. Efeoglu, Ceramics International **43**, 10770 (2017).

[11] B. K. Barnes and K. S. Das, Scientific Reports **8**, 2184 (2018).

[12] P. A. Rundquist, P. Photinos, S. Jagannathan, and S. A. Asher, The Journal of Chemical Physics **91**, 4932 (1989).

[13] V. D. Mote, Y. Purushotham, and B. N. Dole, Journal of Theoretical and Applied Physics **6**, 6 (2012).

[14] Y. V. Pershin and M. Di Ventra, Journal of Physics D: Applied Physics **52**, 01LT01 (2018).

[15] Y. Yu, C. Wang, C. Jiang, I. Abrahams, Z. Du, Q. Zhang, J. Sun, and X. Huang, Applied Surface Science **485**, 222 (2019).

[16] T. D. Dongale, P. J. Patil, N. K. Desai, P. P. Chougule, S. M. Kumbhar, P. P. Waifalkar, P. B. Patil, R. S. Vhatkar, M. V. Takale, P. K. Gaikwad, and R. K. Kamat, Nano Convergence **3**, 16 (2016).

LIGHT SCATTERING INVESTIGATION OF BLACK TURMERIC (CURCUMA CAESIA): A COMPARATIVE STUDY WITH ESTABLISHED MIE THEORY

Farhana Hussain[1] and Sanchita Roy[1*]

[1]*Department of Physics, School of Applied Sciences, University of Science and Technology, Meghalaya, District- Ri Bhoi, 793101, Meghalaya, India.*

[*]Corresponding Author: rsanchita1@gmail.com

(Received 25 September 2025; revised 22 November 2025; accepted 22 November 2025; published 6 April 2026)

Abstract: This study reports measurements of the angular distribution of the scattering matrix elements d_{11} and d_{12} for randomly oriented sub-micron Black turmeric (Curcuma caesia) particles using a light scattering technique with a He–Ne laser at 632.8 nm. The volume scattering function and depolarization effects were experimentally investigated at room temperature (25°C). Theoretical predictions of d_{11} and d_{12} were obtained using Philip Laven's software, based on Mie theory, which describes light scattering by spherical or randomly oriented non-spherical particles. A significant deviation was observed between experimental results and theoretical profiles, indicating the strong influence of particle size, shape, and their distributions on scattering behavior. Given the organic nature of Black Turmeric, external factors such as temperature, humidity, and moisture can further alter scattering characteristics. While experiments can be extended to different temperatures, theoretical modeling remains restricted, as widely used light scattering codes do not account for temperature effects or distributions in size and shape. These findings highlight both the practical importance of experimental investigation for organic samples and the limitations of Mie theory in fully capturing the scattering behavior of Black Turmeric particles under varying conditions.

Keywords: Light scattering; Mie theory; Volume scattering function; Depolarization; Black Turmeric

PACS: 07.05.-t; 85.60.-q

1 Introduction

Among the many ways light interacts with matter, scattering stands out as a phenomenon that shapes both the subtle hues of the natural world and the intricate visual signatures of living systems. Emerging wherever electromagnetic waves encounter structural irregularities, it serves as a window into the morphology and optical nature of particles [1–3]. The interaction of light with matter not only enriches our understanding of fundamental physics but also drives innovation across diverse domains such as Biomedical Imaging, Material Characterization, Atmospheric Science, Optical Biosensing and Point-of-Care Diagnostics, Drug Delivery and Nanomedicine, Food and Agricultural Sciences, Environmental Monitoring and Remote Sensing, Nanotechnology etc. Light scattering, although conceptually simple, is governed by complex parameters including particle size, morphology, chemical composition, and refractive index [3, 4]. Upon striking a particle, photons may undergo absorption, refraction, or directional redistribution, generating scattering profiles that carry distinct imprints of the material's structural properties [5–8].

Among various theoretical approaches, Mie theory provides a rigorous solution for the scattering of electromagnetic waves by homogeneous, isotropic spherical particles and randomly oriented non-spherical particles [9, 10]. While widely used due to its analytical nature and broad applicability, Mie theory assumes idealized conditions that may not accurately represent the complexities of real-world samples, especially those with irregular

geometries or heterogeneous compositions [9–11]. Mie theory offers an accessible way to explore theoretical scattering behavior under controlled parameters, making it valuable for comparison with experimental results. It enables users to calculate and visualize various scattering parameters, including intensity patterns, polarization effects, and angular distributions etc [12, 13]. Mie Plot supports a wide range of input parameters such as particle size, refractive index, angular resolution, and wavelength, allowing for detailed and customizable simulations [11–13]. However, most widely used light scattering software lacks the capability to incorporate parameters such as size distribution, shape distribution, temperature, and other environmental factors [14, 15]. Its intuitive interface and flexible simulation options make it particularly useful for modeling how light interacts with spherical particles [16, 17].

In recent years, bio-organic materials have attracted growing interest due to their distinctive structural and optical properties. One such material, Black Turmeric (BT), contained sub-micron-sized particles and showed promising potential in fields such as medicine, cosmetics, and material science [18–20]. However, despite its relevance, minimal research was carried out to understand how this material scatters light, especially under well-controlled experimental conditions.

In this study, we examined the angular distribution of the scattering matrix elements d_{11} and d_{12} for randomly oriented sub-micron BT particles. We used a He-Ne laser with a wavelength of 632.8 nm to measure the volume scattering function, $\beta(\theta)$, and analyzed depolarization effects through the degree of linear polarization, $P(\theta)$, at room temperature [20–22]. In light scattering, $\beta(\theta)$ represents the volume scattering function, quantifying the scattered light intensity at angle θ, while $P(\theta)$ accounts for the degree of polarization change as light is scattered at angle θ.

`MiePlot` simulations provided valuable insights and served as baseline predictions, notable deviations emerged when compared to the measured scattering behavior of sub-micron BT particles. These differences underscore the limitations of Mie theory, especially when applied to complex biological samples with irregular shapes, internal inhomogeneities, and a range of particle sizes, conditions that deviate from the ideal assumptions of the model.

In this study, we investigated the angular distribution of scattering matrix elements d_{11} and d_{12} for sub-micron BT particles using a He-Ne laser at 632.8 nm. Experimental measurements of the $\beta(\theta)$ and $P(\theta)$ at room temperature were compared with theoretical predictions generated using Philip Laven's Mie Plot software. While Mie theory provided useful insights, significant discrepancies highlighted its limitations in modeling complex, irregular biological particles.

2 Methodological details

2.1 Scanning Electron Microscopy (SEM) of BT

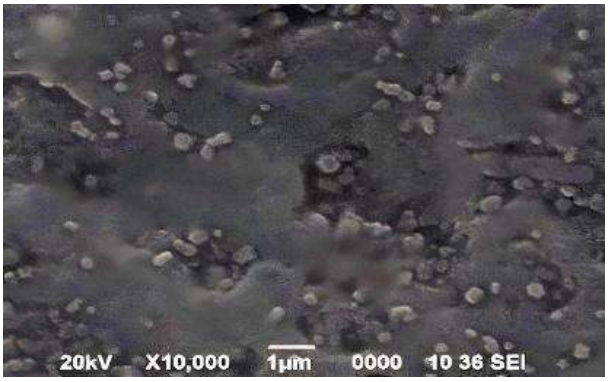

Figure 1: SEM image of BT

SEM images provided high-resolution insights into the morphology of the BT sample. The BT particles were observed to be nearly spherical, with a modal radius of approximately $0.25\mu m$ [14, 20]. The SEM image enabled us to find the parameters required to generate the theoretical scattering profile Mieplot. Accurate knowledge of particle size and shape is crucial for light scattering studies, as these parameters directly influence the scattering behavior. It is supported by Laven's software, though with limitations in parameters such as temperature, size distributions, and shape distributions, and the imaginary component of the refractive index.

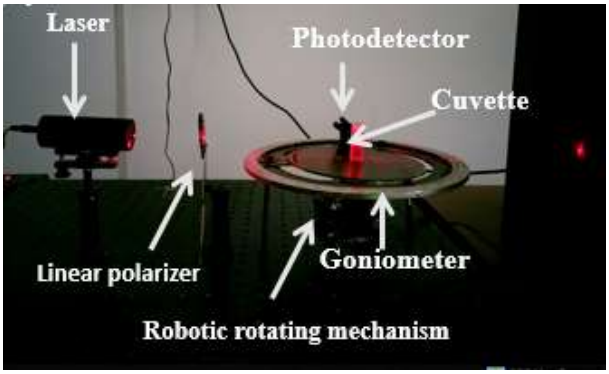

Figure 2: Laboratory-based static light scattering setup

2.2 Experimental Light Scattering Analysis

During the light scattering experiments, the detector was first placed at 0° and then rotated in 1° increments from 10° to 170° to measure the angular distribution of the scattered light. Fig. 2 shows the laboratory-based light scattering setup used for the experimentation and analysis. The intensity of the scattered light, corresponding to the d_{11} and d_{12} elements of the Mueller matrix, was recorded using the light scattering setup. These measurements were then used to calculate the $\beta(\theta)$ and $P(\theta)$. For ease of comparison, the resulting $\beta(\theta)$ and $P(\theta)$ curves were normalized to a value of 1 at 10°. All measurements were conducted at room temperature [14, 15, 20–22].

2.3 Theoretical light scattering analysis

Philip Laven's software based on scattering (`MiePlot v4621`) was used to generate theoretical Volume scattering function and Degree of linear polarization plots for BT. Key input parameters included the refractive indices of the particles and the surrounding medium, the modal particle radius, the angular resolution, and the incident wavelength. These values were manually input into the software, which calculates the angular scattering behavior based on Mie theory [12, 17]. While effective for idealized spherical particles, the software does not account for temperature effects or irregular particle shapes, limiting its ability to fully replicate the complexities observed in experimental BT data. Table 1 outlines the vital inputs of BT employed in the theoretical calculations for data analysis. Fig. 2 and Fig. 3 present a comparison between the Mie plot and the experimental results for BT, highlighting differences in the angular distribution of $\beta(\theta)$ and $P(\theta)$.

Table 1: Parameters used in the theoretical analysis of BT particles.

Parameter	Value
Modal radius	0.250 μm
Refractive index	1.42
Wavelength	632.8 nm
Angular resolution	1°

3 Results and Discussion

3.1 Observed $\beta(\theta)$ for Black Turmeric

The graph compares $\beta(\theta)$ corresponds to BT using experimental data (blue line) with a theoretical Mie scattering model (red line) at a wavelength of 632.8 nm at room temperature. Table 2 below compares the experimental volume scattering function of BT and the theoretical predictions based on Mie scattering. Key characteristics such as peak location, sharpness, tail behavior, and symmetry are evaluated to highlight the differences between practical observations and idealized modeling. The graph in Fig. 3 illustrates how the scattering behavior of BT particles diverges from theoretical expectations derived from Mie theory. Although both the experimental and Mie curves peak near 90°, the BT data reveals more abrupt and uneven variations around this angle. Mie theory, which

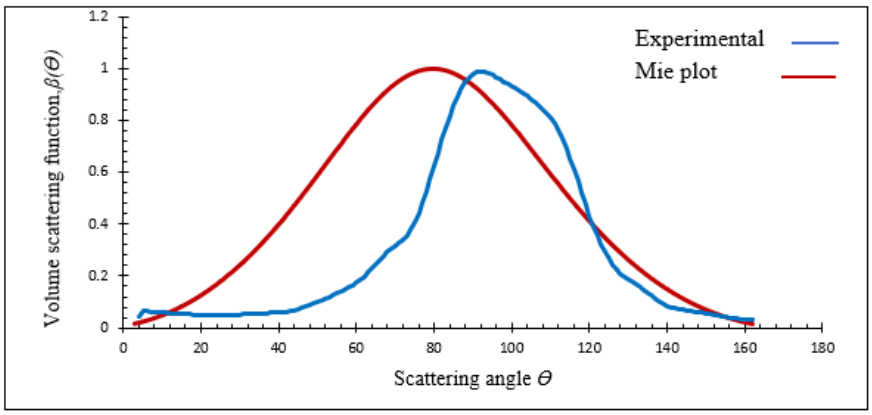

Figure 3: Comparison of measured $\beta(\theta)$ for BT: Experimental vs. Mie plot

assumes uniform, spherical particles, predicts a smooth and gradual scattering profile, but the BT plot exhibits a sharper maximum and steeper intensity drop-off on either side. These sharper features in the BT profile point to more complex interactions, likely caused by the irregular morphology of BT. Notably, the rapid decrease in scattering intensity beyond 90° in the BT curve contrasts with the gentler decline suggested by the Mie model. This discrepancy can be attributed to factors such as surface morphology, size distribution in the sample, and the porous or ”fluffy” texture of the BT sample, all of which influence light scattering in ways that simplified models cannot replicate. Furthermore, Mie theory computations typically involve a single particle radius that is modal radius, whereas real-world experiments involve a diverse mix of particle sizes and shapes. This difference contributes to the observed mismatch between theory and experiment. Consequently, the BT curve underscores the inherent limitations of applying Mie theory to organic systems, which often defy the assumptions of homogeneity and uniformity.

3.2 Observed $P(\theta)$ for Black Turmeric

The graph illustrates a comparison between the experimentally measured $P(\theta)$ of BT (blue line) and the corresponding theoretical prediction derived from Mie scattering theory (red line). Both datasets correspond to a wavelength of 632.8 nm under room temperature conditions. Complementing the visual comparison, Table 2 presents a side-by-side evaluation of key features of the experimental and theoretical $P(\theta)$, including peak position, sharpness, symmetry, and tail characteristics. This comparison sheds light on the discrepancies between real-world behavior and the idealized Mie model.

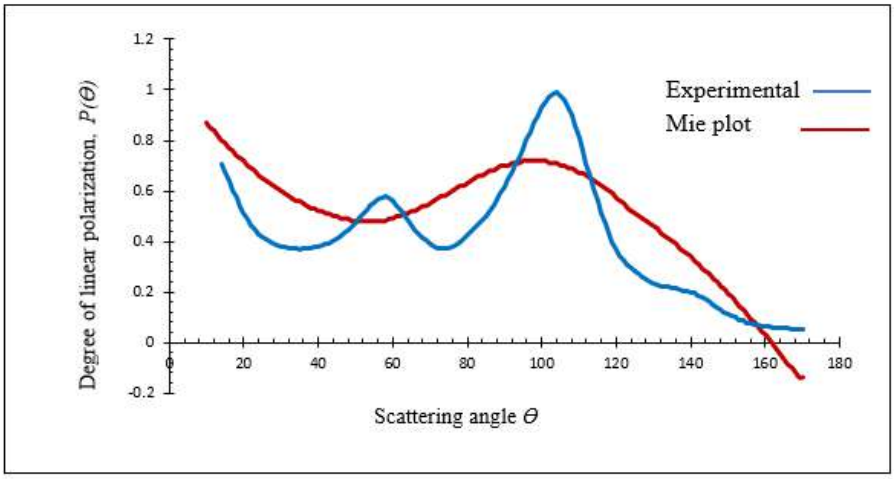

Figure 4: Comparison of Measured $P(\theta)$ for BT: Experimental vs. Mie plot

Feature	Experimental	Theoretical (Mie Plot)
Peak Location	Prominent peak around 60°	Peak occurs gradually near 90°
Sharpness	Sharp and well-defined peaks with local fluctuations	Smooth and broad peak with gradual transitions
Tail Behavior	Steep decline beyond 120°, even turning negative (polarization reversal)	Gradual descent with values staying positive throughout
Profile distribution	Asymmetric with multiple irregular features	Fairly symmetric around the peak, typical of ideal spherical scattering

Table 2: Comparison of $P(\theta)$ Characteristics: Experimental vs. Theoretical

The graph in Fig. 4 compares the $P(\theta)$ of BT using experimental data and theoretical predictions based on Mie scattering. The experimental curve (blue line) shows a non-linear variation of $P(\theta)$ with a scattering angle, characterized by multiple peaks. A prominent peak appears around 60°–70°, followed by a dip and a smaller peak near 110°, after which the $P(\theta)$ gradually decreases and exhibits slight fluctuations beyond 120°. This curve is asymmetric and irregular, reflecting the complexities that might have arisen due to temperature, size distribution, shape distribution, etc. [14, 15]. In contrast, the theoretical Mie plot (red line) exhibits a smooth and symmetrical profile, peaking broadly near 90° and gradually decreasing on either side of the angle range. Unlike the experimental data, it lacks sharp features or oscillations. These deviations arise because:

1. Inclusion of a single size parameter that is modal radius in the `MiePlot` software.
2. Size dependence of polarization and depolarization effects.
3. Possible alignment or organic particles due to gravity settling.

The $\beta(\theta)$ and $P(\theta)$ results emphasize the limitations of applying classical scattering models like Mie theory to biologically derived or structurally complex materials. These findings highlight the necessity for more advanced and flexible modeling tools that can account for real-world factors such as particle size and shape distributions. Notably, all experiments were performed at room temperature; however, the Mie plotting software used for theoretical predictions lacks the ability to incorporate temperature as a variable. Since temperature can influence the morphological characteristics of the particles in a medium, its exclusion may contribute to discrepancies between theoretical and experimental results. Therefore, integrating size and size distribution, shape and shape distribution, temperature control, or adjustment features into Mie modeling software would enhance its accuracy and relevance for experimental comparisons. Furthermore, environmental influences and measurement uncertainties, such as detector sensitivity, alignment errors, and ambient light, can also play a role in the observed deviations. This enables a relative assessment of the reported scattering matrix elements of BT from experimental measurements and theoretical predictions.

4 Conclusion

This study demonstrates the limitations of classical Mie theory in accurately modeling the light scattering behavior of randomly oriented sub-micron BT particles. Experimental measurements of the scattering matrix elements d_{11} and d_{12}, obtained using a He-Ne laser at 632.8 nm, revealed notable deviations from theoretical predictions. These discrepancies are primarily attributed to the complex particle size, shape, and distribution inherent in the BT samples, factors not accounted for in the idealized assumptions of Mie theory. While experimental investigations can be extended to varying temperature conditions, current theoretical models lack the flexibility to incorporate such variations. Overall, the comparative analysis offers valuable insights into the optical properties of BT and underscores the need for more advanced scattering models to better represent biologically complex materials. The experimental database can be created for different sizes, size distributions, temperatures, etc which will serve as a tool for better classification.

Acknowledgement

The authors wish to thank Dr. Ratan Boruah, Sophisticated Analytical Instrumentation Centre (SAIC), Tezpur University, Assam, India for his help in characterizing the Black turmeric, by SEM analysis technique.

Author contributions

SR conceived the study, FH and SR performed research, generated the scattering profiles, and analyzed figures and data. FH wrote the main manuscript, and SR and FH reviewed the results and the main manuscript.

Data Availability Statement

All data generated or analyzed during this study are included in this article.

Declarations

Conflict of interest: The authors declare no competing interests.

References

[1] A. R. Jones, Progress in Energy and Combustion Science **25**, 1 (1999).

[2] H. Zhao, X. Wang, R. Wang, D. Hua, K. Li, and F. Ji, Measurement Science and Technology **34**, 125802 (2023).

[3] E. Huber and M. Frost, Journal of Water Supply: Research and Technology–Aqua **47**, 87 (1998).

[4] L. A. Clementi, J. R. Vega, L. M. Gugliotta, and A. Quirantes, Journal of Quantitative Spectroscopy and Radiative Transfer **113**, 2255 (2012).

[5] H. E. Redmond, K. D. Dial, and J. E. Thompson, Aeolian Research **2**, 5 (2010).

[6] J. Flammer, M. Mozaffarieh, and H. Bebie, *Basic sciences in Ophthalmology: Physics and Chemistry* (Springer, 2013).

[7] M. I. Mishchenko, J. W. Hovenier, and L. D. Travis, eds., *Light Scattering by Nonspherical Particles: Theory, Measurements, and Applications* (Academic Press, San Diego, 2000).

[8] M. I. Mishchenko, Journal of Quantitative Spectroscopy and Radiative Transfer **110**, 1210 (2009).

[9] S. Yushanov, J. S. Crompton, and K. C. Koppenhoefer, in *Proceedings of the COMSOL Conference*, Vol. 116 (Cosmol Inc. Boston, 2013) pp. 1–7.

[10] W. Hergert and T. Wessels, eds., *The Mie Theory: Basics and Applications*, Springer Series in Optical Sciences, Vol. 169 (Springer-Verlag, Berlin, Heidelberg, 2012).

[11] M. J. Cheng, Y. C. Cao, K. F. Ren, H. Zhang, and L. X. Guo, Frontiers in Physics **12**, 1 (2024).

[12] F. Hussain, J. Hussain, S. S. Khanam, S. Noorani, A. B. Bhattacherjee, and S. Roy, Scattering phase functions and polarimetric responses of selected bioparticles, in *Optical Polarimetric Modalities for Biomedical Research*, edited by N. Mazumder, Y. V. Kistenev, E. Borisova, and S. Prasada K. (Springer International Publishing, Cham, 2023).

[13] P. Laven, Applied Optics **44**, 5667 (2005).

[14] F. Hussain, H. P. Jaishi, and S. Roy, Journal of Physics: Conference Series **2919**, 012046 (2024).

[15] F. Hussain, H. P. Jaishi, and S. Roy, in *Emerging Trends in Physical Science*, edited by B. Choudhury, D. P. Mahanta, and S. K. Sharma (Anundoram Borooah Academic Society, Assam, India, 2024).

[16] J. M. Steinke and A. P. Shepherd, Appl. Opt. **27**, 4027 (1988).

[17] F. Hussain, N. Mazumder, and S. Roy, Lasers in Medical Science **38**, 107 (2023).

[18] V. J. Dennis, Just Agriculture **2**, 1 (2021), e-ISSN: 2582-8223.

[19] A. Venugopal, K. A. Rinu, and D. Joseph, Innoriginal International Journal of Sciences **4**, 1 (2017).

[20] F. Hussain and S. Roy, The European Physical Journal Plus **139**, 687 (2024).

[21] S. Roy, F. Hussain, and N. Mazumder, Discover Applied Sciences **7**, 235 (2025).

[22] S. Roy, R. Mahatta, N. Barua, A. K. Buragohain, and G. A. Ahmed, Journal of Quantitative Spectroscopy and Radiative Transfer **112**, 1784 (2011).

MULTIFUNCTIONAL PERFORMANCE OF PVA-PVP/ZnO NANOCOMPOSITES: OPTICAL, DIELECTRIC AND AC CONDUCTIVITY ANALYSIS

T. Suma Chanu[1,3*], K. Jugeshwar Singh[2], and K. Nomita Devi[1]

[1]*Department of Physics, Manipur University, Canchipur, Imphal-795003, India*
[2]*Talent Development Centre, Indian Institute of Science, Kudapura, Karnataka-577536, India*
[3]*Centre of Plasma Physics-Institute for Plasma Research, Sonapur, Assam-782402, India*

[*]Corresponding Author: sumatoijam1@gmail.com

(Received 15 September 2025; revised 17 November 2025; accepted 23 November 2025; published 6 April 2026)

Abstract: Polyvinyl alcohol/Polyvinyl pyrrolidone/Zinc oxide (PVA/PVP/ZnO) polymer blend nanocomposites has been prepared to explore their optical and transport properties. The prepared sample are characterized by X-ray diffraction, Atomic force microscope, Energy-dispersive X-ray analysis, UV-visible spectroscopy and Fourier transform infra-red for structural, morphological, elemental and optical properties. The gradual reduction in the optical band gap energy from 5.30 eV to 2.10 eV is observed when the ZnO content in the PVA/PVP blend matrix increases. The nanocomposites also exhibit negligible transmittance in the UV region, indicating their potential for UV-shielding applications. The dielectric constant values of these nanocomposites are found in the range 14-23 with dielectric loss value of 0.06. The conduction mechanism observed in AC conductivity for all samples is governed by small polaron tunnelling model (SPTM). These results suggest that PVA/PVP/ZnO nanocomposites are suitable candidates for use as an insulator in the development of microelectronic device applications.

Keywords: Polymer blend, Optical properties, dielectric constant, dielectric loss, AC conductivity

PACS: 78.67.Sc, 77.84.Jd, 72.80.Le, 82.35.Np

1 Introduction

Polymer characteristics can be enhanced by blending two or more polymers and incorporating inorganic nanoparticles (NPs) as fillers, enabling their application in areas such as biomedical, thermal conductor, optoelectronics, and electrical insulation [1, 2]. Hydrophilic polymer blends, particularly PVA and PVP, are widely explored for fabricating functional polymer nanocomposites due to their miscible nature. This strong miscibility originates from hydrogen bond formation between the -OH groups of PVA and the C=O groups of PVP. These functional groups effectively interact with various nanofillers, resulting in the development of polymer nanocomposites (PNCs) and complexes with enhanced properties. Such materials are highly desirable for fabricating both current and future biodegradable optoelectronic, microelectronic, and energy storage devices [3, 4]. To optimize the desired thermophysical, dielectric, and electrical properties in flexible nanodielectric polymer matrices, ZnO NPs is often used as filler in the formation of polymer blend nanocomposites (NCs) due to its wide bandgap energy (3.3 eV) and large exciton binding energy (60 meV) [5]. ZnO has been widely utilised in various applications including luminescent and lasing devices, transparent conducting electrodes, ultraviolet blockers, photocatalysts, thin-film transistors, and light-emitting devices [6, 7]. S. H. Zyoud et al. [8] studied on the dielectric and optical parameters of the PVA/PVP/ZnO blend nanocomposite films with different concentration of ZnO (0-5.5 wt%). The results showed that these materials are promising potential in electronic devices and nonlinear optics. S. Jambaladinni et al. [9] investigated the role of ZnO nanofillers (0-15 wt%) on the optical and frequency dependent dielectric and dc conductivity properties of PVA/PVP/ZnO blend polymer, favouring the nanocomposite for potential application in

electromagnetic-induction (EMI). In the present work, optical, dielectric and AC conductivity characteristics of PVA/PVP blend based PNC films with higher loading percentages of ZnO (0, 5, 10, 15 and 20 wt%) has been studied which have been scarcely explored in earlier reports to evaluate their potential in optoelectronic and electronic device applications.

PVA/PVP/ZnO NCs containing varying concentrations of ZnO nanoparticles were synthesized using a simple and economical solution casting method. X-ray diffraction (XRD), Atomic force microscope (AFM), Energy dispersive X-ray analysis (EDX) and UV-visible spectroscopy (UV-Vis) are used to characterize the structural, morphological, elemental composition and optical behaviour of the nanocomposites. Dielectric response and AC conductivity of the samples were examined over a temperature range of 303K-393K and frequency range of 100Hz-1MHz.

2 Experimental

2.1 Materials required

Zinc nitrate tetrahydrate $(\mathrm{Zn(NO_3)_2 \cdot 4H_2O})$, sodium hydroxide (NaOH) procured from MERCK are used as precursor and precipitating agent respectively. Polyvinyl alcohol (PVA) and polyvinyl pyrrolidone (PVP) obtained from Sigma Aldrich are used as polymer for the preparation of NCs. Distilled water is employed as the solvent throughout the synthesis procedure.

2.2 Preparation of PVA/PVP/ZnO nanocomposites (PPZ NCs)

ZnO nanoparticles used in this work were synthesized as reported in our previous study [10]. PVA/PVP/ZnO NCs with different ZnO nanoparticle loadings were obtained through solution casting method. In a typical process, 3g of PVA and 3g of PVP were dissolved in 100ml of distilled water under continuously stirring until clear solution were obtained. The two polymer solutions were then combined and stirred for 2hr to form a homogenous blend. This mixture was divided into five equal portions, after which ZnO nanoparticles were incorporated at concentrations 0, 5, 10, 15 and 20 wt% respectively. Each suspension was ultrasonicated for 1hr and further stirred for 24hr to obtain an even dispersion of nanoparticles within the polymer blend matrix. The resulting solutions were placed in Petri dish and dried at 50°C for 5 hr in an oven. The PVA/PVP/ZnO NCs were labelled as PPZ0, PPZ5, PPZ10, PPZ15, and PPZ20 representing the pure PVA/PVP blend and nanocomposites with 5, 10, 15 and 20 wt% of ZnO NPs content respectively. The films showed an average thickness of approximately $45\mu m \pm 1\mu m$. Fig. 1 depicts the schematic representation of the fabrication procedure.

Figure 1: Schematic representation for the preparation of PVA/PVP/ZnO nanocomposites.

3 Characterization

The crystalline structure of the synthesized nanocomposites was analyzed using Phillip's `PANanalytical X'Pert PRO` diffractometer equipped with a Cu target (λ=1.5405Å) operating over a 2θ range of $10° - 80°$. Surface morphology was characterized by atomic force microscope (AFM). Elemental composition was determined

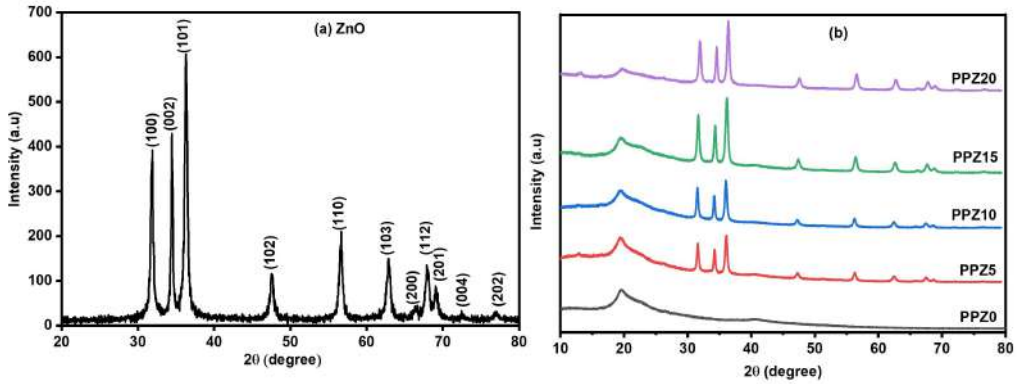

Figure 2: XRD spectra for (a) ZnO NPs and (b) PPZ nanocomposites

using energy dispersive X-ray analysis (EDX) with an `Apollo SDD` detector attached to a SEM `FEI QUANTA 250`. Optical absorption measurement was carried out using UV-visible spectrophotometer (`PerkinElmer Lambda 365`). Fourier transform infra-red (FTIR) spectroscopy analysis was carried out on PerkinElmer Spectrum Two spectrometer over 400cm^{-1} − 4000cm^{-1} while the dielectric response and AC conductivity of the samples were studied from 303K-393K and 100Hz-1MHz using `Agilent 4284A` LCR meter.

4 Results and discussion

4.1 X-ray diffraction (XRD) study

Fig. 2(a) and (b) shows the XRD spectra for ZnO NPs and PPZ NCs with various concentration of ZnO nanoparticles. Crystallite size of ZnO NPs calculated using the Scherrer formula was 20 nm [11]. In PVA/PVP blend NCs, the presence of two broad and intense peaks observed at angles $2\theta = 19.57°$ and $40.43°$ is attributed to the presence of PVA molecules [12] while the PVP exhibits two diffused halos peaks at angles $2\theta = 12.87°$ and $21.80°$ confirming its amorphous structure [13]. Upon incorporation of ZnO nanoparticles into the polymer blend matrix, characteristics ZnO diffraction peaks appear together with those of PVA and PVP. The enhancement of ZnO peak intensities as the filler concentration rises indicates the successful formation of PVA/PVP/ZnO nanocomposites.

4.2 Atomic force microscope (AFM) analysis

Fig. 3 shows the 2D and 3D AFM surface topographical images of PPZ NCs. The corresponding surface roughness values of the nanocomposites expressed as arithmetic mean roughness Ra and the root mean square roughness Rrms determine through AFM analysis using `Gwyddion` software are summarised in Table 1. It is observed from the Table 1, that the surface roughness of the PPZ0 increases with the increase in concentration of ZnO nanoparticles. This rise in surface roughness serves as evidence that ZnO has been effectively incorporated into PPZ0 but also confirms the presence of some agglomeration among the dispersed nanofillers in the blend matrix.

Table 1: Surface topography values for the PVA/PVP/ZnO NCs films

Samples	R_a (nm)	R_{rms} (nm)
PPZ0	1.51	2.01
PPZ5	2.83	3.98
PPZ15	3.99	5.35
PPZ20	4.81	6.14

4.3 Energy dispersive X-ray (EDX) analysis

The EDX spectra for PPZ NCs are presented in Fig. 4(a-e). The PPZ0 sample present only carbon (C) and oxygen (O) as the constituent element whereas PPZ NCs observed the presence of Zn in addition to carbon and oxygen

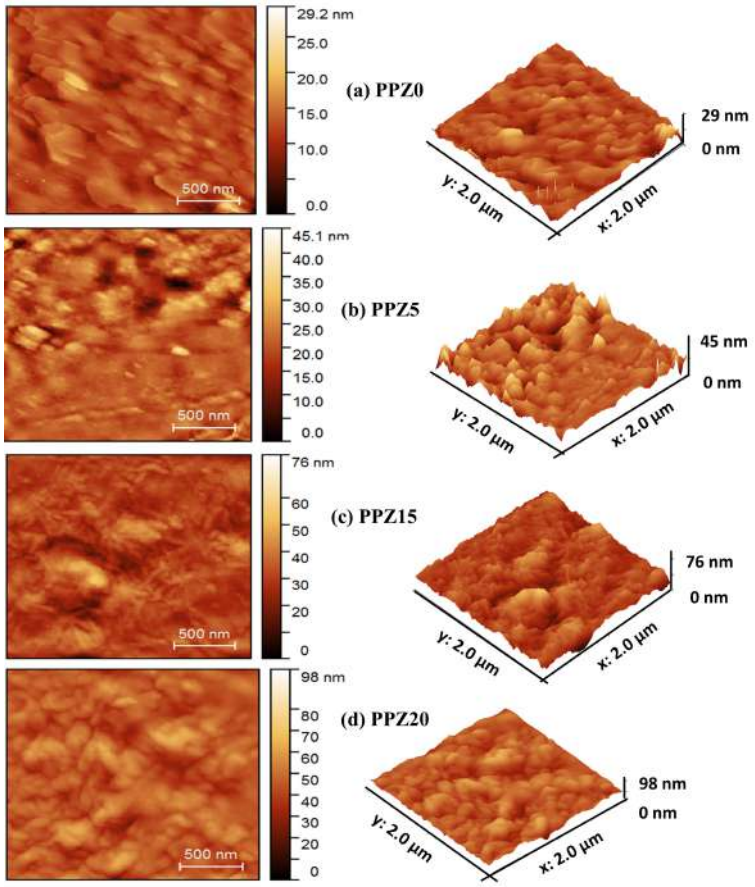

Figure 3: 2D (left side) and 3D (right side) AFM images for PPZ NCs: (a) PPZ0, (b) PPZ5, (c) PPZ15, (d) PPZ20

confirming the successful incorporation of ZnO into the polymer blend matrix. The appearance of two peaks corresponding to Zn in the EDX spectrum arises from the characteristic X-ray emission lines of zinc. The peak observed around 1.02 keV corresponds to the $L\alpha$ emission lines of Zn, while the peaks observed approximately at 8.63 keV are associated with the $K\alpha$ emission lines of Zn.

4.4 UV-visible absorbance spectra

Fig. 5 presented the UV-Vis absorbance spectra for PPZ nanocomposites. The PPZ NCs showed the absorption within the wavelength range of 225-454 nm. With increasing ZnO NPs content in the PVA/PVP blend matrix, an absorption peaks shift toward longer wavelength with varying absorption intensities. In the UV region of the PPZ NCs, there is noticeable light scattering which might be attributed to the increased surface roughness as also evident from the AFM images.

The optical band gap energy is determined using the Tauc's equation (1) from the absorbance spectra

$$(\alpha h\nu)^n = \beta(h\nu - E_g) \tag{1}$$

where α denotes the absorption co-efficient, $h\nu$ represents the photon energy, E_g correspond to the band gap energy, β is the proportionality constant. The exponent n is determined by the nature of the electronic transition with a value of $\frac{1}{2}$ for direct allowed transition and 2 for indirect allowed transition.

The optical band gap energy for direct allowed transition for each sample determined by extrapolating the linear portion of the $(\alpha h\nu)^2$ versus $(h\nu)$ curve to its interaction with the photon energy axis as shown in Fig. 6. From the Tauc's plot, the direct band gap energy for PPZ0, PPZ5, PPZ10, PPZ15 and PPZ20 are 5.30eV, 2.66eV, 2.39eV, 2.19eV and 2.10eV respectively. The introduction of ZnO nanoparticles into the PVA/PVP matrix induces a decrease in band gap energy. This reduction is attributed to the formation of structural defects in the polymer blend matrix caused by the presence of ZnO [14, 15]. The structural defect produces localized state

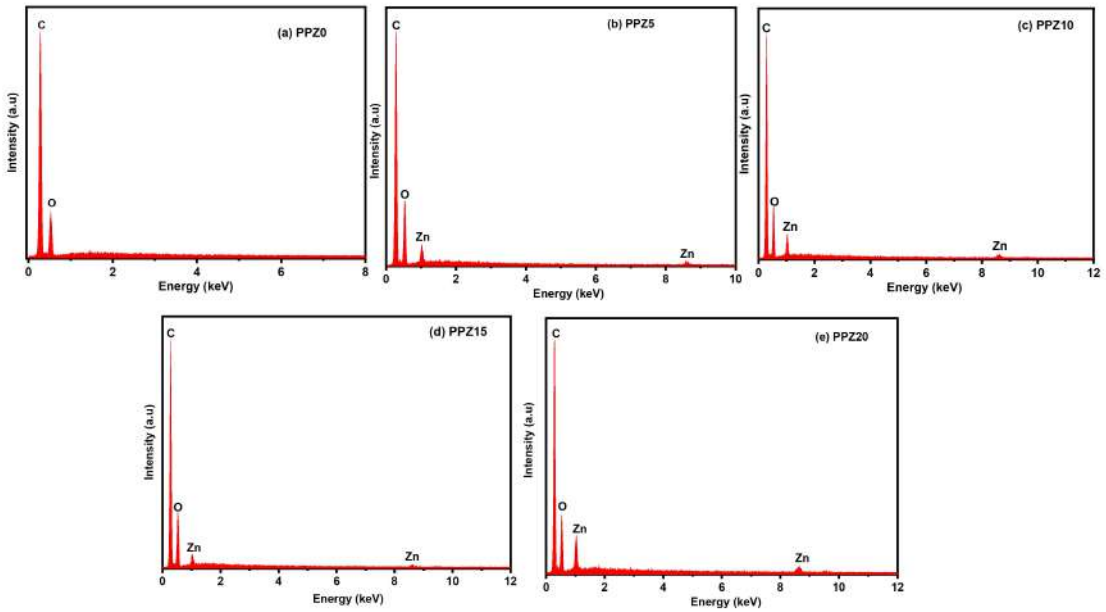

Figure 4: EDX spectra for PPZ NCs: (a) PPZ0, (b) PPZ5, (c) PPZ10, (d) PPZ15, (e) PPZ20

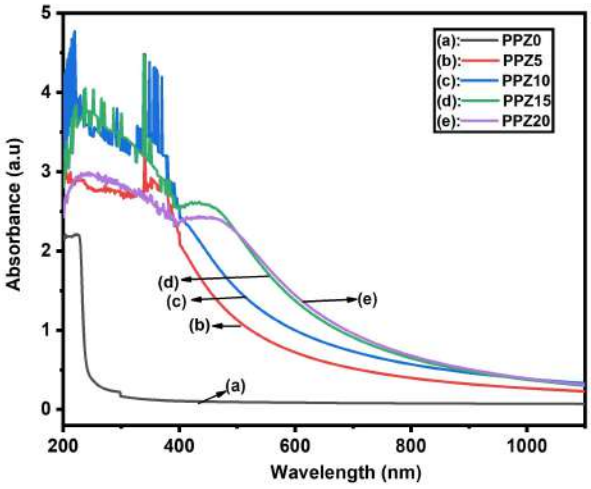

Figure 5: UV-visible absorbance spectra for PPZ nanocomposites: (a) PPZ0, (b) PPZ5, (c) PPZ10, (d) PPZ15 and (e) PPZ20

between highest occupied molecular orbital (HOMO) and the lowest unoccupied molecular orbital (LUMO) of the polymers. As the concentration of ZnO rises within the polymer blend matrix, the number of localized states also increases. These localized states create opportunities for electrons to transition from the valence band to these localized states, or from the localized states to the conduction band, all at energy levels lower than the material's band gap energy. This interplay gives rise to the absorption or emission of photons with energies lower than the band gap energy, effectively causing a reduction in the material's optical band gap [16, 17].

4.5 UV-visible transmittance spectra

Fig. 7 illustrates the UV-visible transmittance spectra of PPZ NCs recorded over the wavelength range of 200 nm-1100nm. As the loading of ZnO nanoparticles within the PVA/PVP blend increases, a gradual decline in transmittance is observed in the visible region, while the ultraviolet region exhibits nearly complete absorption. The

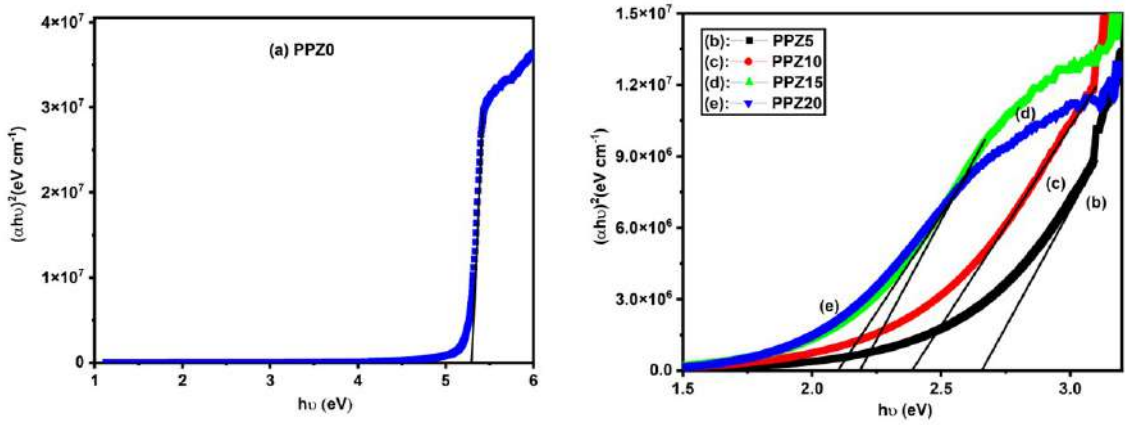

Figure 6: Tauc's plot of $[(\alpha h\nu)^2$ vs. $(h\nu)]$ for PPZ NCs: (a) PPZ0 and (b) PPZ5, PPZ10, PPZ15, PPZ20 NCs.

negligible UV transmittance can be explained by the strong absorption of short-wavelength radiation by electrons in the outer energy levels of ZnO nanoparticles, which become excited to higher energy states and consequently prevent a portion of the incident radiation from passing through the material. Conversely, the pure PVA/PVP polymer blend contains no free charge carriers or intermediate energy states between the HOMO and LUMO levels, and therefore requires photons of higher energy for electronic excitation, resulting in higher transparency. These results demonstrate that the synthesized PPZ NCs possess strong UV-shielding characteristics, making them suitable for UV-protective applications [15, 18].

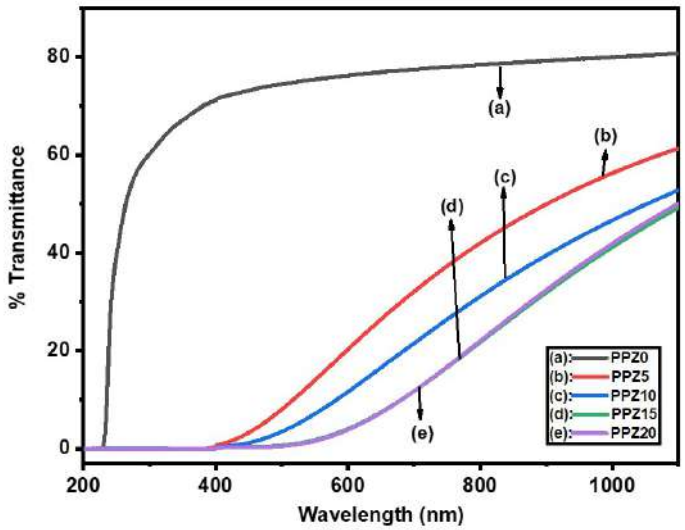

Figure 7: UV-visible transmittance spectra for PPZ nanocomposites: (a) PPZ0, (b) PPZ5, (c) PPZ10, (d) PPZ15, (e) PPZ20

4.6 Fourier transform infra-red analysis

Fig. 8 shows the FTIR spectra for PPZ nanocomposites. A broad and intense absorption band appeared in all samples in the range of 3000 cm^{-1}-3600 cm^{-1} is attributed to the stretching vibration of hydroxyl group (-OH) and slight shifted towards the higher wavenumber with the increasing ZnO nanoparticles content. A band at 2941 cm^{-1} corresponds to the -CH stretching vibration of PVA and PVP. The C=O stretching mode is ascribed at 1658 cm^{-1}. The combination band of (CH+CC) group is identified at 1245 cm^{-1}. The band at 1283 cm^{-1} is attributed to C-N bending vibration. The stretching mode of C-C group are seen at 917cm^{-1} and 852cm^{-1}. The band at 570cm^{-1} is assigned to N-C=O bending vibration. The band at 1080cm^{-1}- arises from the stretching vibration of

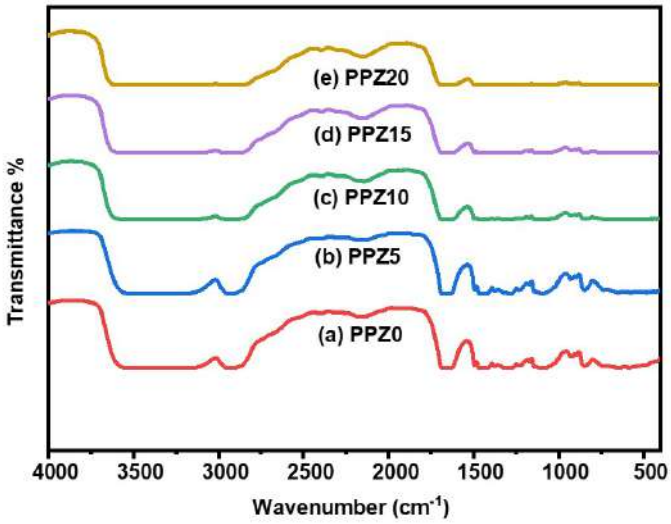

Figure 8: FTIR spectra for PPZ nanocomposites: (a) PPZ0, (b): PPZ5, (c) PPZ10, (d) PPZ15, (e):PPZ20

C-O groups of PVA and a strong band at 1658cm^{-1} is attributed to the C=O stretching vibration of PVP. All the characteristic absorption band observed in the nanocomposites are agrees well with the previous reports [19–21]. As the concentration of ZnO nanoparticles increase, the intensities of some bands are decreased, becomes wider as well as slightly shifted to longer wavelength. This indicates the strong interfacial interaction between the ZnO and miscible chain structure of PVA/PVP.

5 Dielectric properties

5.1 Dielectric constant

For each sample the dielectric constant is evaluated using the expression, $\epsilon = \frac{Cd}{\epsilon_0 A}$, where C denotes the capacitance, d signifies film thickness, A represent film area, ϵ_0 is the permittivity of free space. Fig. 9 depicts the dependence of dielectric constant on frequency at various temperature and variation of dielectric constant with temperature at fixed frequency (inset) for PPZ NCs. The dielectric permittivity of all samples exhibits high values in the low frequency region and gradually declines as the frequency increases. The low frequency response is predominantly controlled by the interfacial polarization commonly referred to as Maxwell-Wagner-Sillars (MWS) mechanism, which is the characteristic feature of polymer-based nanocomposite. In the present samples, semiconducting fillers dispersed within the PVA/PVP polymer blend promotes the charge build up at the filler-polymer interfaces. Variations in charge distribution across these interfaces lead to the formation of large number of micro-capacitors like regions throughout the material which effectively behave as dipoles [10, 22, 23]. At low frequencies, these dipoles can easily orient in response to the applied electric field, resulting in strong polarization and high dielectric permittivity. With increasing frequency, dipole orientation becomes progressively hindered, leading to a decrease in the dielectric constant.

In addition, it can be observed that the dielectric constant of all samples rises with the increasing temperature at a given frequency. At lower temperature, the polymer films exhibit smaller dielectric constant values because limited thermal energy restricts dipole motion, rendering the dipoles associated with the micro-capacitive regions and the polar PVA/PVP matrix relatively immobile and less responsive to the applied electric field. As the temperature increases, the flexibility of polymer chain, polar functional groups and dipolar species within the system improves. This increased molecular mobility shortens the relaxation time of both polymer segments and dipoles, allowing them to respond more readily to variations in the external electric field. As a result, an enhancement in dielectric constant is observed [15, 24, 25]. Fig. 9(f) shows the variation of dielectric constant with frequency for different concentration of ZnO nanoparticles at 393K. From the graph, it is observed that the dielectric constant value of PPZ0, PPZ5, PPZ10, PPZ15 and PPZ20 does not vary much with values of 14, 15, 13, 16 and 23 respectively. Such PPZ NCs which has lower dielectric constant value suggests their suitability for use as an insulator in the fabrication of micro electronic device applications.

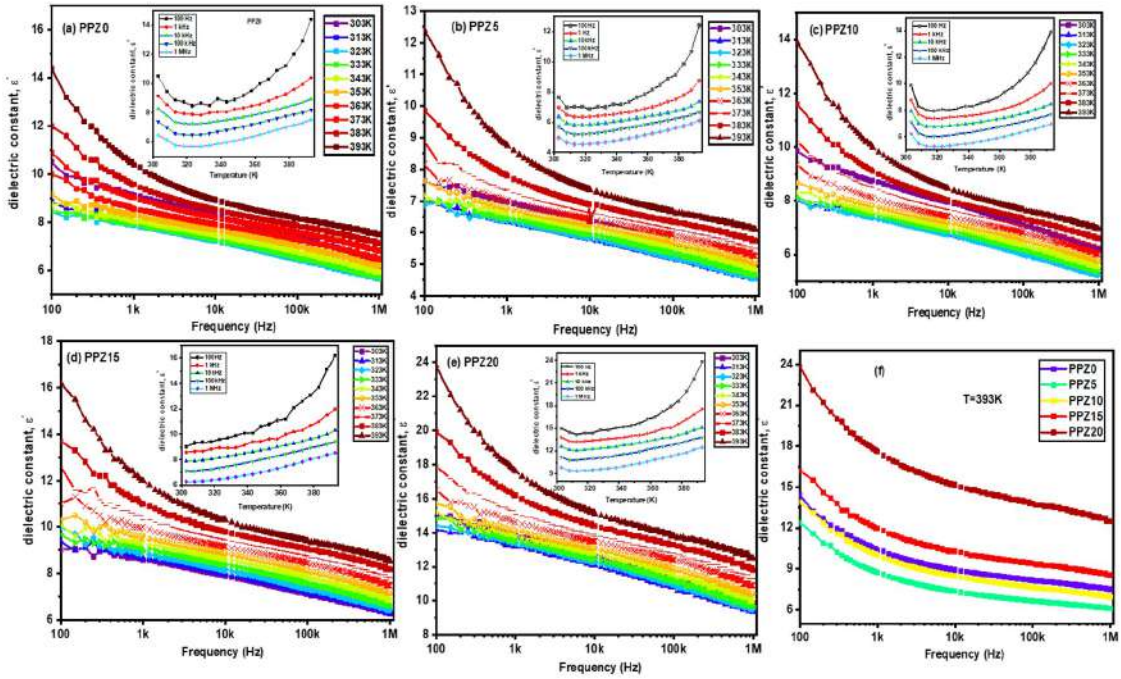

Figure 9: Frequency variation of dielectric constant at different temperatures and temperature-dependent dielectric constant (inset) at a fixed frequency for PPZ nanocomposites: (a) PPZ0, (b) PPZ5, (c)PPZ10, (d) PPZ15, (e) PPZ20 and (f) frequency-dependent dielectric behaviour for different PPZ NC loadings.

5.2 Dielectric loss

Fig. 10(a-e) illustrate the frequency-dependent dielectric loss of PPZ nanocomposites measured at different temperature, along with the temperature variation of dielectric loss at a chosen frequency shown in inset graph. The samples exhibit relatively high dielectric loss in the low-frequency region, which is mainly attributed to interfacial polarization effect. As the frequency increases, the dipoles are unable to keep pace with the rapid oscillations of the applied electric field, leading to a gradual reduction in the dielectric loss. The inset plot further reveals that dielectric loss increases with the increasing temperature. This behaviour can be explained by the formation of additional free volume within the polymer blend matrix at elevated temperature, which facilitates dipolar reorientation and thereby enhances dielectric loss [26–29]. Moreover, the dielectric loss values decrease from approximately 0.9 at low frequencies to about 0.06 at frequencies above 100 kHz for all samples, as shown in Fig. 10(f). The observed low dielectric loss at higher frequencies indicates that these nanocomposites are promising candidates for low-loss dielectric applications.

5.3 AC Conductivity

The AC conductivity for each sample is evaluated using Eq. (2) by utilizing the dielectric constant and dielectric loss data derived from dielectric measurements over the temperature range of 303K-393 K and the frequency range of 100Hz -1MHz to further understand the electrical conduction mechanism.

$$\sigma_{ac} = 2\pi f \epsilon \epsilon_0 \tan\delta \tag{2}$$

Here, f represents the frequency of the applied electric field, ϵ_0 denotes the permittivity of free space, ϵ corresponds to the dielectric constant, and $\tan\delta$ refers to the dielectric loss tangent.

Fig. 11(a-e) displays AC conductivity varies with frequency for all samples at specific temperature. It is observed from the graph that the AC conductivity for all the samples shows a linear behaviour upto a frequency of 10kHz and then increased non-linearly at higher frequency. The linear response in the low frequency region indicates that charge transport is dominated by the localized motion of charge carrier associated with interfacial polarization arising from Maxwell-Wagner-Sillars effect. Whereas the non-linear dispersion at higher frequency over the frequency range 10kHz to 1MHz is attributed to the motion of localized charge carrier over the shorter

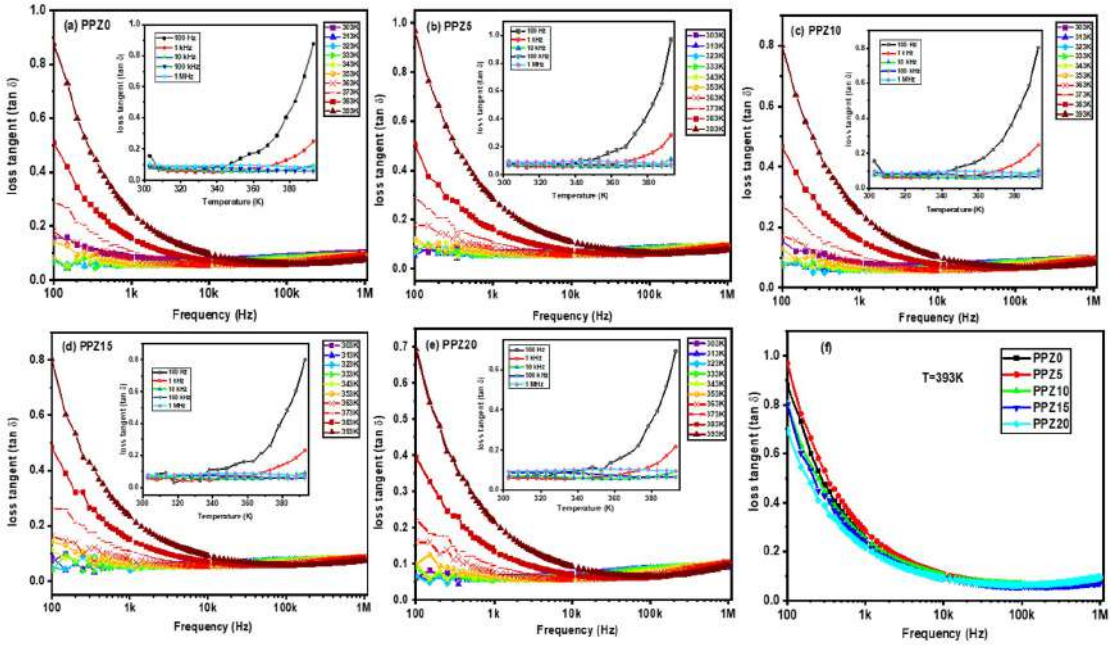

Figure 10: Frequency variation of dielectric loss at various temperature and temperature dependent dielectric loss at a fixed frequency for PPZ nanocomposites: (a) PPZ0, (b) PPZ5, (c) PPZ10, (d) PPZ15, (e) PPZ20 and (f) Frequency dependent dielectric loss for PPZ NCs.

path. The AC conductivity values for all samples at 100Hz for 313K are around 10^{-9}(S/m) and at 393K are around 10^{-7}(S/m). The values of AC conductivity increase with the increase in frequency and found to be 10^{-5}(S/m) at 1MHz. Such low conductivity value indicates that these NCs are promising materials for use as flexible dielectric substrates and insulating layers in biodegradable electronic devices. The conductivity data is evaluated using the

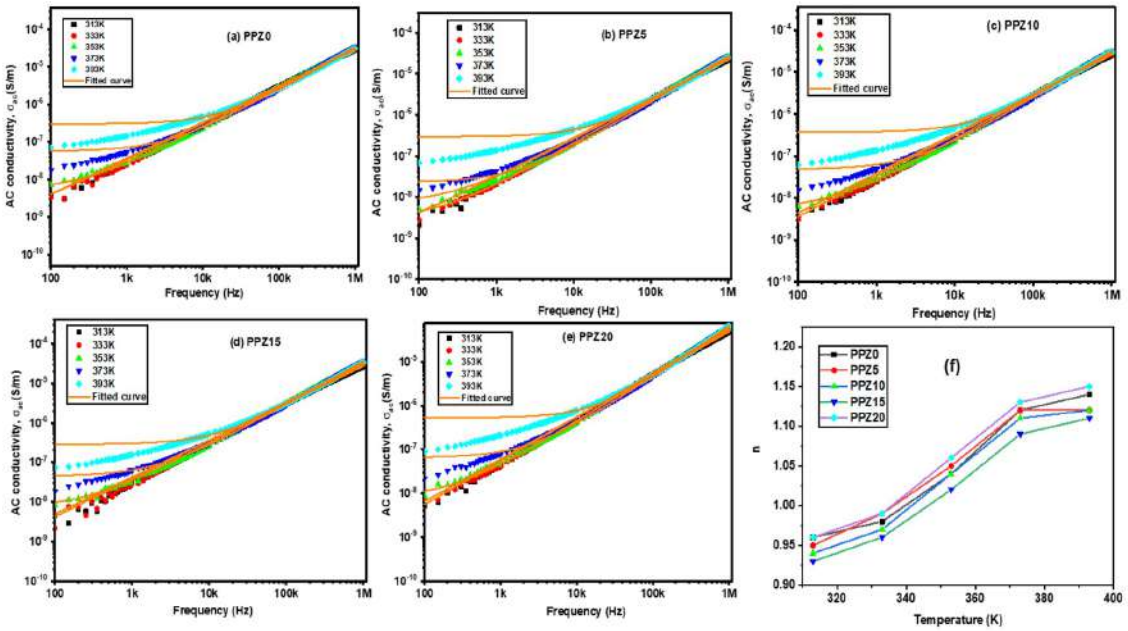

Figure 11: Frequency variation of AC conductivity for PPZ nanocomposites at selected temperature: (a) PPZ0 (b) PPZ5 (c) PPZ10 (d) PPZ15 (e)PPZ20 and (f) Variation of the fit parameter 'n' with temperature.

Jonscher's power law relation expressed as, $\sigma(f) = \sigma_0 + Af^n$. In this relation $\sigma(f)$ denotes the total conductivity, σ_0 represents the dc component of the conductivity, A is the constant related to the strength of the polarizability and n is the frequency exponent that describes the extent of interaction between charge carriers and the lattice. Several theoretical models have been proposed to describe charge transport based on the behavior of n, including the Quantum Mechanical Tunnelling (QMT) model, where n depends on frequency but remains independent of temperature; the Correlated Barrier Hopping (CBH) model, in which n decreases with increasing temperature; the Small Polaron Tunnelling (SPT) model, where n increases with temperature; and the Large Polaron Quantum Mechanical Tunnelling (LPQMT) model, in which n initially decreases to a minimum and then increases as temperature rises. As shown in Fig. 11(f), the value of n increases with temperature, indicating that charge transport in PPZ NCs follows the small polaron tunnelling mechanism [30].

6 Conclusion

PVA/PVP/ZnO nanocomposites containing different ZnO loadings (0, 5, 10, 15, and 20wt%) were synthesized using the solution casting technique. The formation of polymer nanocomposites and the purity of the samples were confirmed through XRD and EDX analyses. AFM images indicate that incorporating ZnO nanoparticles leads to an increase in surface roughness. The band gap energy of the nanocomposites decreases with the increasing concentration of ZnO from 5.30eV to 2.10eV. UV-visible transmittance studies revealed a decrease in transmittance with increasing ZnO concentration, effectively blocking UV radiation, rendering them suitable for UV-shielding applications. FTIR results demonstrate physical interactions between ZnO nanoparticles and the hydroxyl groups of PVA as well as the carbonyl groups of PVP. The dielectric constant values at 393K for PPZ0, PPZ5, PPZ10, PPZ15, and PPZ20 are 14, 15, 13, 16, and 23 respectively. The value of dielectric loss for all samples at lower frequency is of the order of around 0.9 which reduces to 0.06 at higher frequency (above 100 kHz). The values of AC conductivity increase with the increase in frequency and found to be 10^{-5}(S/m) at 1MHz. The frequency-dependent conductivity behaviour follows Jonscher's power law, and the dominant conduction process is attributed to the small polaron tunnelling model. The combination of low dielectric constant, low dielectric loss, and AC conductivity suggests that these nanocomposites are promising candidates as flexible nanodielectric substrates and insulating materials for microelectronic device fabrication.

References

[1] S. Mallakpour and M. Khani, Colloid and Polymer Science **294**, 583 (2016).

[2] D. Rithesh Raj, S. Prasanth, T. Vineeshkumar, and C. Sudarsanakumar, Optics Communications **340**, 86 (2015).

[3] K. Rajesh, V. Crasta, N. B. Rithin Kumar, G. Shetty, and P. D. Rekha, Journal of Polymer Research **26**, 99 (2019).

[4] P. Dhatarwal and R. J. Sengwa, Advanced Composites and Hybrid Materials **3**, 344 (2020).

[5] S. Shinde, P. Shinde, Y. Oh, D. Haranath, C. Bhosale, and K. Rajpure, Applied Surface Science **258**, 9969 (2012).

[6] H. Kim, C. M. Gilmore, J. S. Horwitz, A. Piqué, H. Murata, G. P. Kushto, R. Schlaf, Z. H. Kafafi, and D. B. Chrisey, Applied Physics Letters **76**, 259 (2000).

[7] Özgür, Y. I. Alivov, C. Liu, A. Teke, M. A. Reshchikov, S. Doğan, V. Avrutin, S.-J. Cho, and H. Morkoç, Journal of Applied Physics **98**, 041301 (2005).

[8] S. H. Zyoud, T. H. AlAbdulaal, A. Almoadi, M. S. Alqahtani, F. A. Harraz, M. S. Al-Assiri, I. S. Yahia, H. Y. Zahran, M. I. Mohammed, and M. S. Abdel-wahab, Crystals **13** (2023).

[9] S. Jambaladinni and J. S. Bhat, Iranian Journal of Science and Technology, Transactions A: Science **45**, 1851 (2021).

[10] T. S. Chanu, K. J. Singh, W. J. Singh, and K. N. Devi, Physica Status Solidi (A) **220**, 2300531.

[11] T. Suma Chanu, K. Jugeshwar Singh, and K. Nomita Devi, Materials Today: Proceedings **65**, 2844 (2022).

[12] P. L. Reddy, K. Deshmukh, K. Chidambaram, M. M. N. Ali, K. K. Sadasivuni, Y. R. Kumar, R. Lakshmipathy, and S. K. K. Pasha, Journal of Materials Science: Materials in Electronics **30**, 4676 (2019).

[13] P. Dhatarwal, S. Choudhary, and R. Sengwa, Materials Letters **273**, 127913 (2020).

[14] J. Rozra, I. Saini, A. Sharma, N. Chandak, S. Aggarwal, R. Dhiman, and P. K. Sharma, Materials Chemistry and Physics **134**, 1121 (2012).

[15] T. S. Chanu, K. J. Singh, and K. N. Devi, Polymer Bulletin **81**, 5069 (2024).

[16] K. Hemalatha, K. Rukmani, N. Suriyamurthy, and B. Nagabhushana, Materials Research Bulletin **51**, 438 (2014).

[17] J. Rozra, I. Saini, A. Sharma, N. Chandak, S. Aggarwal, R. Dhiman, and P. K. Sharma, Materials Chemistry and Physics **134**, 1121 (2012).

[18] H. S. Roy, M. Y. A. Mollah, M. M. Islam, and M. A. B. H. Susan, Polymer Bulletin **75**, 5629 (2018).

[19] C. L. Raju, J. L. Rao, B. C. V. Reddy, and K. Veera Brahmam, Bulletin of Materials Science **30**, 215 (2007).

[20] M. M. Rahman Khan, S. Pal, M. M. Hoque, M. R. Alam, M. Younus, and H. Kobayashi, ACS Omega **4**, 6144 (2019).

[21] E. M. Abdelrazek, A. M. Abdelghany, A. E. Tarabiah, and H. M. Zidan, Journal of Materials Science: Materials in Electronics **30**, 15521 (2019).

[22] K. S. Hemalatha, G. Sriprakash, M. V. N. Ambika Prasad, R. Damle, and K. Rukmani, Journal of Applied Physics **118**, 154103 (2015).

[23] R. C. Smith, C. Liang, M. Landry, J. K. Nelson, and L. S. Schadler, IEEE Transactions on Dielectrics and Electrical Insulation **15**, 187 (2008).

[24] A. H. Mohamad, O. G. Abdullah, and S. R. Saeed, Results in Physics **16**, 102898 (2020).

[25] B. M. Baraker and B. Lobo, Bulletin of Materials Science **42**, 18 (2019).

[26] M. S. Gaur, A. P. Indolia, A. A. Rogachev, and A. V. Rahachou, Journal of Thermal Analysis and Calorimetry **122**, 1403 (2015).

[27] P. Mukherjee, A. Das, B. Dutta, and A. Meikap, Journal of Physics and Chemistry of Solids **111**, 266 (2017).

[28] R. J. Sengwa, S. Choudhary, and P. Dhatarwal, Advanced Composites and Hybrid Materials **2**, 162 (2019).

[29] S. Choudhary, Polymer Composites **39**, E1788.

[30] M. Dult, R. Kundu, J. Hooda, S. Murugavel, R. Punia, and N. Kishore, Journal of Non-Crystalline Solids **423-424**, 1 (2015).

PANE Journal of Physics P. J. Phys. 02 (01), 033 (April 2026)

ENHANCED PHOTOCATALYTIC ACTIVITY OF MOF-DERIVED ZnO NANOPARTICLES FOR DYE DEGRADATION

Salam Jogita Chanu[1], L. Anju Chanu [1], and K. Nomita Devi[1*]

[1]*Department of Physics, Manipur University, Canchipur, Imphal 795003, India*

[*]Corresponding Author: kongkhamn@gmail.com

(Received 8 September 2025; revised 4 December 2025; accepted 5 December 2025; published 6 April 2026)

Abstract: In this study, the photocatalytic performance of Metal-Organic Framework (MOF) derived ZnO has been shown to be more efficient than the pure ZnO for Malachite Green (MG) dye degradation, a commonly used organic dye having considerable environmental influence. ZnO in pure form was prepared by chemical coprecipitation method and MOF-derived ZnO was prepared by self-assembly process. X-ray diffraction (XRD), energy dispersive X-ray spectroscopy (EDX), Field emission scanning electron microscope (FESEM), Fourier-transform infrared spectroscopy (FTIR), and UV-visible spectroscopy (UV-vis) were utilized to characterize the materials. XRD established that the two materials crystallize in the hexagonal wurtzite form, and FESEM established that pure ZnO was made up of both spherical and spindle-like particles, and MOF-derived ZnO consisted of mostly spherical particles. The UV-visible absorption spectra showed that both samples had bandgap energies of 3.32 eV. The photocatalytic performance (under UV light irradiation) of MOF-derived ZnO was excellent, as it was able to degrade MG dye by 98% in 3 hours. Such enhancement may be ascribed to the increased effective surface area and increased porosity of the MOF-derived structure which allows more effective photocatalysis.

Keywords: Metal-Organic Framework (MOF), Malachite Green, photocatalytic activity

PACS: 78.67.Bf, 61.46.-w, 78.67.-n, 78.40.-q

1 Introduction

Over the past century, the global demand of freshwater has increased owing to economic growth, population escalation and change in usage patterns. On the other hand, domestic, industrial, agricultural, and municipal activities, are exhausting the water resources increasing the water shortage and pollution, thereby making access to clean water one of the most pressing issues of modern society [1]. Among various pollutants, the wastewater of industrial productions like textiles, dye manufacturing, apparel, paper pulp, tanneries and printing is one of the major source of contamination [2]. Heavy metals (Zn, Ni, Cd, Cu, Pb, Hg, etc.), organic dyes ($e.g.$, methylene blue, Rhodamine B, malachite green), toxic chemicals, pesticides, herbicides, hydrocarbons, pharmaceuticals, $etc.$ are some of the harmful pollutants found in this industrial wastewater [3, 4]. Some of these chemicals are harmful, mutagenic, persistent in nature, and possess carcinogenic properties, creating a serious threat to both human health and environment [3, 5]. As per the World Health Organization (WHO), the textile industry accounts for approximately 17-20% of industrial wastewater pollution worldwide [6]. In the dyeing process, dyes are released into wastewater by 10-15%, which further degrades the quality of water [1, 6]. It is thus of much essence to manage the dye waste effectively before it is released to the environment to avoid the environmental pollution caused by the decomposition of dyes into forms that are non-toxic to the environment, reduction of contamination in the major water bodies, and effective elimination of the dyes in the aquatic environments.

The removal of dyes in wastewater has been done by applying various methods such as chemical precipitation, solvent extraction, coagulation-flocculation, biological treatments, and membrane filtration. Nevertheless, these

methods only transfer pollutants into sludge rather than completely eliminating them [4, 6]. To overcome these challenges, it is also requisite to have innovative, cost-effective, sustainable and energy efficient water purification process that can effectively remove contaminants with minimizing energy consumption and chemical usage [1, 7]. Advanced oxidation processes (AOPs) is an effective method of oxidizing and mineralizing diverse organic pollutants, which rely on highly reactive and strongly oxidizing radicals [7]. The high levels of efficacy in decontaminating pollutants to form less harmful byproducts and the high rates of degradation, as well as non-selective oxidation have made AOPs highly recognizable in wastewater treatment [4]. Semiconductor photocatalysis is one of the many AOPs that are highly effective in degrading toxic metal ions and organic pollutants [1, 2].

Photocatalysis, which is a process in which a semiconducting material produces electron-hole pairs in the presence of light of suitable wavelength. These charge carriers form reactive oxygen species (ROS), including superoxide anions ($O_2 \cdot^-$) and hydroxyl radicals ($\cdot OH$), when in contact with water and oxygen and have strong oxidizing capabilities [4, 8]. These ROS are effective in the degradation of organic pollutants into harmless byproducts [5, 7, 9–11]. Photocatalysis is a renewable and environmentally friendly technology, therefore, it can be used to effectively degrade persistent hazardous contaminants with the use of sunlight [5, 12]. Additionally, it operates at room temperature, which not only makes the elimination for the need of high energy input but ensures that the pollutants are effectively degraded [2, 13]. Different metal oxide semiconductors, which are TiO_2, $ZnO, Bi_2O_3, Fe_2O_4, WO_3, Cu_2O, SnO_2$, etc., are highly active photocatalytic materials that facilitate the mineralization of organic pollutants [1, 2, 14–16]. Among the various metal-oxide semiconductors, ZnO and TiO_2 are most prospective materials used in degrading organic pollutants because of their high chemical robustness, non-toxicity, and strong oxidative potential [1, 15, 17–19]. Nevertheless, TiO_2 has low quantum efficiency and a small surface area when compared to ZnO, which is emerging to be a superior alternative as it has greater surface area, better quantum yield, and increased photoluminescence [16, 20, 21].

Moreover, Metal-Organic Frameworks (MOFs) have become a focal point of research due to their exceptionally large surface areas as well as highly tunable structures [8]. By self-assembly of metal ions and multidentate linkers, these three-dimensional and highly porous organic-inorganic frameworks are formed. They are highly versatile with regards to chemical and structural properties due to their large surface area, substantial pore volume, and tunable composition. The porosity of the MOFs is inherent in ion storage and transport [21, 22]. They can be integrated with metal oxides, which opens the potential for energy storage, catalysis, and remediation of the environment [8, 22]. Pure ZnO and MOF-derived ZnO have been prepared in this study through chemical co-precipitation method and self-assembly method, respectively. The resulting photocatalyst were characterized by X-ray diffraction (XRD), Field emission scanning electron microscope (FESEM), energy-dispersive X-ray spectroscopy (EDX), Fourier-transform infrared spectroscopy (FTIR), and UV-visible spectroscopy (UV-vis). Their photocatalytic performance was subsequently evaluated for the degradation of Malachite Green dye.

2 Materials and Methods

2.1 Materials Required

In this study, analytical grade Zinc Nitrate Hexahydrate ($Zn(NO_3)_2 \cdot 6H_2O$, Sigma-Aldrich), 2-Methylimidazole ($C_6H_6N_2$, Sigma-Aldrich), Sodium Hydroxide (NaOH, Merck) and Malachite Green ($C_{23}H_{25}ClN_2$, Hi-Media) were used as reagent without further treatment. Distilled water (DI) is used as a solvent for the entire experiment.

2.2 Synthesis of pure ZnO

Pure ZnO nanoparticles were synthesized by the facile chemical co-precipitation method. Initially, 0.1 M of $Zn(NO_3)_2 \cdot 6H_2O$ was dispersed in 200 mL of deionised (DI) water and magnetically stirred for 30 min at room temperature (27°C). Similarly, 0.5 M NaOH solution in 300 ml of DI water was prepared with continuous stirring for 30 min. The NaOH solution was then introduced gradually into the $Zn(NO_3)_2 \cdot 6H_2O$ solution until the pH reached 12 and kept stirring for another 2 hours. The resulting precipitate was washed numerous times with DI water, dried in an oven at 80°C for about 2 days until it was completely dry and ground to obtain ZnO powder.

2.3 Synthesis of MOF-derived ZnO

MOF-derived ZnO nanoparticles were synthesized via a self-assembly process. The starting materials, $Zn(NO_3)_2 \cdot 6H_2O$ and 2-Methylimidazole, were used in a 1:4 molar ratio. 0.594g of $Zn(NO_3)_2 \cdot 6H_2O$ was dissolved in

50mL of DI water and magnetically agitated at 300 rpm at room temperature for 30min. Separately, 0.656g of 2-Methylimidazole was dissolved in 50ml of DI water. The $Zn(NO_3)_2 \cdot 6H_2O$ solution was then introduced to the 2-Methylimidazole solution, and the mixture was continuously stirred overnight on a hot plate. The precipitate so formed was washed and collected by centrifugation, dried in an oven at 80°C and then finely ground into powder. Finally, the finely powdered sample was subjected to calcination at 500°C for 6 hours to obtain MOF-derived ZnO.

2.4 Characterization

Powder X-Ray diffraction (XRD) was used to determine the phase composition of pure ZnO and MOF-derived ZnO with the X'Pert Pro PANalytical diffractometer equipped with Cu Kα radiation. The Field emission scanning electron microscopy (FESEM) was used alongside EDX spectroscopy to analyze its morphological characteristics, as well as its elemental constitution. The UV-visible spectra of the materials were taken on a Perkin Elmer Lambda-365 UV-Vis Spectrophotometer. The functional group and the chemical bond of the particles were determined by the Perkin Elmer FTIR Spectrum 2 IR spectrometer.

2.5 Photocatalytic activity test

Photodegradation experiment was conducted by using Malachite Green dye as the model pollutant and irradiated by UV-C light from an 8W mercury lamp. In a typical photocatalytic procedure, the catalyst was dispersed into the dye solution and subjected to ultrasonication. To achieve a state of adsorption-desorption equilibrium, the catalyst-loaded dye suspension was stirred in the dark for 1 hour and thereafter it was irradiated with the light source. Aliquots of the irradiated solution were then taken at regular interval of time and their absorbance was recorded with the help Ocean Optics HR 4000 UV-Vis Spectrophotometer. The photocatalytic efficiency of the synthesized samples was assessed based on percentage degradation, calculated using the following Eq. (1) [23].

$$\% \text{ of Degradation} = \frac{C_0 - C}{C_0} \times 100 = \frac{A_0 - A}{A_0} \times 100 \tag{1}$$

where C_0 represents the initial dye concentration, C represents the concentration after irradiation, A_0 denotes the initial absorbance, and A denotes the absorbance of the solution measured after irradiation.

3 Results and Discussion

3.1 Structural characterization

Fig. 1(a), 1(b) and 1(c) illustrate the XRD patterns of pure ZnO nanoparticles, pure MOF and MOF-derived ZnO nanoparticles, respectively. The diffracted patterns in Fig. 1(a) and 1(c) exhibit characteristic Bragg reflections corresponding to the crystallographic planes: (202), (004), (201), (112), (200), (103), (110), (102), (101), (002), and (100), along with their corresponding 2θ values. The peaks of the diffraction confirm the existence of hexagonal wurtzite phase of ZnO (ICSD card number: 01-075-0576). Scherrer's formula (Eq. (2)) was used to estimate the crystallite size, which was calculated to be 18 nm and 24 nm for pure ZnO and MOF-derived ZnO respectively.

$$g = \frac{k\lambda}{\beta \cos\theta} \tag{2}$$

where g denotes the crystallite size (nm), λ is the wavelength of the X-ray (nm), k is the shape factor or Scherrer constant (0.9), θ is the Bragg angle (radians), and β is the full width at half maximum of the diffraction peaks (radians) [24].

The XRD pattern of the synthesized MOF, as shown in Fig. 1(b), exhibits distinct diffraction peaks corresponding to the characteristic planes of its crystalline framework, confirming its successful formation [25].

The measured positions and intensities of the observed peaks are comparable with those of the MOF structures which crystallized in the hexagonal phase and is highly similar to the reference pattern indexed in the JCPDS card no. 00-062-1030, thus confirming the high purity and crystallinity of the phase in the obtained material [26–29].

The controlled growing environment of the MOF precursor, which facilitates uniform nucleation and growth of the crystal is the reason behind the slightly larger size of the MOF-derived ZnO [22]. The intense, sharp peaks suggest high levels of crystallinity, which facilitates rapid electron transport and slow down recombination and contribute to the high photocatalytic activity of MOF-derived ZnO in MG dye degradation [30].

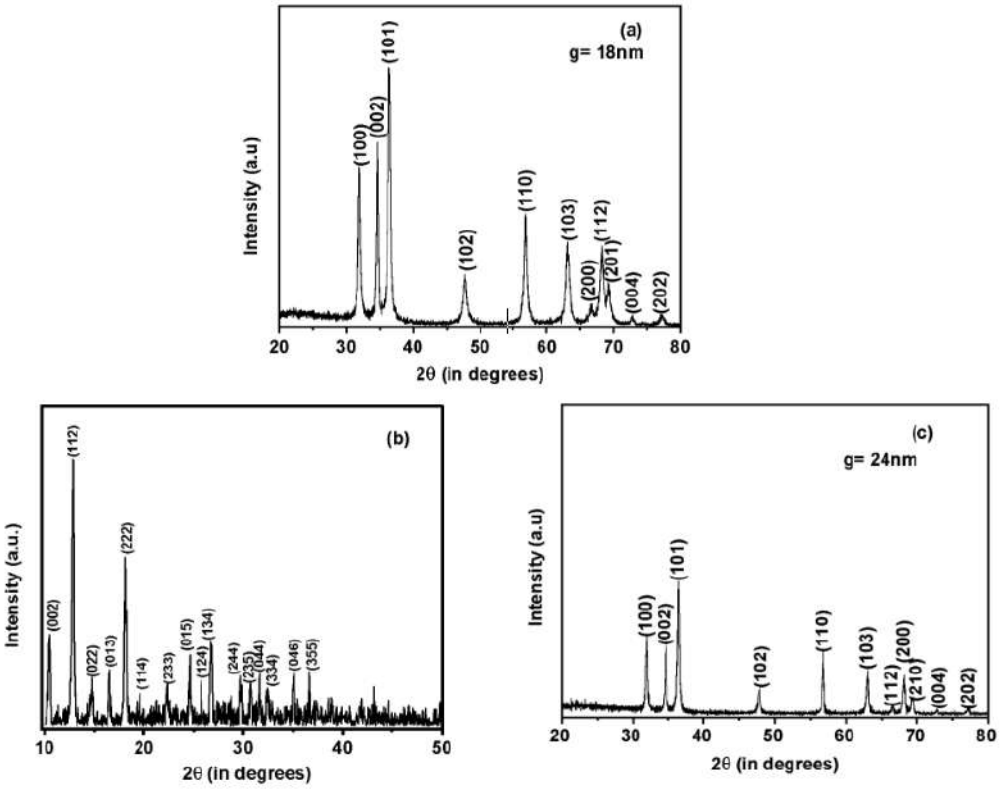

Figure 1: XRD patterns of the synthesized samples (a) pure ZnO, (b) ZIF-8 MOF, and (c) MOF-derived ZnO.

3.2 Morphological and compositional analysis

FESEM was used to study the surface morphology of the synthesized samples. As shown in Fig. 2(a), the pure ZnO nanoparticles exhibit a mixture of spherical and spindle-like structures. In contrast, Fig. 2(c) reveals that the MOF-derived ZnO crystals predominantly exhibit an agglomerated spherical morphology. The corresponding particle size distribution histograms, presented in Fig. 2(b) and 2(d), were fitted using a log-normal distribution function [31]:

$$f_d = \frac{1}{d\sigma\sqrt{2\pi}} \exp[\frac{(\ln d - \mu)^2}{2\sigma^2}], \tag{3}$$

where d is the particle diameter, σ is the standard deviation of $\ln d$, μ is the mean of $\ln d$.

Average particle size was estimated from the fitted parameters according to the standard expression for a log-normally distributed variable [32]:

$$d_{avg} = \exp[\frac{\mu + \sigma^2}{2}] \tag{4}$$

Using this relation, the average particle sizes of the pure ZnO and MOF-derived ZnO were estimated to be 175 nm and 92 nm, respectively. The significantly smaller and more uniform particle size of the MOF-derived sample highlights the structural templating of the MOF precursor, which promotes the formation of finer ZnO nanoparticles with enhanced surface area and improved physiochemical properties, including photocatalytic performance.

Fig. 3(a) and 3(b), respectively display the elemental composition of pure ZnO and MOF-derived ZnO. The presence of emission peaks corresponding to Zn and O atoms only are observed in the EDX spectra, with no additional peaks, which confirms the sample purity.

3.3 UV-Vis Absorption Spectroscopy

Fig. 4(a) and 4(b) depict the UV-Vis absorption results of pure ZnO and MOF-derived ZnO nanoparticles, respectively, with 367 nm and 373 nm as the absorption peaks. The optical band gap (Eg) was also estimated using the

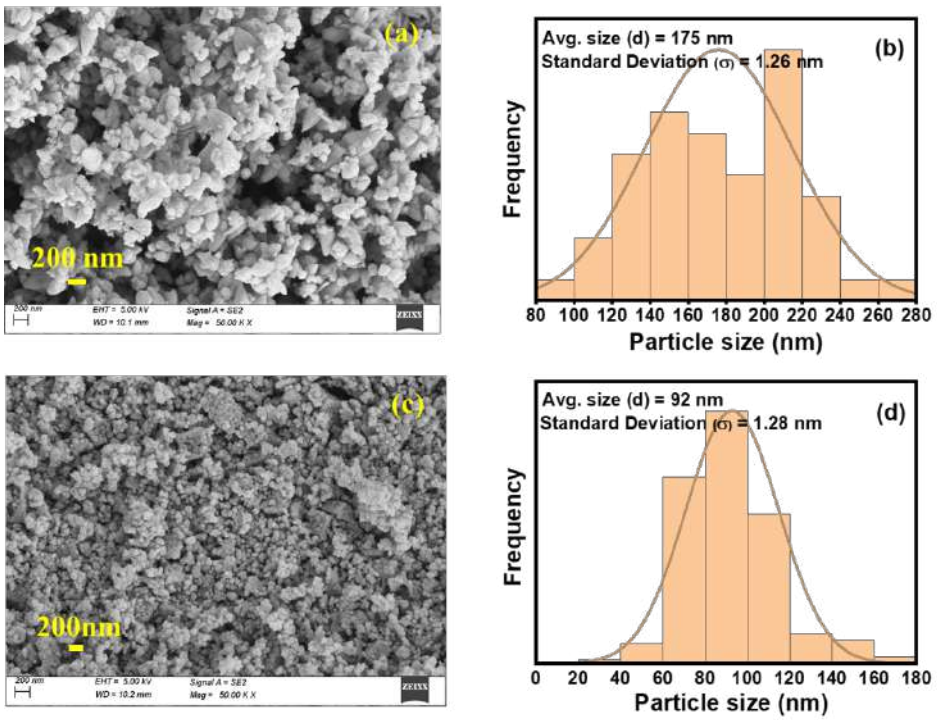

Figure 2: Surface morphology observed by FESEM and particle size distribution histograms of (a) FESEM image of pure ZnO and (b) particle size distribution of pure ZnO fitted with a log-normal distribution (c) FESEM image of MOF-derived ZnO (d) particle size distribution of MOF-derived ZnO fitted with a log-normal distribution.

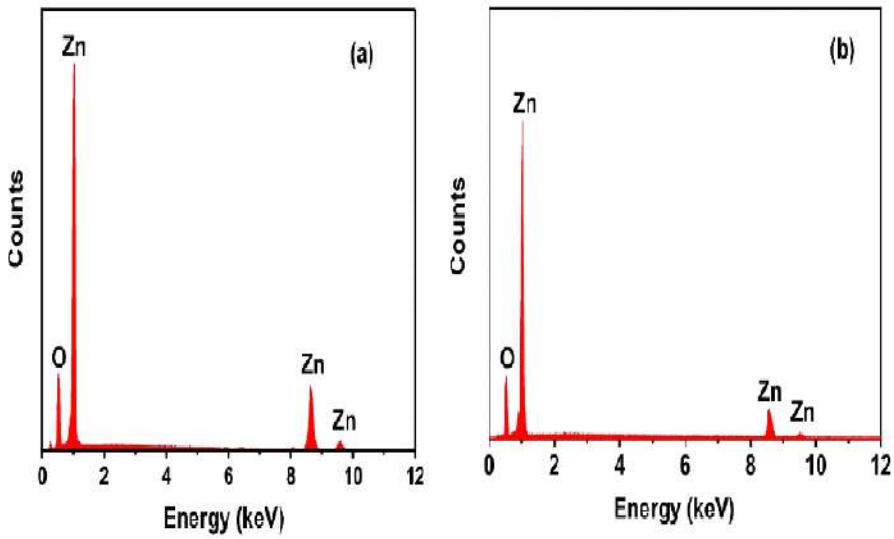

Figure 3: EDX spectra of the synthesized samples (a) pure ZnO and (b) MOF-derived ZnO.

following relation [33]:

$$E_g = \frac{hc}{\lambda} \tag{5}$$

where c represents the speed of light, h denotes Planck's constant, and λ corresponds to the wavelength of the respective absorption peak.

The band gap energy of pure ZnO and MOF-derived ZnO was determined to be 3.32 eV.

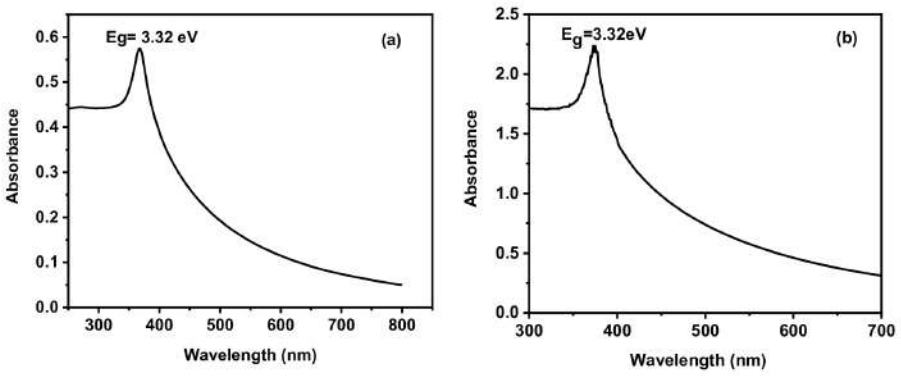

Figure 4: UV-vis absorption spectra of the synthesized samples (a) pure ZnO and (b) MOF-derived ZnO.

3.4 Fourier Transform Infrared (FTIR) Spectra

The Fourier transform infrared (FTIR) spectrum of pure ZnO and MOF-derived ZnO, are presented in Fig. 5(a) and 5(b), respectively. For pure ZnO, a prominent absorption band corresponding to the Zn–O stretching vibration is observed at 410 cm^{-1}. In the case of MOF-derived ZnO, this band is slightly shifted to 416 cm^{-1}, which may be attributed to lattice distortions, altered crystallite size, or structural modifications induced during the MOF-to-ZnO transformation [34].

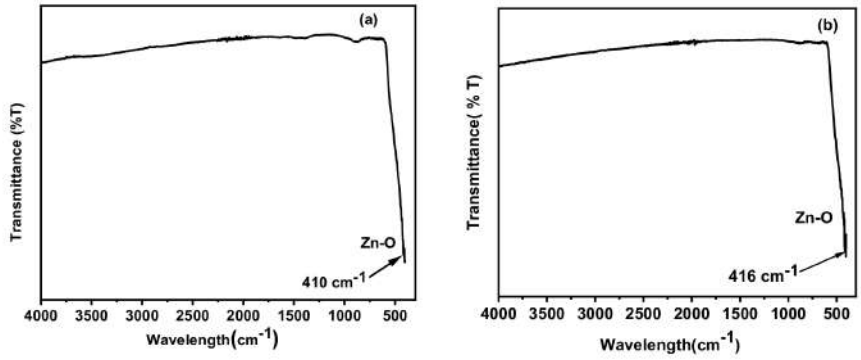

Figure 5: FTIR spectra of synthesized samples (a) pure ZnO and (b) MOF-derived ZnO.

3.5 Evaluation of the photocatalytic activity on MG dye

Fig. 6(a) and 6(b) show the photocatalytic degradation curves of pure ZnO and MOF-derived ZnO upon UV light irradiation. Pure ZnO achieves 76% degradation of MG under 3 hours of irradiation, whereas MOF-derived ZnO reaches 98% degradation in just 3 hours. This enhanced photocatalytic performance is ascribed to the MOF-derived architecture, which provides increased surface area and porosity, thereby facilitating more efficient dye degradation [22].

Kinetics of the photocatalytic reaction was studied by applying the Langmuir-Hinshelwood model, which reveals that the reaction followed the pseudo-first-order kinetics. This relationship is expressed as Eq. (4) [35]

$$\ln\frac{C_0}{C} = kt \tag{6}$$

where C_0 and C denote the initial and final concentration of dye prior to and following irradiation, respectively, k is the pseudo first order rate constant, t is the irradiation time. Table 1 indicates the values of the rate constants

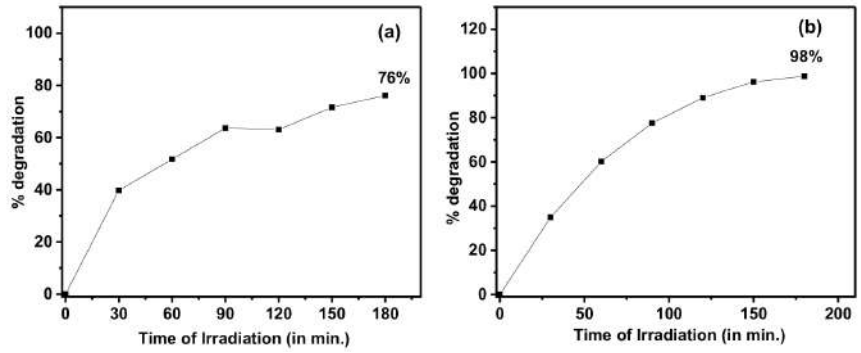

Figure 6: Photocatalytic degradation curves for (a) pure ZnO and (b) MOF-derived ZnO.

calculated. The two distinct linear areas in the kinetic plot may be explained as follows:

$$\text{Organic Dye} \rightarrow \text{Adsorption} \xrightarrow{k_1} \text{Intermediate Product} \xrightarrow{k_2} \text{Colourless Product}$$

Photocatalyst	**Rate constant,** k_1 **(**10^{-2} **per min)**	**Rate constant,** k_2 **(**10^{-2} **per min)**
MOF – derived ZnO	1.7	3.2
Pure ZnO	1.2	0.8

Table 1: Reaction rate constants calculated for the synthesized samples.

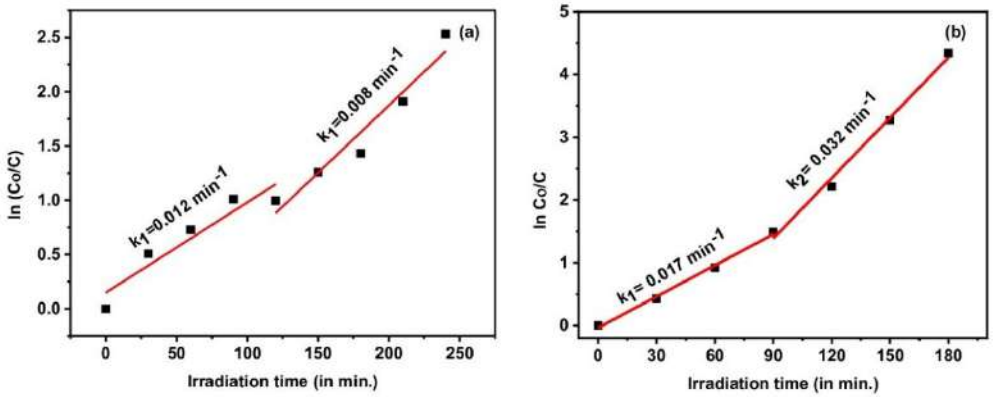

Figure 7: Plot of $\ln(C_0/C)$ vs. irradiation time for (a) pure ZnO and (b) MOF-derived ZnO.

4 Conclusions

In conclusion, pure ZnO nanoparticles and MOF-derived ZnO nanoparticles were prepared using chemical co-precipitation method and self-assembly technique, respectively. XRD analysis confirmed that both samples were in the hexagonal wurtzite structure. FESEM micrographs proves that pure ZnO was a composite of both spherical and spindle-like particles, but the MOF-derived ZnO was more likely to have the morphology of a sphere. The use of energy-dispersive X-ray (EDX) spectroscopy technique established that the samples only contained zinc and oxygen. The UV-visible absorption spectra were used to estimate the optical bandgap energies, which means that both samples can be applied in the UV region. The photocatalytic efficiency of MOF-derived ZnO was found to be better degrading 98% of MG dye under the UV light in 3 hours. These findings highlight the possibility of MOF-derived ZnO to be an efficient photocatalyst in eliminating organic pollutants.

References

[1] N. Nayak, S. Singha, J. P. Maity, P. P. Rath, T. Sahoo, and T. R. Sahoo, Journal of Materials Science: Materials in Electronics **35**, 310 (2024).

[2] R. Sarathi, L. Renuga Devi, N. L. Sheeba, E. Selva Esakki, and S. Meenakshi Sundar, Journal of Chemical Reviews **5**, 15 (2023).

[3] D. Sahoo, S. Tyagi, S. Agarwal, J. Shakya, N. Ali, W. J. Yoo, and B. Kaviraj, Langmuir **39**, 7109 (2023).

[4] P. Singh, B. Mohan, V. Madaan, R. Ranga, P. Kumari, S. Kumar, V. Bhankar, P. Kumar, and K. Kumar, Environmental Science and Pollution Research **29**, 69294 (2022).

[5] S. Meena, D. Vaya, and B. K. Das, Bulletin of Materials Science **39**, 1735 (2016).

[6] M. O. Chijioke-Okere, N. J. Okorocha, B. N. Anukam, and E. E. Oguzie, International Letters of Chemistry, Physics and Astronomy **81**, 18 (2019).

[7] T. Ahuja, U. Brighu, and K. Saxena, Journal of Water Process Engineering **53**, 103759 (2023).

[8] S. Chaudhari, A. Kularkar, S. Devi, and P. Nagababu, Journal of Physics and Chemistry of Solids **188**, 111929 (2024).

[9] A. M. Saad, M. R. Abukhadra, S. Abdel-Kader Ahmed, A. M. Elzanaty, A. H. Mady, M. A. Betiha, J.-J. Shim, and A. M. Rabie, Journal of Environmental Management **258**, 110043 (2020).

[10] W. S. Koe, J. W. Lee, W. C. Chong, Y. L. Pang, and L. C. Sim, Environmental Science and Pollution Research **27**, 2522 (2020).

[11] A. Balapure, J. Ray Dutta, and R. Ganesan, RSC Applied Interfaces **1**, 43 (2024).

[12] J. Kalita, L. Bharali, and S. S. Dhar, New J. Chem. **46**, 20182 (2022).

[13] S. N. Ahmed and W. Haider, Nanotechnology **29**, 342001 (2018).

[14] R. E. Adam, G. Pozina, M. Willander, and O. Nur, Photonics and Nanostructures - Fundamentals and Applications **32**, 11 (2018).

[15] R. Ullah and J. Dutta, Journal of Hazardous Materials **156**, 194 (2008).

[16] D. Dodoo-Arhin, T. Asiedu, B. Agyei-Tuffour, E. Nyankson, D. Obada, and J. Mwabora, Materials Today: Proceedings **38**, 809 (2021), 2020 International Symposium on Nanostructured and Advanced Materials.

[17] S. Kerli, M. Kavgacı, A. K. Soğuksu, and B. Avar, Brazilian Journal of Physics **52**, 22 (2021).

[18] N. Qutub, P. Singh, S. Sabir, S. Sagadevan, and W.-C. Oh, Scientific Reports **12**, 5759 (2022).

[19] Y. Wang, C. Hou, X. Lin, and H. Jiang, SN Applied Sciences **1**, 743 (2019).

[20] S. H. Ribut, C. A. Che Abdullah, M. Mustafa, M. Z. Mohd Yusoff, and S. N. Ahmad Azman, Materials Research Express **6**, 025016 (2018).

[21] S. Sheikhi, M. Aliannezhadi, and F. Shariatmadar Tehrani, European Physical Journal Plus **137**, 60 (2022).

[22] P. Abisha, J. C.G., and S. Sonia, Current Applied Physics **60**, 79 (2024).

[23] L. A. Chanu, K. J. Singh, and K. N. Devi, Integrated Ferroelectrics **204**, 90 (2020).

[24] L. Anju Chanu, W. Joychandra Singh, K. Jugeshwar Singh, and K. Nomita Devi, Results in Physics **12**, 1230 (2019).

[25] Y. Jing, J. Wang, B. Yu, J. Lun, Y. Cheng, B. Xiong, Q. Lei, Y. Yang, L. Chen, and M. Zhao, RSC Adv. **7**, 42030 (2017).

[26] Y. Sun, H. Zhang, Y. Lv, S. An, and R. Wang, RSC Adv. **14**, 17498 (2024).

[27] J. Chen, Y. Yang, S. Yu, Y. Zhang, J. Hou, N. Yu, and B. Fang, Nanomaterials **13** (2023).

[28] I. Rabani, S. A. Patil, M. S. Tahir, F. Afzal, J.-W. Lee, H. Im, Y.-S. Seo, and N. K. Shrestha, Nanomaterials **13** (2023).

[29] K. Zhou, B. Mousavi, Z. Luo, S. Phatanasri, S. Chaemchuen, and F. Verpoort, J. Mater. Chem. A **5**, 952 (2017).

[30] Q. Wang and D. Astruc, Chemical Reviews **120**, 1438 (2020).

[31] S. K. Paswan, S. Kumari, M. Kar, A. Singh, H. Pathak, J. Borah, and L. Kumar, Journal of Physics and Chemistry of Solids **151**, 109928 (2021).

[32] M. Molaei, M. Abdollahi, A. M. Zardkhoshoui, and S. S. H. Davarani, Journal of Energy Storage **85**, 111079 (2024).

[33] L. A. Chanu, K. J. Singh, and K. N. Devi, AIP Conference Proceedings **2265**, 030052 (2020).

[34] C. Berthomieu and R. Hienerwadel, Photosynthesis Research **101**, 157 (2009).

[35] L. Anju Chanu, K. Jugeshwar Singh, and K. Nomita Devi, Materials Today: Proceedings **65**, 2865 (2022).

PANE
P. J. Phys. 02 (01), 042 (April 2026) PANE Journal of Physics

ETCHING CHARACTERISTICS OF LR-115 TYPE II FILMS USING PERCENTAGE–TRACK DENSITY

Yubaraj Sharma[1], Budmiki Talang[2], Deveshwori Maibam[3], and Aibanjop Pyngrope[*4]

[1]*Department of Physics, Don Bosco College, Tura, Meghalaya, India*
[2]*Department of Physics, Assam Don Bosco University, Sonapur, Assam, India*
[3]*Don Bosco College of Teacher Education, Tura, Meghalaya, India*
[4]*Department of Physics, Captain Williamson Sangma State University, Meghalaya, India*

[*]Corresponding Author: ibanbiba@gmail.com

(Received 26 September 2025; revised 21 November 2025; accepted 11 December 2025; published 6 April 2026)

Abstract: We investigate the etching characteristics of environment-exposed LR-115 film (cellulose nitrate) solid state nuclear track detector (SSNTD), which is commonly used for the detection of terrestrial ionizing radiation, particularly in indoor and soil gas environments. The percentage-track density in exposed LR-115 detectors is used as a proxy for bulk etching and examined under different etching conditions. Expectedly, results reveal that the track density increases with temperatures and normality. Linear regression coefficients as well as multiple linear regression coefficients are estimated.

Keywords: SSNTD; Etching; LR-115, Regression

PACS: 07.57.Kp, 29.40.-n; 87.53.Bn; 87.53.-j

1 Introduction

Solid State Nuclear Track Detectors (SSNTDs) are widely used for detecting and measuring properties of fast-moving charged particles, including alpha particles, fission fragments, and heavy ions, owing to their remarkable sensitivity, durability, and affordability [1]. Among SSNTDs, polymeric detectors stand out due to their sensitivity, and among polymeric detectors, the cellulose nitrate polymer film, commonly known as LR-115 (type II), is the most favoured for monitoring environmental radioactivity, especially in studies on radon and thoron concentration [2–5]. These detectors capture ionizing radiation by creating latent tracks, which can be uncovered via an appropriate chemical etching process [1].

The etching process is vital for visualizing and analysing these tracks. Factors like etching time, temperature, and the concentration of the etchant greatly influence track geometry, etch rate, and consequently, track density measurements [1, 6, 7]. Therefore, a comprehensive understanding of etching characteristics is crucial for precise particle identification as well as dosimetric calculations. Although morphology of etch pits conveys details about the energy and charge of the incident particle, it is the simpler quantity — track density — that is useful for measurement of environmental radioactivity [8–10]. Several researchers have focused on optimizing etching conditions to enhance the resolution and accuracy of the LR-115 detector response. For instance, Durrani and Bull [1] provided foundational insights into track formation and etching mechanisms, while later studies have explored variations in chemical etchants and etching protocols to improve track contrast and reduce background noise [7, 11, 12]. These advancements also warrant corresponding investigations to corroborate the etching behaviour of LR-115 films under different controlled exposures and chemical conditions.

The present study focuses on examining the etching properties of exposed LR-115 film, particularly how various etching parameters affect track revelation. It is usually the bulk etch rate of detectors that is measured against etching parameters, but during use in the field, it is the track density that is directly measured and hence its adoption in the present study. Such investigations are essential for enhancing the accuracy of SSNTD-derived measurements, particularly in situations involving low-level radiation monitoring.

2 Materials and method

In the present study, LR-115 type II SSNTD manufactured by DOSIRAD, France, with an active layer of $12\,\mu\mathrm{m}$ and polyester base of thickness $100\,\mu\mathrm{m}$ was used. The water-bath used had a thermostat with control of $\pm 2^{\circ}\mathrm{C}$. A typical microscope (Labomed) with magnification $40\times$ was used for counting and measurement of track properties. For etching, laboratory-grade NaOH was used. For radiation source, we used the ubiquitous environmental radioactivity — the detectors were hung from threads for a period of 90 days, similar to the method of bare-mode exposure for the measurement of indoor radon concentration [13, 14].

The primary objective of the study is to determine etching characteristics in terms of track densities observed in the etched LR-115 film by varying etching duration, etchant concentration and etching temperature. Two etchant concentrations were identified for the experiment, viz., $2\mathrm{N}$ and $2.5\mathrm{N}$ of NaOH; three temperature values were identified, viz., $40^{\circ}\mathrm{C}$, $50^{\circ}\mathrm{C}$ and $60^{\circ}\mathrm{C}$, while the track densities were measured at four etching durations, viz., 60, 70, 80 and 90 minutes. These values of the parameters were chosen keeping in mind the upper limits of standard procedure of etching LR-115 films, which are $2.5\mathrm{N}$, $60^{\circ}\mathrm{C}$ and 90 minutes [10, 15, 16]. The raw values of track density are not conducive for direct calculation as they are highly dependent on the exposure duration and the concentration of alpha-emitting radon atoms in air. Therefore, with the assumed standard values of etching parameters, we represent track density in percentage terms with respect to the track density obtained for 90 minutes of etching at $60^{\circ}\mathrm{C}$ and $2.5\mathrm{N}$ etchant solution.

The exposed detectors were selected randomly and placed into six groups labelled with a specific normality value and temperature. Successive etching was carried out, keeping step with the time interval chosen for the study. The etching process is carried out by placing a conical beaker with the etchant of a specific concentration in the thermostatically controlled water bath at specific temperature. When the temperature of the etching solution reaches equilibrium with the temperature of the water bath, the LR-115 films are introduced in the beaker so as to completely submerge them in the etchant. At specified intervals, the LR-115 films are extracted from the water bath and dried. The track densities in the etched films are then determined by manually counting the tracks with the help of the microscope.

Linear regression as well as multiple linear regression were carried out to estimate a linear relationship between the response (or dependent) variable, viz., the track density, and three explanatory (or independent) variables — etchant normality, etchant temperature and etching time. The linear regression was done using the `scikit-learn` package [17], while the multiple regression was done using the R programming language [18].

A simple linear regression consists of a single response as well as a single explanatory variable and entails the estimation of the coefficients of the linear equation (usually called the prediction equation) of the form [19],

$$y = \beta_0 + \beta_1 x + \varepsilon \tag{1}$$

where $\hat{y}$ is the predicted value for a given value of the explanatory variable x (the cap over a variable indicates predicted or estimated value); $\hat{\beta}_0$ and $\hat{\beta}_1$ are respectively the intercept and slope of the linear relationship, and ε is the error (the unpredictable part of the data).

Multiple linear regression extends linear regression to accommodate multiple explanatory variables $(x_1, x_2, \cdots, x_k)$ for a single response variable (y) and is mathematically expressed as [19],

$$y = \beta_0 + \beta_1 x_1 + \beta_2 x_2 + \cdots + \beta_k x_k + \varepsilon. \tag{2}$$

The other symbols in the above equation have meanings similar to those used in equation (1).

We do realise that the results of this study have limited generality due to the limited range of variables considered; however, this study can pave the way for more detailed experimental setup and analysis.

3 Results and Discussions

The obtained experimental values of percentage track density are plotted as a function of etching time for different values of etching temperature in the two subplots given in figure 1. Each subplot in the figure represents data corresponding to a specific etchant normality — $2\mathrm{N}$ and $2.5\mathrm{N}$. We have kept the y-axis of both the subplots the same to facilitate comparison at the cost of some detail. Expectedly, track densities increase with time as well as temperature. It is also seen that the general trend indicates higher slopes for higher temperatures. Track densities are also higher for higher normality for a given etching time, thus indicating throughout a positive correlation between track density and all three explanatory variables.

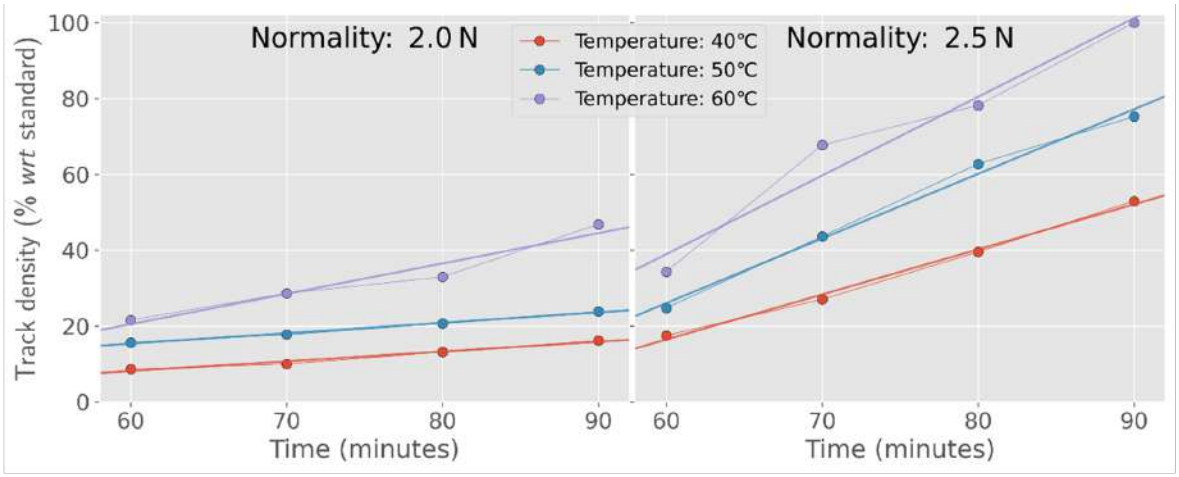

Figure 1: Track density in LR-115 as a function of etching time for various etching temperatures for two different normalities of etchant concentration. Solid lines of corresponding colour indicate linear-fit line.

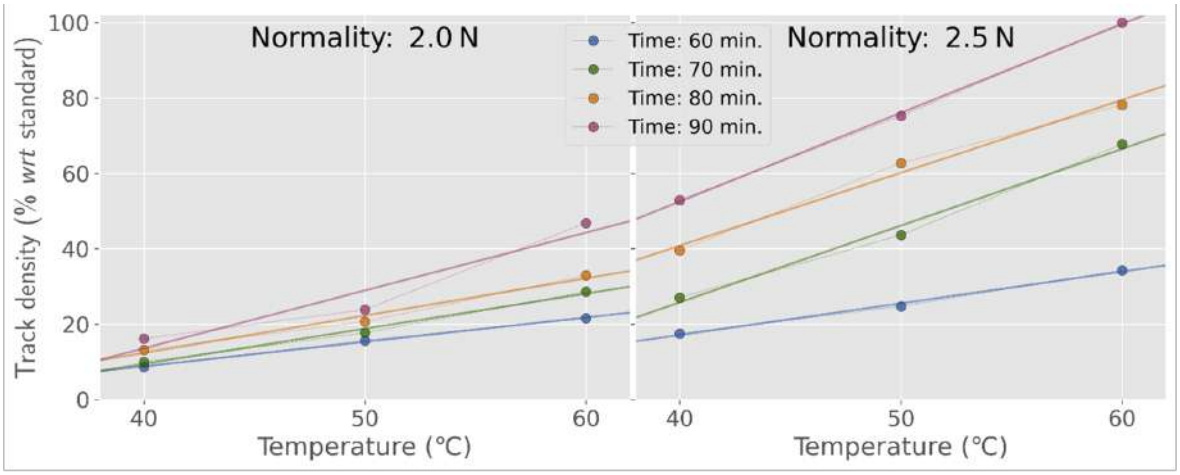

Figure 2: Track density in LR-115 as a function of etching temperature for different etching times for two different normalities of etchant concentration. Solid lines of corresponding colour indicate linear-fit line.

To highlight the effect of etching temperature, we have replotted the data in figure 2, but with the temperature on the x-axis. This is to visually show the effect of temperature on track density at various etching times.

To quantify the trend across the various variables, we have provided the values of linear regression in table 1, along with corresponding goodness-of-fit parameters.

Table 2 provides the value of coefficients for the various explanatory variables obtained from a multiple regression exercise carried out on the experimental data. The Sum of Squared Errors (SSE) for the regression is found to be 1779.188 and the multiple R^2 value is 0.8719. We can see that the R^2 value of the multiple regression is noticeably lesser than the R^2 value of direct linear regression (table 1), indicating that the generalization of the fit to multiple variables reduces the goodness-of-fit observed in individual regressions.

Based on the coefficients given in table 2, the percentage track density (ρ) as a function of time of etching in minutes (t), the temperature in $^\circ$C (θ) and the normality of etchant (N) can be written as [1] (c.f., equation 2),

$$\rho = -250.38 + 1.05\,t + 1.41\,\theta + 61.29\,N. \tag{3}$$

Based on the value of coefficients obtained, we find that, in terms of numerical value (with the specific units used here), the normality has the highest impact (as it has the highest value of slope, thus providing a large increase in the value of dependent variable for a specified increase in its value), followed by temperature and then

[1] Rounded to two decimal digits

Normality	Time	Temperature	Slope	Intercept	SSE	r^2
2	60	**	0.65	-17.1	0.22	0.997
2	70	**	0.93	-27.8	1.69	0.990
2	80	**	0.99	-27.2	3.80	0.981
2	90	**	1.53	-47.8	38.64	0.924
2.5	60	**	0.84	-16.5	0.86	0.994
2.5	70	**	2.03	-55.6	9.38	0.989
2.5	80	**	1.93	-36.4	9.95	0.987
2.5	90	**	2.35	-41.6	1.04	0.999
2	*	$40°\mathrm{C}$	0.26	-7.3	0.84	0.975
2	*	$50°\mathrm{C}$	0.27	-1.1	0.35	0.991
2	*	$60°\mathrm{C}$	0.80	-27.5	19.15	0.944
2.5	*	$40°\mathrm{C}$	1.19	-54.9	3.94	0.994
2.5	*	$50°\mathrm{C}$	1.70	-76.2	12.45	0.992
2.5	*	$60°\mathrm{C}$	2.07	-85.6	92.47	0.959

* indicates all values of etching time variable, viz., 60, 70, 80 and 90 minutes.

** indicates all values of etching temperature variable, viz., $40°\mathrm{C}$, $50°\mathrm{C}$ and $60°\mathrm{C}$.

Table 1: Coefficients of linear regression between normality–etching time and normality–temperature along with goodness-of-fit statistics.

Coefficients	Estimate	Std. Error	p-value
Constant term (or intercept)	-250.3835	24.6930	2.50×10^{-9}
Time (minutes)	1.05	0.1722	5.85×10^{-6}
Temperature ($°\mathrm{C}$)	1.4077	0.2358	7.74×10^{-6}
Normality	61.2879	7.7011	1.260×10^{-7}

Table 2: Coefficients of multiple linear regression for the response variable of track density and the three etching parameters.

the time of etching. For example, equation (3) predicts that an increase in normality by ΔN would produce about $(60\,\Delta N)\%$ more tracks compared to a $\Delta\theta$ increase in temperature.

It is hoped that the calculations and regression values provided here might prove useful in numerical simulation exercises and facilitate comparison even under different etching conditions.

Conclusions

Experimental values of percentage track densities for the solid-state nuclear track detector LR-115 type II for various etching conditions are presented. The observed trends are consistent with those reported in literature [1, 8]. Linear and multiple linear regression coefficient values are estimated.

References

[1] S. A. Durrani and R. K. Bull, *Solid State Nuclear Track Detection: Principles, Methods and Applications*, International Series in Natural Philosophy, Vol. 111 (Pergamon Press, Oxford, 1987).

[2] A. Pyngrope, P. Sangma, and R. K. Kakati, Journal of Physics: Conference Series **2919**, 012039 (2024).

[3] L. A. S. Pereira and C. A. T. Sáenz, Physics **7**, 56 (2025).

[4] P. Pereyra, C. J. Guevara-Pillaca, R. Liza, B. Pérez, J. Rojas, L. Vilcapoma L., S. Gonzales, L. Sajo-Bohus, M. E. López-Herrera, and D. Palacios Fernández, Atmosphere **14** (2023).

[5] A. S. Hussein, Radiation Environment and Medicine **10**, 26 (2021).

[6] S. Durrani and P. Green, Nuclear Tracks and Radiation Measurements (1982) **8**, 21 (1984).

[7] M. Caresana, F. Campi, and M. Ferrarini, Radiation Protection Dosimetry **113**, 354 (2005).

[8] D. Nikezic, F. Ng, and K. Yu, Applied Radiation and Isotopes **61**, 1431 (2004).

[9] V. Mehta, C. Kapil, D. Shikha, and S. Kanse, Environmental Monitoring and Assessment **196**, 128 (2024).

[10] K. Eappen and Y. Mayya, Radiation Measurements **38**, 5 (2004).

[11] D. Palacios, L. Sajo-Bohus, H. Barros, E. Greaves, and F. Palacios, Revista Mexicana de Física **56**, 22 (2010).

[12] M. D. Salim, N. F. Kadhim, and A. A. Ridha, AIP Conference Proceedings **2290**, 030039 (2020).

[13] M. S. Khan, Journal of Nuclear and Radiation Sciences **1**, 19 (2022).

[14] D. Maibam, Y. Sharma, A. K. Dewsaw, A. Kenye, D. Walia, and A. Saxena, Journal of Applied and Fundamental Sciences **1**, 130 (2015).

[15] J. Virk and H. S. Virk, Research Reviews: A Journal of Toxicology **11**, 7 (2021).

[16] M. Prasad, M. Rawat, A. Dangwal, M. Yadav, G. S. Gusain, R. Mishra, and R. C. Ramola, Radiation Protection Dosimetry **167**, 102 (2015).

[17] F. Pedregosa, G. Varoquaux, A. Gramfort, V. Michel, B. Thirion, O. Grisel, M. Blondel, P. Prettenhofer, R. Weiss, V. Dubourg, J. Vanderplas, A. Passos, D. Cournapeau, M. Brucher, M. Perrot, and Édouard Duchesnay, Journal of Machine Learning Research **12**, 2825 (2011).

[18] R Core Team, *R: A Language and Environment for Statistical Computing*, R Foundation for Statistical Computing, Vienna, Austria (2025).

[19] L. Ott and M. Longnecker, *An Introduction to Statistical Methods and Data Analysis*, 7th ed. (Cengage Learning, 2016).

PANE

PANE Journal of Physics P. J. Phys. 02 (01), 047 (April 2026)

EXPLORING PATTERNS IN NUCLEAR BINDING ENERGY: ISOTOPIC, ISOTONIC AND ISOBARIC VARIATIONS

Yubaraj Sharma*[1]

[1]*Department of Physics, Don Bosco College, Tura, Meghalaya, India*

*Corresponding Author: yubaraj.physics@donboscocollege.ac.in

(Received 22 September 2025; revised 12 December 2025; accepted 28 December 2025; published 6 April 2026)

Abstract: We explore patterns in the nuclear binding energy data and seek their explanation in the Semi-Empirical Mass Formula (SEMF). The variations in the binding energy across isotopic, isotonic and isobaric sequences is analysed via standard deviation; the result shows a general decreasing trend, with the steepest decline for isotopic sequence and the gentlest decline for isobaric sequence. We have also analysed the correlation between the number of nuclides and the standard deviation. Transformation of the data into a time-series by arranging it in specific order in terms of the associated proton, neutron and atomic mass numbers reveal interesting patterns. Differencing of the generated time-series is found to have similarities and strong correlation with nucleon separation energies.

Keywords: Binding Energy per Nucleon; Isobars; Isotopes; Isotones; time-series

PACS: 21.10.-k, 21.10.Dr, 29.85.-c

1 Introduction

Nature and consequently real-world data are unruly, far from the elegant mathematical portraits drawn on university blackboards. The nuclear binding energy (BE) data may debatably be a good example of this familiar observation, and the simple and elegant formula used to model this data, called the Semi-Empirical Mass Formula (SEMF), although impressive, has limitations. Currently, there exists BE data of more than 3500 nuclides [1, 2], although not huge by the "big data" standards of today, still substantial enough to permit data and statistical analysis attempted in the current article.

The chronological journey of the nuclear binding energy concept starts arguably with the laying of the foundations of atomic theory by John Dalton. Observations at the time revealed that atomic masses were very close to whole numbers [1], but small deviations were also noticed, initially attributed to lack of experimental precision [3]. After the discovery of the atomic nucleus by Rutherford, it became abundantly clear that most of the mass of the atom was concentrated in the very small region of the nucleus [4]. With more precise measurements, particularly using high-precision mass-spectrographs, the "mass defect" or the deviation from whole numbers became undeniable [5]. Explanations were provided for this apparent deviation, but were not entirely satisfactory, as the structure of the nucleus was unclear at that time [6, 7], which only settled with the discovery of the neutron [8]. Bethe and Backer [9] clearly indicated the direct correspondence between the mass defect and the binding energy and even calculated the conversion factor from atomic mass units to MeV as $931.05 \pm 0.15\ \mathrm{MeV}$[2]. They redefined packing fraction as the ratio of the mass defect to the mass number[3] and formulated what is now known as the Semi-Empirical Mass Formula (SEMF) based on an earlier work by Weizsäcker[4].

Since the current state of knowledge of the nuclear structure places only protons and neutrons as constituents of the nucleus, it is obvious that the identity of a nuclide and therefore its binding energy is tied to the number of

[1]For example, see Prout's hypothesis or Aston's whole number rule.

[2]The notation used in the original publication was MV.

[3]This is slightly different from the definition of Aston [6], who had an additional factor of 10,000.

[4]Some literature cite this as the Bethe–Weizsäcker formula, crediting Weizsäcker also for the discovery, but the unfamiliarity of the author with the language of the original article [10] has prevented further comments.

these "elementary" constituents of the nucleus. It is, however, customary to set aside the neutron number (N) and use the proton number [5] (Z) and the mass number (A) to represent a nuclide. Consequently, in this representation, the binding energy $\mathrm{BE}(A, Z)$ of a nuclide is defined as a function of the mass number A and proton number Z with the defining equation [4, 11], given by

$$\mathrm{BE}(A, Z) = Zm_p + (A - Z)m_n - M(A, Z) \tag{1}$$

where m_p, m_n and $M(A, Z)$ represent the mass of a free proton, a free neutron and the actual mass of the nuclide respectively. All masses are expressed in energy units (usually MeV or keV), or they can be converted to MeV units from mass units (amu) using the more recent conversion factor from the CODATA 2022 [12] values:

$$931.49410372 \ \frac{\mathrm{MeV}}{\mathrm{amu}}.$$

The SEMF is given by [11, 13, 14],

$$\mathrm{BE}(A, Z) = a_v A - a_s A^{2/3} - a_c \frac{Z^2}{A^{1/3}} - a_{as} \frac{(A - 2Z)^2}{A} + \delta \tag{2}$$

where a_v, a_s, a_c and a_{as} are constant coefficients of the volume term, the surface term, the Coulomb term, and the asymmetry term respectively, while the pairing term δ has two general formulations with $A^{-3/4}$ or $A^{-1/2}$; the sign of the associated constant depends on proton–neutron pairing. The first three terms of SEMF correspond to an aspect of the liquid drop model of the nucleus, while the other two are quantum mechanical corrections; however, all the coefficients are derived empirically from data. These five coefficients are updated regularly as more experimental data becomes available, still, differences [6] persist [13, 15, 16]. These differences between the SEMF predictions and the experimental results, though small, have been the cause of some investigation [17, 18]. The reason for the nomenclature "Semi-Empirical Mass Formula" is historical, as the formula was used to determine the mass of nuclides [7]. However, to facilitate comparison between different nuclides, it is conventional to use the ratio of BE to the mass number (A), i.e., the binding energyper nucleon; we will hereafter use the shorter notation BE/A for binding energy per nucleon.

In the present paper, we explore patterns in the BE data made evident by data analysis techniques and seek explanations from the SEMF. Time-series analysis [19, 20] has a unique set of tools to extract patterns from data. While it is far more prevalent in the fields of finance and meteorology, it has had some applications in physics [21, 22]. Our approach is marginally different from traditional usage — the nuclear binding energy requires two independent variables, usually A and Z (see equations (1) and (2)). We flattened these two dimensions into a single dimension by ordering/sorting one variable followed by the other variable. This allows us to apply traditional methods of time-series analysis to the transformed data.

2 Computational aspect

To carry out the calculations and visualizations, two updated data sources were identified: the AME2020 [1, 23] and NuDat3 [2]; since NuDat3 also sources most of its data from AME2020, we opted for the more user-friendly NuDat3 dataset. For computation, we used the open-source Python programming language, with the `Pandas` and `SciPy` libraries/packages for most of the data analysis tasks, and the `matplotlib` package for drawing graphs [24–27].

To calculate [8] the theoretical values from the semi-empirical mass formula, we have used the coefficients and consequently the formula used by Benzaid *et al.* [13]; note that these authors have used Z^2 instead of the theoretically more palatable $Z(Z - 1)$ for the Coulomb term. Minor data cleaning was carried out before actual analysis, viz., removal of zero and negative BE values.

Primarily, we have a dependent variable (BE/A) and a set of three variables $(Z,\ N,\ A)$, only two of which are independent due to the relation/definition $A = Z + N$. To make it shorter and easier to refer to them, we shall call this collection of three variables the 'nuktriads' [9]. Each set of (BE/A) values with a common nuktriad value

[5] The number of protons in a nucleus is generally called atomic number, but we use proton number in consonance with the term neutron number

[6] See LDM disparity graph (defined later in the article) in Figs. 4-9 for an indication of the discrepancy

[7] Substituting equation 1 in equation 2 to get the formula for mass

[8] NuDat3 also provides their own SEMF values, however, we choose to calculate values directly

[9] Short for nuclear-triads (collection of three nuclear variables)

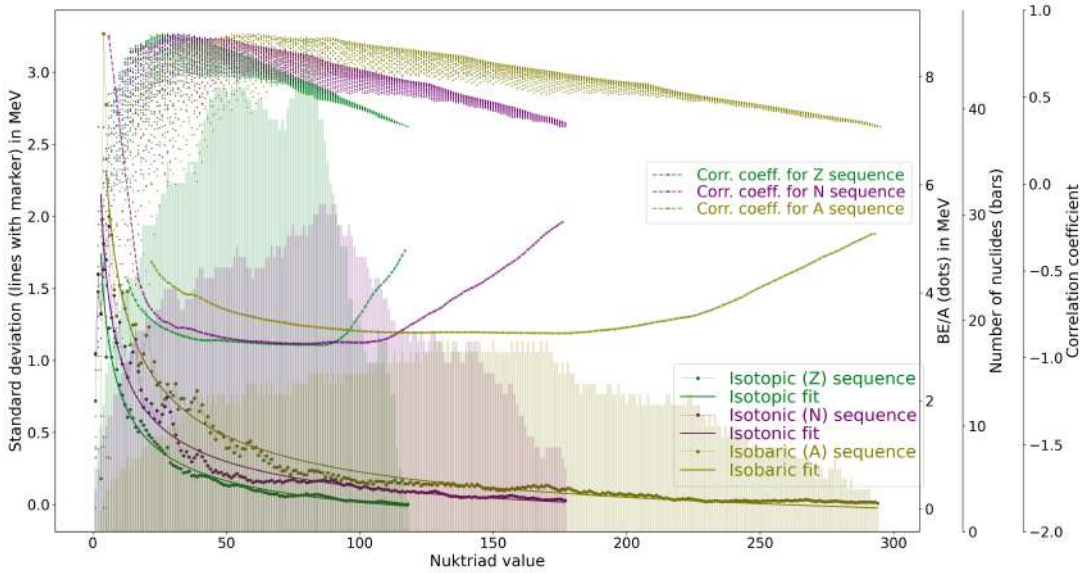

Figure 1: Plot of standard deviation of BE/A variation across isobaric, isotopic and isotonic sequences along with regression fit. Other plots include: Scatter-plot of actual BE/A; bar-graph of number of nuclides for each nuktriad value; correlation between and number of nuclides in the corresponding sequence. All plots have common x-axis.

will be called a sequence. Thus, an isotopic sequence is the set of nuclides with the same value of Z, an isotonic sequence is the set of nuclides with the same N value, and an isobaric sequence is the set of nuclides with the same A value.

3 Results and Discussion

We first look at the variations in the binding energy data within the isotopic, isotonic and isobaric sequences, quantified using the standard deviation (σ) as a measure; these are plotted in Fig. 1. We have used the sample standard deviation, defined as [28]:

$$\sigma = \sqrt{\frac{1}{N-1}\sum_{i=1}^{N}(x_i - \bar{x})^2} \tag{3}$$

where x_i represents the i^{th} value of the variable x having N data points, and $\bar{x}$ is its mean value. This basic definition is specified here for easy reference and reproducibility.

To make optimum use of space and to substantiate the relationships between different groupings, we have included multiple graphs (five sets) in Fig. 1. The common x-axis in the figure represents the value of the nuktriad variables — for example, in the figure of (BE/A) and other associated data plotted against Z, the x-axis represents the corresponding Z values. Similarly, when the same set of data is plotted against N, the x-axis represents the corresponding N values and so on. The colours in the figure are matched to corresponding groupings (one specific colour for a specific nuktriad variable). The primary data of our interest are the standard deviations, for which the y-scale is given on the left side of the graph. To corroborate the nature of the standard deviation curves obtained, we have included scatter plots of the (BE/A), arranged as per the three nuktriad sequences (y-scale attached to the right side of the graph).

We have also included bar graphs showing the number of nuclides within each nuktriad sequence. We observe that these bar graphs expectedly show broadly a Gaussian/bell-shaped pattern. This is expected because at lower values of the nuktriad variables there are not many stable combinations possible, while nuclides with high nuktriad values have fewer reported data due to their unstable nature and experimental difficulties.

Another aspect that we have packed into the figure is the Pearson correlation coefficient. This statistic (r) gives us a measure of the linear association between two time-series; it is given by [28]:

$$r = \frac{\sum(x_i - \bar{x})(y_i - \bar{y})}{\sqrt{\sum(x_i - \bar{x})^2 \sum(y_i - \bar{y})^2}} \tag{4}$$

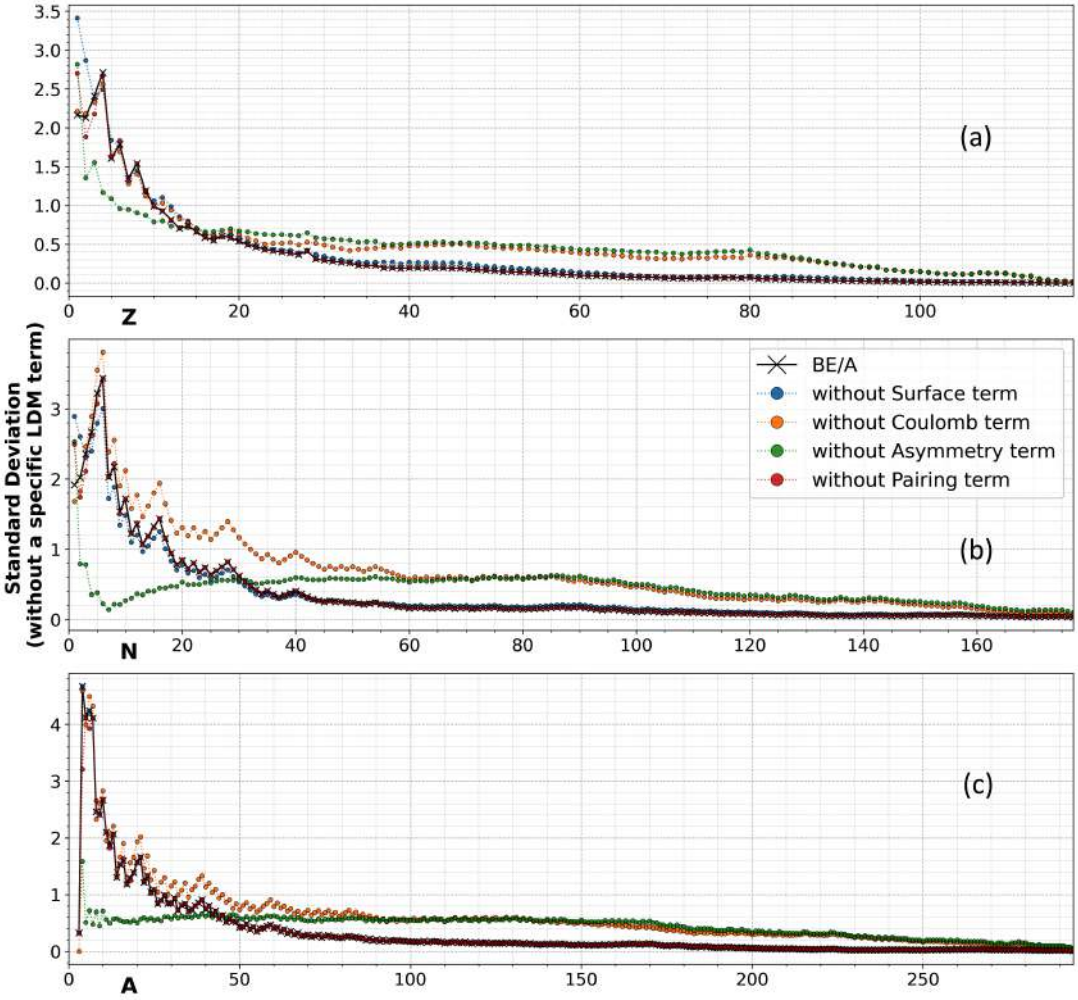

Figure 2: Standard deviation calculated from SEMF with only the nuclides present in the used dataset; the curve with black line contains all terms, other curves have one specific term of the SEMF excluded from the calculation. The x-axis label in three subplots represents the nuktriad sequence associated with the calculated standard deviation.

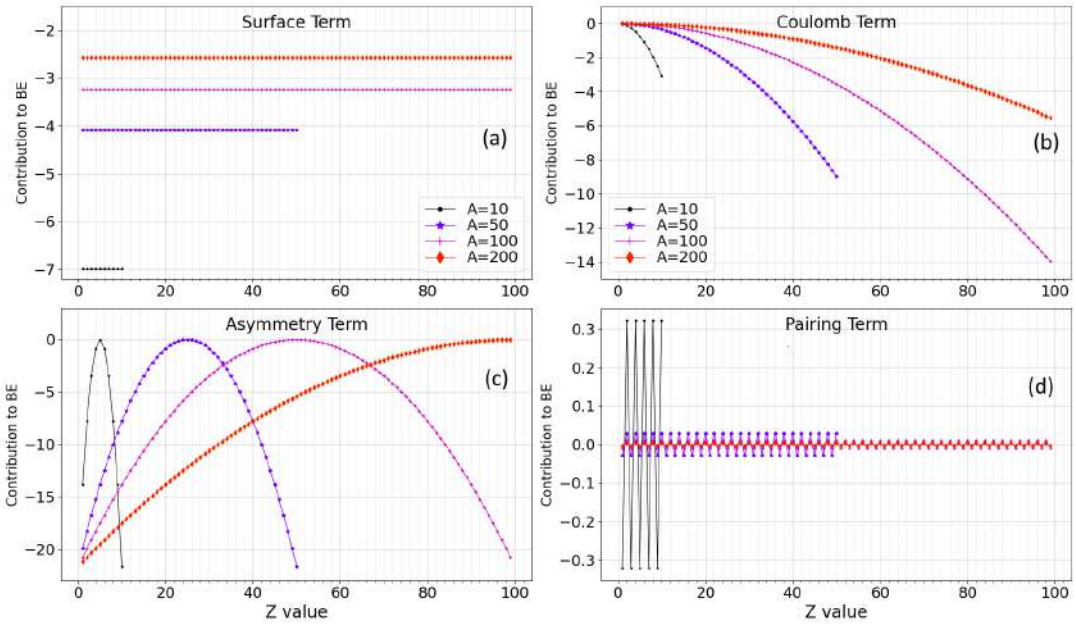

Figure 3: Variation of each term of the semi-empirical mass formula with values (range: 0 to 100) for four specific values of the atomic mass . Volume term is not included as it is a constant.

where x_i and y_i represent the i^{th} value of two correlated variables x and y respectively; $\bar{x}$ and $\bar{y}$ are the mean values of the respective variables.

The correlation plots given in Fig. 1 represent the coefficients of the Pearson correlation between standard deviation values and the number of nuclides; each point (say at x-axis or nuktriad value n) of the graph represents the correlation between the two variables from the beginning, i.e., nuktriad value 1, of the dataset up to nuktriad value n. Only points with statistically significant correlations, with p-value < 0.05, are plotted. We find that these curves broadly exhibit a U shape. This shape can broadly be explained as follows. The first part of a bell curve, where it is increasing, correlates negatively with the decreasing standard deviation curve; the other part of the bell curve (beyond the peak), where it is also decreasing, gives positive correlation — cumulatively and in conjunction with finer variations, they produce the U curve.

It is not straightforward to find a simple explanation from SEMF for the decreasing trend of the standard deviation (σ) in all the three nuktriad sequences. We employ the graphical route for explanation. In Fig. 2, we have shown [10] the standard deviation curves of partial SEMF values, i.e., SEMF calculated without a particular term, to observe the impact of the absent term on σ. The figure clearly shows that the Coulomb and the Asymmetry terms contribute the most to the overall σ, the latter showing significant drop during the initial part of the curve, and then (about $1/6$th of the way) it rises above the overall BE/A curve.

The remaining SEMF terms — the Pairing term and to a lesser extent the Surface term — have a barely noticeable individual contribution, as seen in the figure. To explain these observed behaviours of the SEMF terms, we have drawn a representative graph of these terms in Fig. 3: the explanation can be found in the relatively high variation of the Coulomb and the Asymmetry terms with Z (as well as with A) compared to the Pairing and Surface terms. The high fluctuations in the Pairing term at low values of A [11] show up in Fig. 2, around the first few points of the x-axis, but require close scrutiny.

Another pattern that emerges out of Fig. 1 relates to the grouping: isotopic sequences have generally the lowest σ values, followed by isotonic and isobaric sequences. To quantify this behaviour, we decided to perform a statistical fit/regression with some function of known characteristics. The shape of the σ curves shows some similarity to a power-law function; finally, we settled on the following function (after some hit-and-trial [12]):

$$f(x) = a\,x^{-1} + b \tag{5}$$

[10] We have not included the Volume term in the plot as it a constant and therefore will not contribute to σ (see Eq. (4))

[11] In Fig. 3d, in the subplot for Pairing term, see the curve for A=10

[12] The choice of function was based on regression with several values for the power of x, leading to the subjective conclusion that taking a square root had the best combination of 'r-squared' goodness of fit values, optimum number of parameters and elegance of the fitting function

Time-series	**a**	**b**	r-squared
Isotopic (Z)	3.588	-0.342	0.956267
Isotonic (N)	4.251	-0.303	0.91717
Isobaric (A)	6.016	-0.375	0.97079

Table 1: Coefficients of a regression model (Eq. (5)) of standard deviation in BE/A data as a function of corresponding nuktriad variables.

where a and b are parameters to be determined from the fit. The values of the fit for different sequences are given in table 1. Now, the parameter a in the fitting function controls the gentleness of bending in the decreasing curve; higher the value of a, the gentler (or less steep) is the decrease of $f(x)$, and obviously the parameter b controls the vertical location of the curve. Values obtained for parameter a (table 1) show that the sharpest decrease is for isotopic sequence, while the isobaric sequence has the gentlest decrease. Fit lines are also plotted alongside the σ curves.

The various aspects of BE/A data as well as the SEMF appear prominently when we try to reimagine the data as time-series (instead of a scatter plot, c.f. Fig. 1) by sorting the entire dataset, first by one of the nuktriad variables, followed by another. The independent variable, or the x-axis, thus represents simply the order of arrangement of the dataset. Out of the six permutations possible for ordering any two of the nuktriad variables, we have chosen, for economy, three arrangements to represent isotopic, isotonic and isobaric sequences: (Z, N), (N, Z) and (A, Z). The choice stemmed from the assumed order of importance of the nuktriad variables in respect of nuclear binding energy: $Z > N > A$ [13]. For brevity, we shall continue with the same notation but with bold font, i.e., we shall denote as $(\mathbf{Z}, \mathbf{N})$ the sorting of data first along increasing Z values followed by increasing N values. This order of sorting, viz., $(\mathbf{Z}, \mathbf{N})$, leads to BE/A graph being arranged in segments, where each segment represents an isotopic sequence (a set of constant Z values) within which the neutron number (N) increases monotonically. The other two orders of arrangement, viz., $(\mathbf{N}, \mathbf{Z})$ and $(\mathbf{A}, \mathbf{Z})$, have similar interpretations — isotonic and isobaric sequences respectively — within which Z increases monotonically. Each segment in all of the three BE/A time-series analysed can be identified visually by their distinct downward-opening parabolic portions.

The time-series of BE/A data with different orders of sorting are shown in Figs. 4–6. Within the same subplot, we have included predictions from SEMF as well as the difference between the two. For reference, we shall call the plot of the difference between SEMF and data as the LDM disparity curve[14] (represented as $(\mathrm{SEMF} - \mathrm{data})$ in the figure).

We have included a zoomed section of the time-series (x-axis value from 2700 to 3000) to show detailed structures present in the plotted data. Corresponding nuktriad variables for the figures are plotted in the lower subplots. We have also included similarly transformed time-series of the various individual terms of the SEMF, so that the nature of their contribution to the total value can be appreciated. We have inset in the SEMF figure itself, a zoomed section of the plot.

The shapes of the A, Z and N scatter plots are trivial to explain, arising out of the time-series ordering and their simple relationship $A = Z + N$. Fig. 4a containing plots of the $(\mathbf{Z}, \mathbf{N})$ sorting clearly shows that it is the interplay between the Coulomb and the Asymmetry terms that gives rise to the parabolic segments in the time-series. We also see that the Surface term (see inset of Fig. 4a) strengthens the Coulomb term due to their co-directional trend. Obviously, they have a direct correspondence with Fig. 3. For $(\mathbf{Z}, \mathbf{N})$ time-series (Fig. 4b), each segment implies constant Z and increasing N, which leads to increasing A, and in Fig. 3, increasing A for a constant value of Z for Surface and Coulomb terms clearly indicates increasing energy values, which explains the corresponding increasing trend of these terms in Fig. 4a.

The Asymmetry term in Fig. 3c shows parabolas for constant A, the vertex of which occurs at $Z = N$. Before the vertex $(Z < N)$, on looking along a constant value of Z, the energy associated with the Asymmetry term increases with increasing A; and beyond the vertex $(Z > N)$, the energy starts decreasing — this results in a parabola for constant Z and increasing A also. These A-parabolas can be observed in the asymmetry term in Fig. 4a roughly before 700 units of the x-axis.

The parabolic segments in BE/A time-series in $(\mathbf{N}, \mathbf{Z})$ and $(\mathbf{A}, \mathbf{Z})$ sorting are also caused by the interplay between the Coulomb and the Asymmetry terms (Figs. 5a & 6a); the Surface term however changes affiliations here, acting collaboratively with the Asymmetry term and against the Coulomb term for $(\mathbf{N}, \mathbf{Z})$ sorting, while

[13] See table 1 and accompanying discussion; higher variation of BE/A within a nuktriad is assumed to imply more impact
[14] LDM for Liquid Drop Model

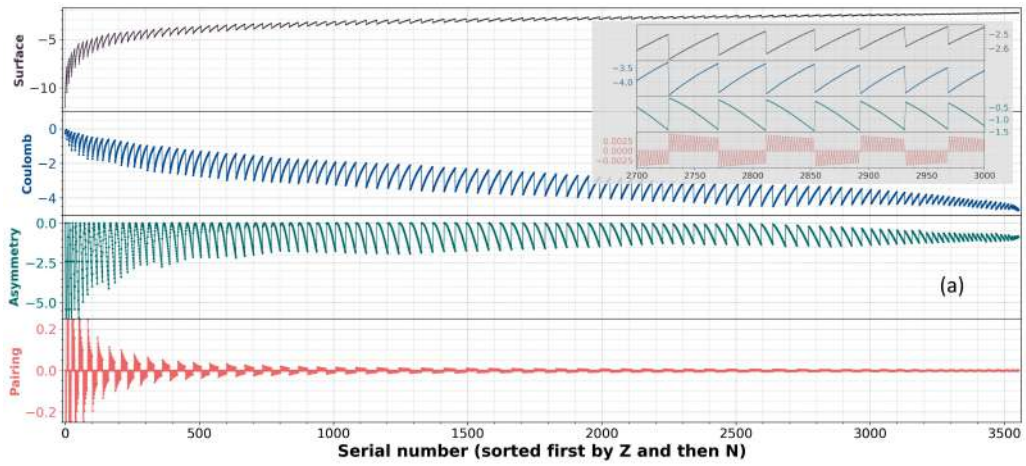

(a)

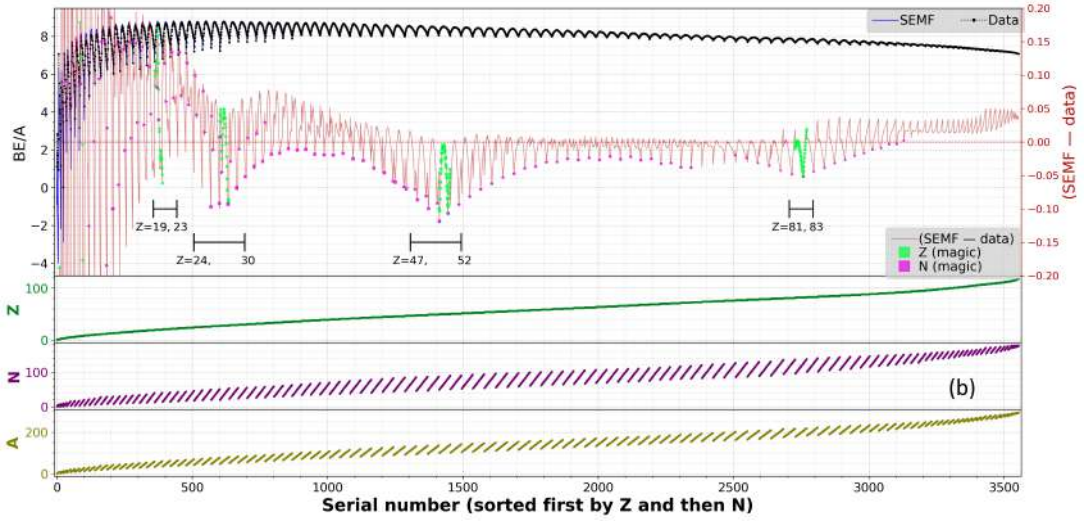

(b)

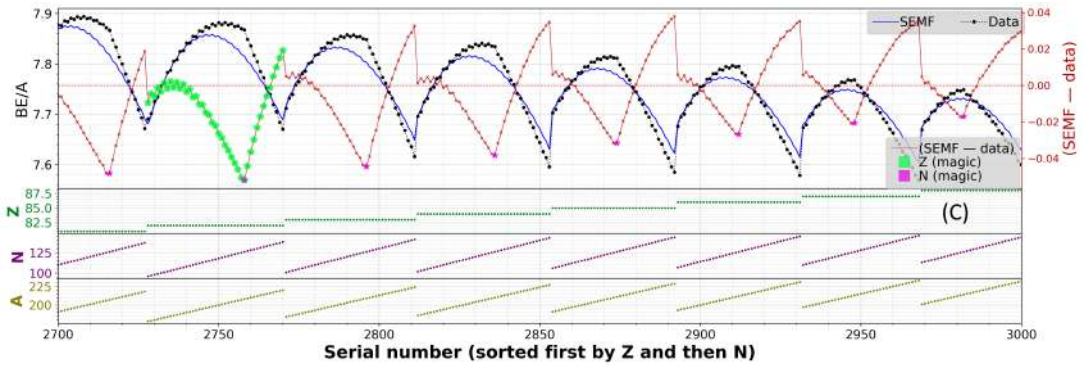

(c)

Figure 4: Time-series plots with (Z, N) sorting. Part (a) shows the various terms of the SEMF. Part (b) shows the BE/A time-series and associated graphs, and part (c) is a zoomed version of part (b) from 2700 to 3000 on the x-axis. The detailed legend for magic numbers is given in Fig. 10.

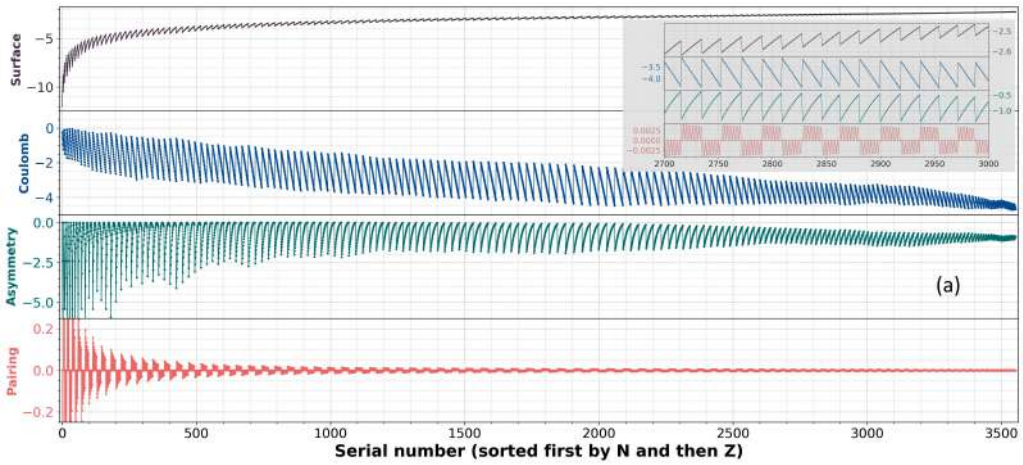

(a)

(b)

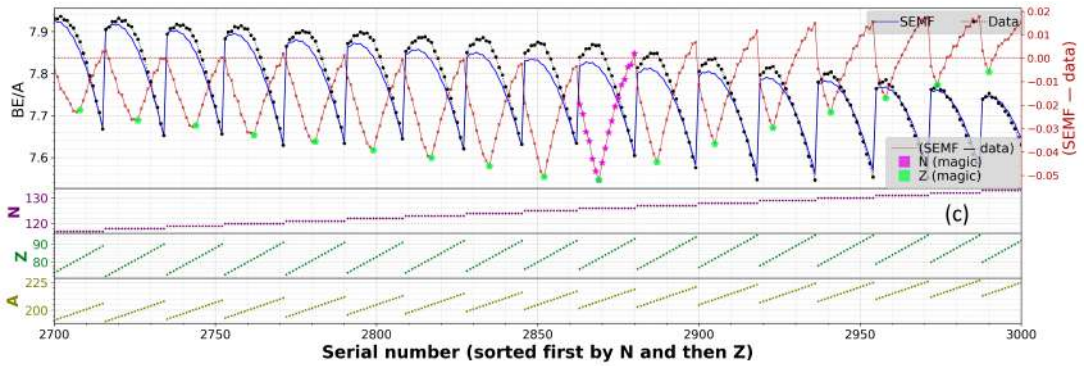

(c)

Figure 5: Time-series plots with (N, Z) sorting. Part (a) shows the various terms of the SEMF. Part (b) shows the BE/A time-series and associated graphs, and part (c) is a zoomed version of part (b) from 2700 to 3000 on the x-axis. The detailed legend for magic numbers is given in Fig. 10.

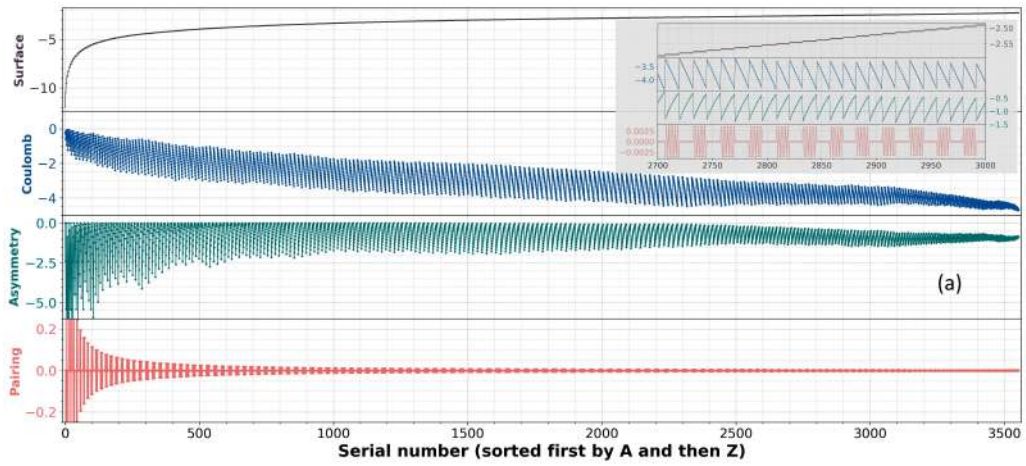

(a)

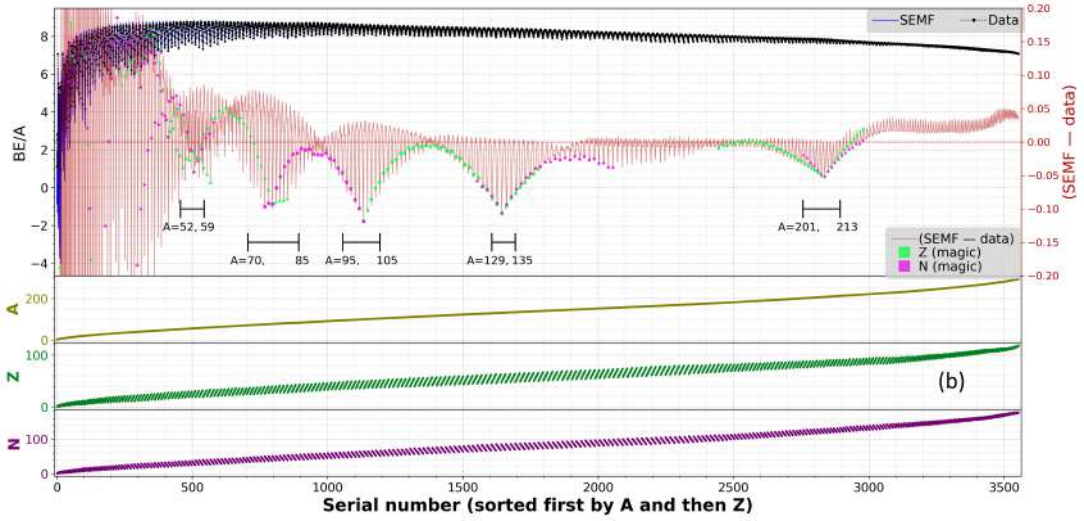

(b)

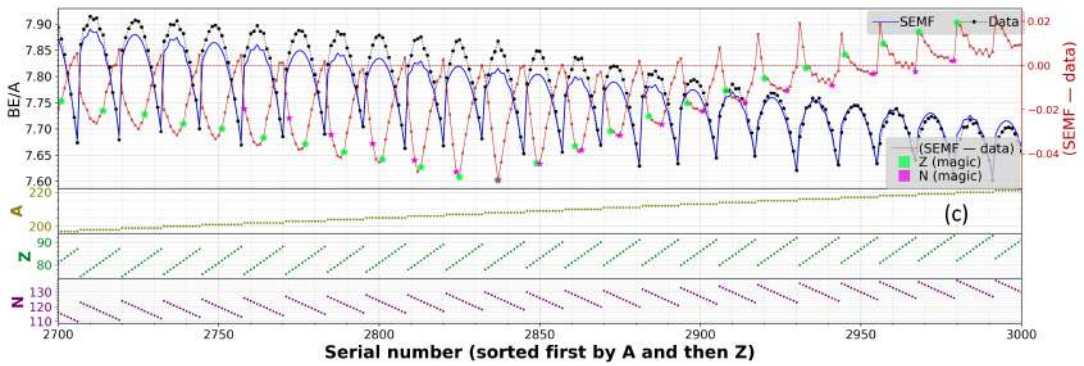

(c)

Figure 6: Time-series plots with $(\mathbf{A}, \mathbf{Z})$ sorting. Part (a) shows the various terms of SEMF. Part (b) shows the BE/A time-series and associated graphs, and part (c) is a zoomed version of part (b), from 2700 to 3000 of the x-axis. Detailed legend for magic numbers is given in Fig. 10.

remaining non-aligned/constant for the $(\mathbf{A}, \mathbf{Z})$ sorting. The necessity for shell correction in the SEMF clearly shows up in the LDM disparity curve patterns for all the three time-series (Figs. 4b, 5b & 6b), where we observe significant dips around the nuclear magic numbers $2, 8, 20, 28, 50, 82$, and 126 [29]. These are much more clearly visible in the zoomed plots (Figs. 4c, 5c & 6c). In the zoomed plot with $(\mathbf{Z}, \mathbf{N})$ sorting as well as the $(\mathbf{N}, \mathbf{Z})$ sorting (Figs. 4c & 5c), we see that the dips in the LDM disparity curve occur at magic numbers, with the deepest dip occurring for a doubly magic nuclide. The parabolic segments of BE/A plots are clearly not smooth; however, for these two orders of sorting, it appears as if two different curves are joined to form each segment [15], and the magic number appears at the point of joining.

For the $(\mathbf{A}, \mathbf{Z})$ sorting also, the deepest dip is a double magic number and beyond it, the dips in the LDM disparity curve also correspond to magic numbers. But, prior to the double magic number, the dips do not occur at magic numbers. In all three cases, the BE/A plots and the LDM disparity curve have a mirrored relation with respect to a horizontal line, i.e., the peaks of one occur at the trough of the other (reminiscent of sine and cosine curves). There is a slight systematic shift of this mirrored relationship (the peaks and troughs get misaligned) on one side as we move away from the double magic number.

We now explore one more tool in the time-series arsenal: differencing. We have plotted differencing for the aforementioned three arrangements of BE/A time-series in Figs. 7, 8 & 9, along with the corresponding proton and neutron separation energies (single and double) as subplots for comparison. The subplot for BE/A also includes the LDM disparity curve for comparison. A zoomed section of the figure (from serial number 2700 to 3000) is also given. Since our focus in this figure is the differencing curve, we have attached the markers for magic numbers to it instead of the LDM disparity curve as was done previously.

Differencing (Δx) is the simple process of taking the difference between successive terms of a time series, i.e.,

$$\Delta x_i = x_i - x_{i-1}. \tag{6}$$

Differencing with higher lags can also be taken; however, we confine ourselves to the first–order differencing. For the (Z, N) sorting, differencing will give (for each segment)

$$\Delta x_{(Z,N)} = \frac{BE(Z,N)}{A} - \frac{BE(Z,N-1)}{A-1}. \tag{7}$$

At the boundary, Z jumps to the next higher value (increases by 1), while N drops by an uncertain amount, obstructing a precise formula at the boundary. The above equation looks very similar to the formula for neutron separation energy (S_n) written in terms of binding energy [30]:

$$S_n(Z,N) = BE(Z,N) - BE(Z,N-1). \tag{8}$$

Similarly, the differencing of (N, Z) time-series resembles proton separation energy (S_p) [31]:

$$\Delta x_{(N,Z)} = \frac{BE(N,Z)}{A} - \frac{BE(N,Z-1)}{A-1}, \tag{9}$$

$$S_p(N,Z) = BE(N,Z) - BE(N,Z-1). \tag{10}$$

These similarities can be verified in Figs. 7 and 8.

For the differencing of (A, Z) time-series, each segment consists of a constant A and increasing Z. Thus, we obtain

$$\Delta x_{(A,Z)} = \frac{1}{A}\left[BE(A,Z) - BE(A,Z-1)\right]. \tag{11}$$

Thus, for a segment with even A, both Z and N will be either odd or even, alternating between the two possibilities as they move forward. This causes sharp changes in the binding energy, producing the zigzag behaviour for even A observed in Fig. 9b. For odd A, both Z and N will have opposite even–odd character, and therefore a smoother change is observed for the differencing. For the other two time-series, $(\mathbf{Z}, \mathbf{N})$ and $(\mathbf{N}, \mathbf{Z})$, no matter the nature of the first variable (odd or even), the other variable alternates between odd and even when moving forward, thus causing the observed zigzag behaviour for all segments. The (A, Z) differencing has a relation to β-decay energetics [30]. Clearly, if we had taken only BE instead of BE/A, the connection between differencing and separation energies would have been more direct.

With respect to magic numbers, we find that in $(\mathbf{Z}, \mathbf{N})$ and $(\mathbf{N}, \mathbf{Z})$ time-series (Figs. 7b & 8b), there is a comparatively larger dip in the differencing plot at the position of the magic number that is also mimicked in the

[15] This behaviour is much more prominent for $(\mathbf{Z}, \mathbf{N})$ graphs.

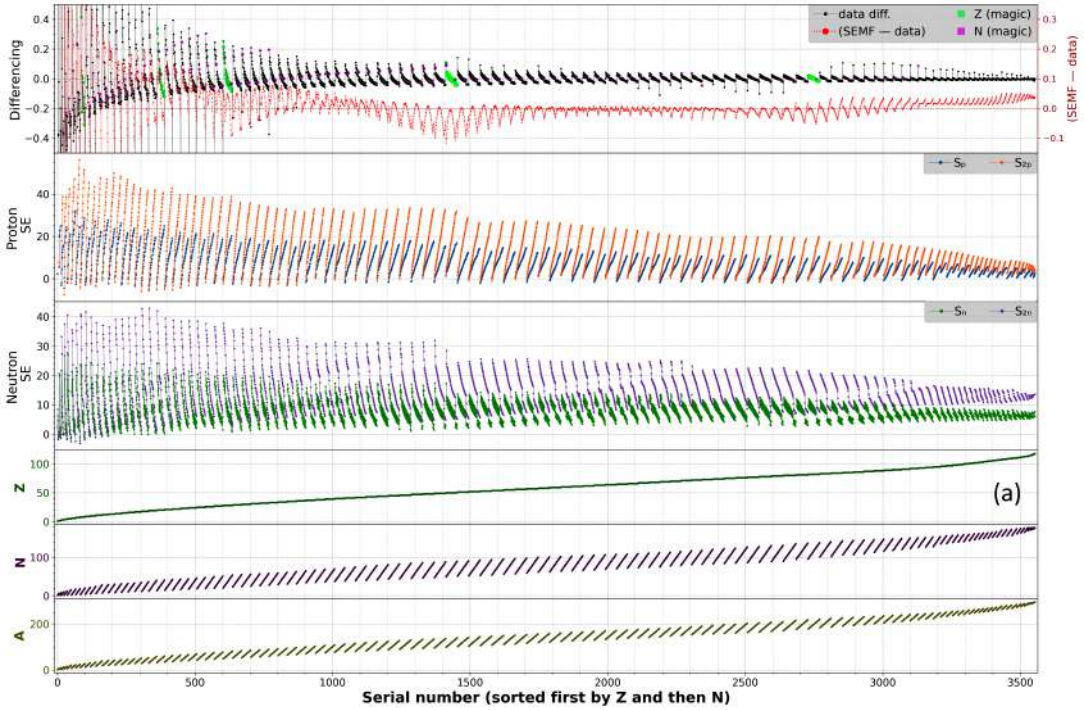

(a)

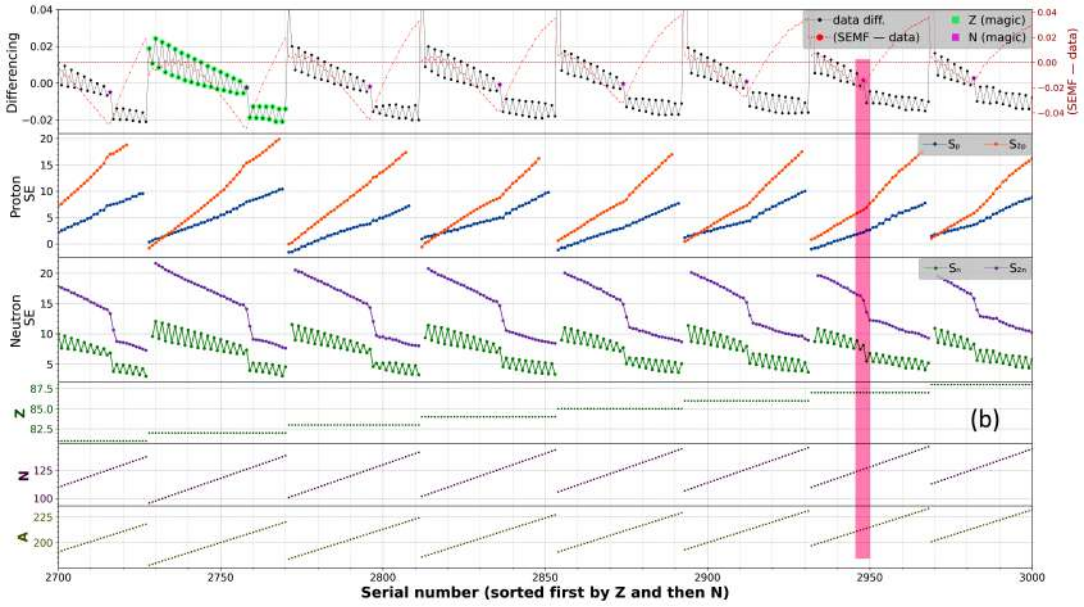

(b)

Figure 7: Time-series plots with (Z, N) sorting. Part (a) shows differencing and LDM disparity curve, along with magic numbers and part (b) is a zoomed version of part (a), from 2700 and 3000 of the x-axis. Detailed legend for magic numbers is given in Fig. 10.

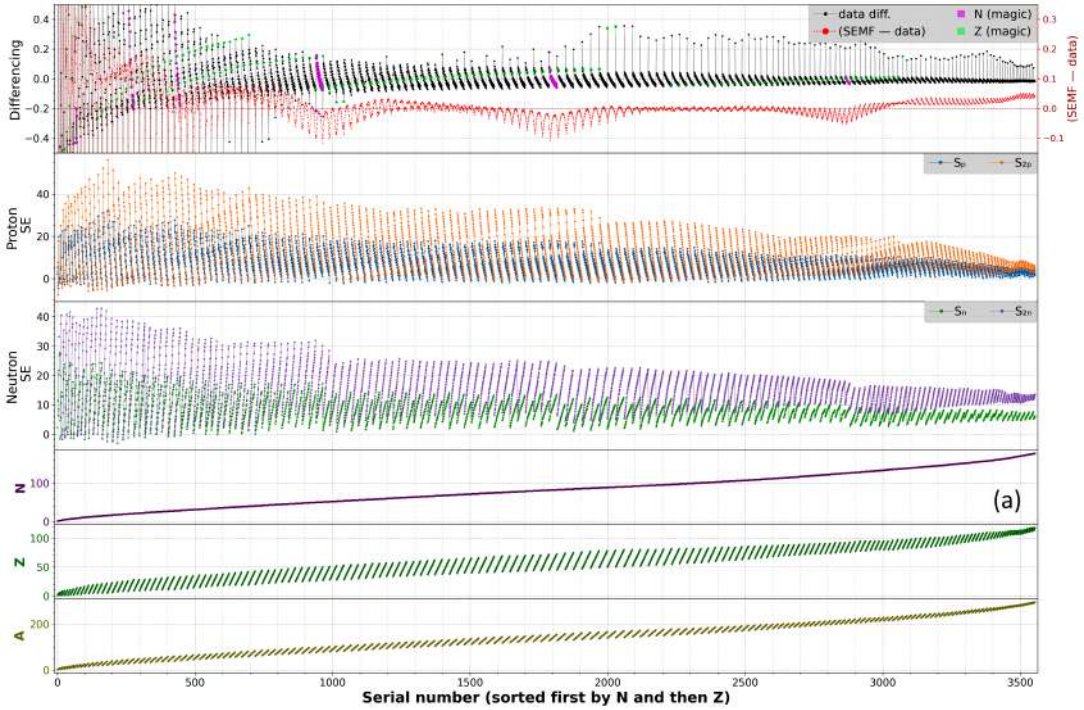

(a)

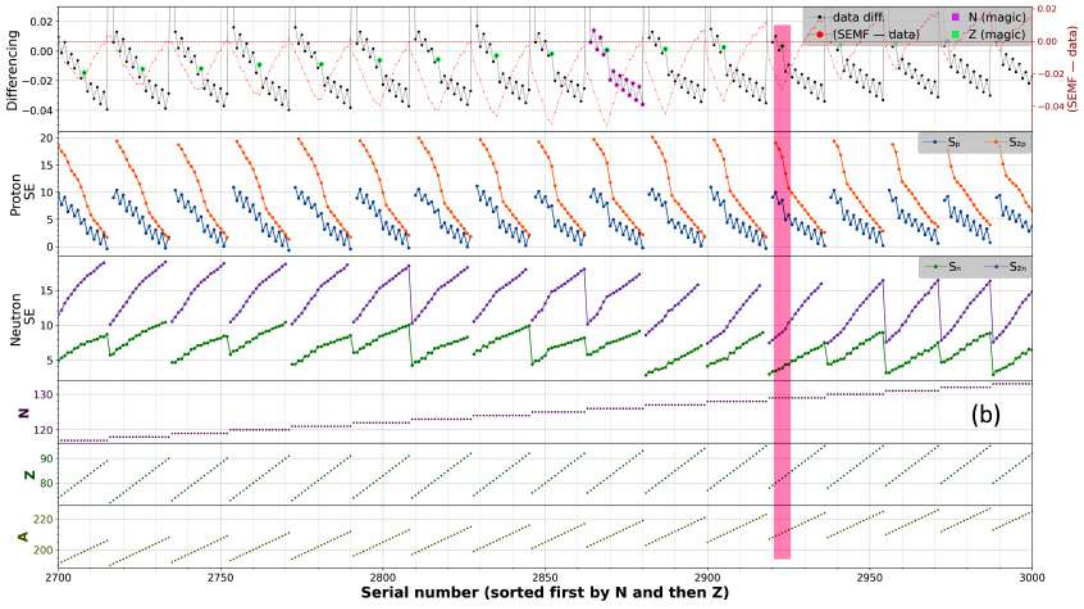

(b)

Figure 8: Time-series plots with (N, Z) sorting. Part (a) shows differencing and LDM disparity curve, along with magic numbers and part (b) is a zoomed version of part (a), from 2700 and 3000 of the x-axis. Detailed legend for magic numbers is given in Fig. 10.

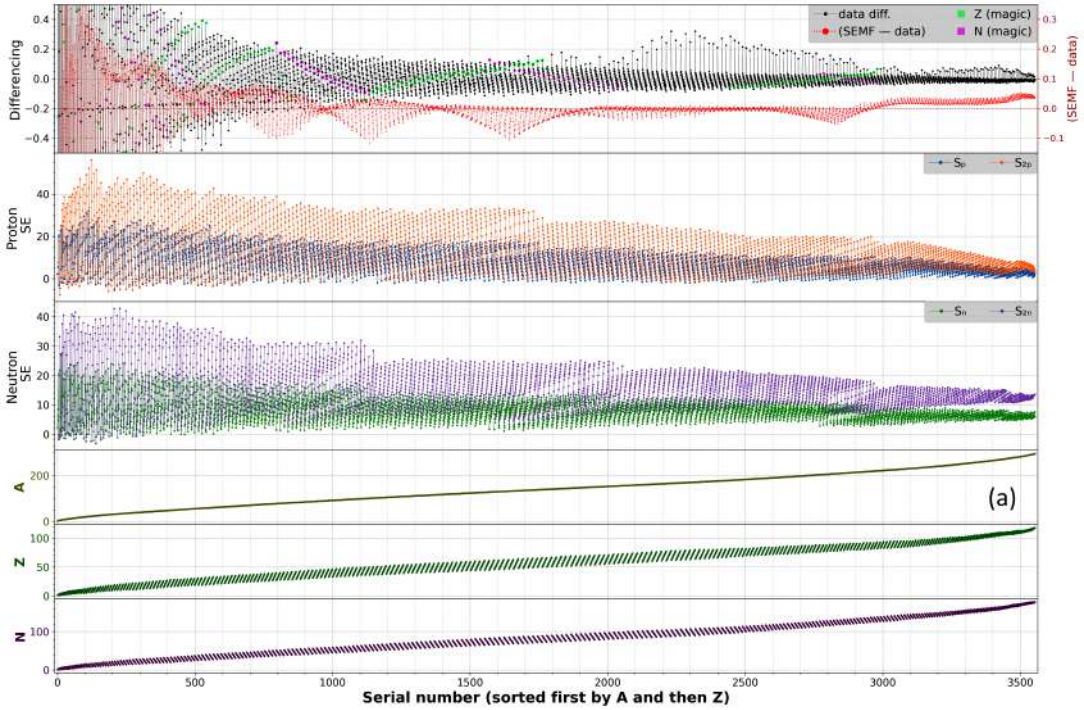

(a)

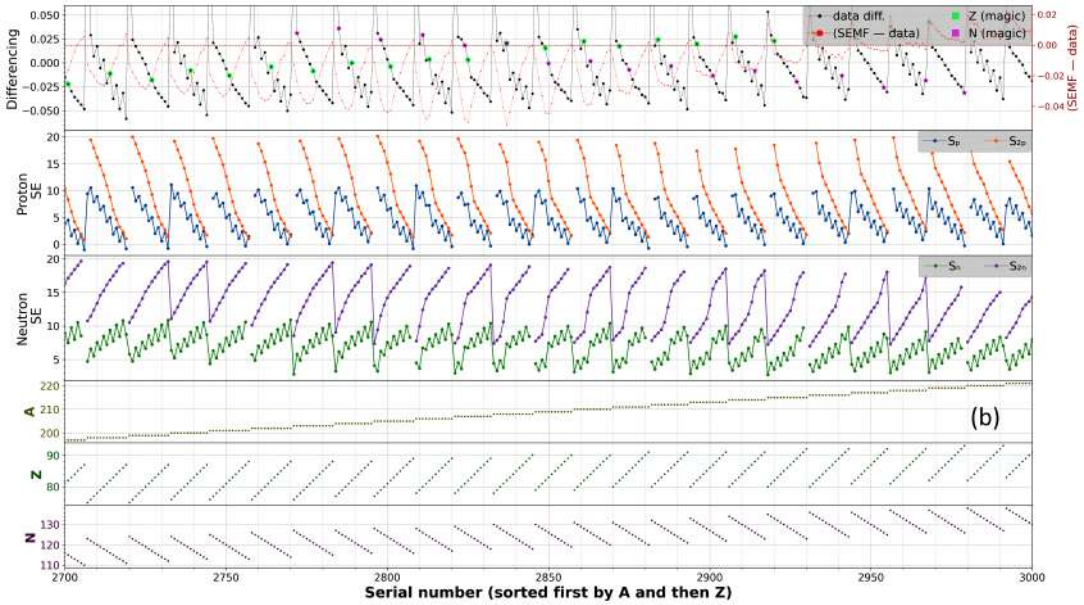

(b)

Figure 9: Time-series plots with (A, Z) sorting. Part (a) shows differencing and LDM disparity curves, along with magic numbers, and part (b) is a zoomed version of part (a), from 2700 and 3000 on the x-axis. A detailed legend for magic numbers is given in Fig. 10.

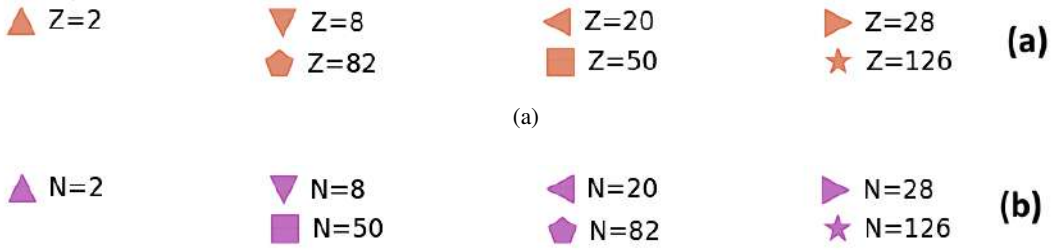

Figure 10: Plot legend for different magic numbers used in Figs. 4-9.

S_n and S_{2n} curves (and the S_p and S_{2p} for $(\mathbf{N}, \mathbf{Z})$); we have highlighted a single example in the corresponding figures for easy identification. Behavior of $(\mathbf{A}, \mathbf{Z})$ in relation to the magic numbers is discernibly without any pattern.

As mentioned previously, there is a correspondence between differencing and nucleon separation energies; we have tried to quantify this using the Pearson correlation. We have also calculated the correlation between differencing and the LDM disparity curve to estimate the linear relationship between them. Although correlation is a cruder tool that compresses the rich interplay in a pair of variables to a single number, it can be useful for summarizing. Table 2 lists the values of the correlation coefficients; all the reported coefficients have extremely low p-values indicating the correlations are statistically significant (not surprising given the substantial number of data points).

For each nuktriad variable, we see a pair of positive and a pair of negative correlations with the separation energies. The correlation with the LDM disparity curve (i.e., $(\mathrm{SEMF}-\mathrm{data})$) is found to be positive and relatively high across all three sorting arrangements. This indicates that there exists systematic variation in the data that is not accounted for by the SEMF; otherwise, it would have been nearer zero, implying no correlation. It is tempting to hypothesise that there might be more terms than just the shell corrections that might be contributing to the correlation, but a coherent supporting argument is beyond the expertise of the author; hence, we leave it at that.

Variable	**Z**	**N**	**A**
$(\mathrm{SEMF}-\mathrm{data})$	0.232	0.369	0.289
S_p	-0.162	0.577	0.523
S_{2p}	-0.142	0.622	0.559
S_n	0.535	-0.164	-0.327
S_{2n}	0.542	-0.144	-0.343

Table 2: Coefficient values for Pearson Correlation of BE/A time-series differencing with LDM disparity curve and single and double nucleon separation energies.

Besides the features discussed above, these time series have a host of other interesting features, investigation of which may take up more room than traditionally delimited for a journal article; hence, we also leave it for now. To quote an example of the interesting features not enumerated, we observe that for x-axis values roughly between 2000 and 2500 (Figs. 4b, 5b & 6b), high-frequency dips in the LDM disparity curve for all three sets of BE/A time-series do not have any associated magic numbers — this inconsistency may lead to interesting discussions.

The other aspect of the current paper is appreciation of visual approaches to understanding data, which can also be helpful in clarifying the connections to the underlying equations; these kinds of visual and sensory approaches to learning have also been explored by a few authors [32].

4 Conclusion

We have explored patterns in BE/A from the NuDat3/AME2020 dataset. On analysing the standard deviations of isotopic, isotonic and isobaric sequences, we found that variation within isotopic sequence is largest compared to the others, while isobaric sequence has the least variation. Time-series transformation of the BE/A data revealed interesting pattern and connection with other variables; some of which were identified and discussed in the light

of the semi-empirical mass formula. We found that differencing of the time-series can be related to proton/neutron separation energies; computed correlations indicate paired responses. Besides exploration, these transformation and visualization tools can be useful in pedagogy.

References

[1] M. Wang, W. J. Huang, F. G. Kondev, G. Audi, and S. Naimi, Chinese Physics C **45**, 030003 (2021).

[2] National Nuclear Data Center (NNDC), Nudat 3.0, `https://www.nndc.bnl.gov/nudat3/`.

[3] T. H. Levere, *Transforming Matter: A History of Chemistry from Alchemy to the Buckyball* (Johns Hopkins University Press, 2003).

[4] I. Kaplan, *Nuclear Physics* (Narosa Publishing House, New Delhi, 2020).

[5] F. W. Aston, Proceedings of the Royal Society of London. Series A **115**, 487 (1927).

[6] F. W. Aston, Nature **120**, 956 (1927).

[7] W. D. Harkins and T. H. Liggett, Journal of Physical Chemistry **28**, 74 (1924).

[8] J. Chadwick, Proceedings of the Royal Society of London. Series A **136**, 692 (1932).

[9] H. A. Bethe and R. F. Bacher, Reviews of Modern Physics **8**, 82 (1936).

[10] C. F. von Weizsäcker, Zeitschrift für Physik **96**, 431 (1935).

[11] B. R. Martin and G. Shaw, *Nuclear and Particle Physics: An Introduction*, 3rd ed. (Wiley, 2019).

[12] P. J. Mohr, D. B. Newell, B. N. Taylor, and E. Tiesinga, Reviews of Modern Physics **97**, 025002 (2025).

[13] D. Benzaid, S. Bentridi, A. Kerraci, and N. Amrani, Nuclear Science and Techniques **31**, 9 (2020).

[14] B. Pandey *et al.*, AIP Advances **14**, 105228 (2024).

[15] D. Cha and B. Kim, Journal of the Korean Physical Society **56**, 1546 (2010).

[16] S. Gora, O. S. K. S. Sastri, and S. K. Soni, European Journal of Physics **43**, 035802 (2022).

[17] A. Saad, Z. I. Elghobary, and M. Taha, Bulletin of the Faculty of Science, Zagazig University , 66 (2025).

[18] S. Lakshminarayana, Preprint (2025).

[19] T. W. Anderson, *The Statistical Analysis of Time Series* (John Wiley & Sons, 2011).

[20] R. H. Shumway and D. S. Stoffer, *Time Series Analysis and Its Applications* (Springer, 2017).

[21] P. Song and C. T. Russell, Space Science Reviews **87**, 387 (1999).

[22] S. Li and A. Adelmann, Physical Review Accelerators and Beams **26**, 024801 (2023).

[23] W. J. Huang, M. Wang, F. G. Kondev, G. Audi, and S. Naimi, Chinese Physics C **45**, 030002 (2021).

[24] W. McKinney, in *Proceedings of the 9th Python in Science Conference* (2010) pp. 56–61.

[25] The pandas development team, pandas-dev/pandas: Pandas 2.2.3 (2025).

[26] P. Virtanen *et al.*, Nature Methods **17**, 261 (2020).

[27] J. D. Hunter, Computing in Science & Engineering **9**, 90 (2007).

[28] A. Holmes, S. Dean, and A. H. Barbar, *Introductory Business Statistics 2e* (OpenStax, 2023).

[29] D. Steppenbeck *et al.*, Nature **502**, 207 (2013).

[30] J. M. Blatt and V. F. Weisskopf, *Theoretical Nuclear Physics* (Springer, 1979).

[31] S. Athanassopoulos, E. Mavrommatis, K. A. Gernoth, and J. W. Clark, Preprint (2005).

[32] M. Hein, A. Pusch, and S. Heusler, European Journal of Physics **43**, 035801 (2022).

SYNTHESIS AND DIELECTRIC PROPERTIES ANALYSIS OF POLYTHIOPHENE NANOPARTICLES

Paragjyoti Chutia*[1]

[1]*Department of Physics, DHSK College, Dibrugarh-786001, Assam, India*

*Corresponding Author: paragjyotic@gmail.com

(Received 13 September 2025; revised 3 January 2026; accepted 14 January 2026; published 6 April 2026)

Abstract: Polythiophene nanoparticles were synthesized using a cationic surfactant-assisted chemical oxidative polymerization technique. Morphological, dielectric relaxation, and AC conductivity analyses were carried out with systematically varying CTAB concentrations. HRTEM images show well-ordered nanoparticles. X-ray diffraction patterns reveal a new diffraction peak at $2\theta = 26.6^\circ$ at higher CTAB concentrations, indicating an enhancement of the conjugation length. Dielectric permittivity studies show that at lower frequencies ($< 10^5$ Hz), the relaxation is dominated by the electrode polarization effect. AC conductivity analysis suggests the presence of a correlated barrier hopping mechanism. In the scaling approach, the AC conductivity data obtained at different temperatures superimpose on one another, suggesting a temperature-invariant conduction process.

Keywords: polythiophene. Nanoparticles. dielectric permittivity. AC conductivity. electric modulus.

PACS: 61.10.Nz, 68.37.Lp, 77.22.Ch

1 Introduction

Polymers with heteroaromatic rings have received an enormous deal of interest among researchers in the last two decades [1, 2]. Electronic properties of conjugated conducting polymers can be manipulated through changing doping level and modifying its structure from insulating to metal [3]. Conducting polymers are widely used in different technological applications such as electrodes, sensors, actuators, light emitting diodes, etc. [4, 5]. Among the diversity of intrinsically conducting polymers polythiophene (PTh) is widely studied because its promising electronic and optical properties, natural constancy against oxygen and moisture, structural versatility, high conductivity and wide commercial applications [6]. Polythiophene can be obtained from the polymerization of thiophene through chemically, photo-chemically, electrochemically [7, 8]. Some notable applications of typical PTh derivatives are molecule-based devices, rechargeable battery electrodes, light-emitting diodes, chemical and optical sensors etc. [9, 10]. Among the family of conjugated conducting polymers, Polythiophene and its derivatives have received significant interest among scientist owing to their superior stability, ease of structural change, flexible optical and electrochemical behaviors [11]. The dielectric and modulus formalism can be employed to understand the charge transport process in disordered systems. The movement of charge carriers and orientations of dipoles in polymer determines AC conductivity and dielectric relaxation. Interfacial polymerization in disordered polymeric materials or in polymeric composite materials arises because of dopant ions, fillers, or other impurities present in the system. At low frequencies the interfacial polarization is covered by the conductivity and high permittivity values [12]. The charge carriers relaxation process and different polarization mechanism present in a system can be understood through modulus formalism and dielectric formalism, respectively. The presence of charge carrier hopping mechanism in conducting polymers, results the conductivity relaxation which is different from the dielectric relaxation in common polymers. The electrode polarization outcomes the high values of permittivity at lower frequencies which get concealed in the modulus formalism [13].

Dielectric and AC conductivity of Polyaniline, Polypyrrole and PEDOT nanostructures have been widely studied by many research groups in recent years [14–16] but synthesis and dielectric properties study of polythiophene

nanostructured systems are limited. The present paper investigates the dielectric and charge transport properties of PTh nanoparticles. Further, the effect of CTAB concentrations on structural, dielectric and transport properties has also been studied.

2 Experimental

2.1 Materials

Sigma Aldrich company prepared thiophene monomer has been used for synthesis of polythiophene. The oxidant ferric chloride ($FeCl_3$), chloroform, surfactant N, N, N-Trimethyl-1-hexadecanaminium bromide (CTAB), methanol and acetone were purchased from Merck.

2.2 Preparation of polythiophene nanoparticles

Cationic surfactant-assisted chemical oxidative polymerization procedure has been employed to synthesis Polythiophene (PTh) nanoparticles. In present synthesis procedure thiophene monomer (0.024 mol) and surfactant CTAB (0.003 mol) were dissolved in $CHCl_3$ (20 ml) and kept under stirring for 15 m. $FeCl_3$ (0.0055 mol) was added in $CHCl_3$ (70 ml) and poured drop wise to the monomer-surfactant solution under stirred conditions [17]. The synthesis process was being carried out at room temperature and kept stirring for 24 h. The obtained dark-brown precipitates were first subjected to centrifugation to separate the solid product from the reaction medium. The supernatant containing unreacted species was carefully removed, and the collected final product was repeatedly washed with deionized water and ethanol to ensure effective removal of residual reactants and by-products. Each washing step was followed by centrifugation. Finally, the purified nanoparticles were dried under vacuum at 70°C for 6 h to remove physically adsorbed moisture and residual solvents, yielding the final purified product. For CTAB concentrations 1 mmol, 2 mmol, 3 mmol, 4 mmol and 5 mmol the samples are named as C1, C2, C3, C4 and C5, respectively. Block diagrams of the synthesis and purification steps are depicted in Fig. 1(a) and Fig. 1(b), respectively.

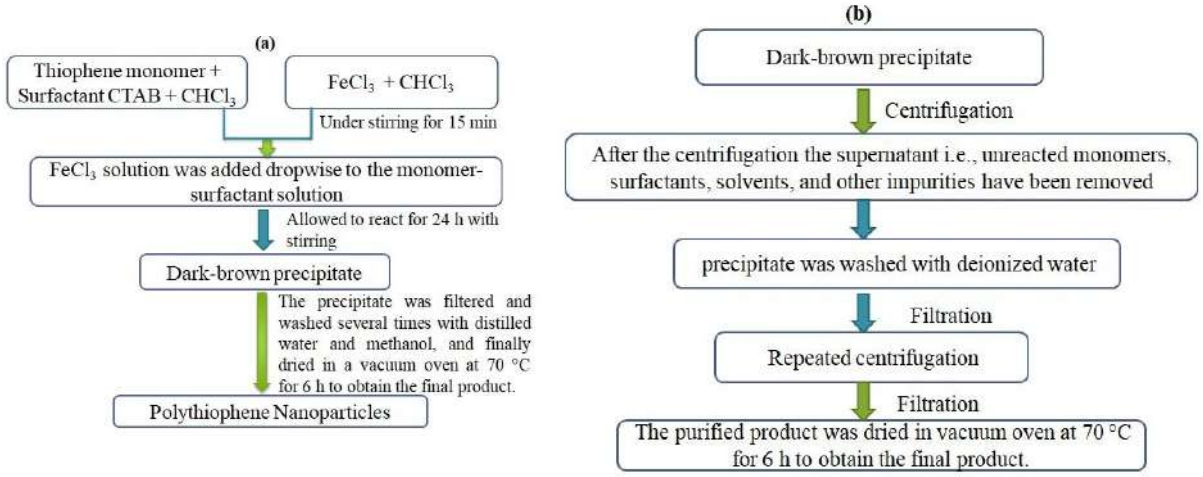

Figure 1: Block diagram of (a) synthesis of polythiophene nanoparticles and (b) purification steps of obtained dark-brown polythiophene nanoparticles precipitates.

2.3 Characterization

The shape and size of the PTh nanoparticles were observed with high-resolution transmission electron microscope (HRTEM, JEM-2100, 200 kV, Jeol). Bruker D8 Advance X-ray diffractometer was employed for X-ray diffraction analysis. Nicolet Impact I-410 FTIR spectrometer was being used to study FTIR spectra between 400 cm^{-1} to 4000 cm^{-1}. The thermal measurement was carried out by employing the Perkin Elmer thermal analyzer TGA 6000 in nitrogen environment from room temperature to $\sim$ 900°C at heating rate of 10°C min^{-1}. HIOKI-LCR

meter (frequency range: 42 Hz - 5 MHz) was being used for Dielectric measurements within temperature of 303 K - 363 K.

3 Results and Discussion

3.1 HRTEM study

HRTEM images of PTh samples C1 and C5 are depicted in Fig. 2(a & b) The HRTEM micrographs show the formation of fairly well-ordered spherical PTh nanoparticles. The diameter of the nanoparticles varies from 10 to 20 nm for sample C1 (Fig. 2(a)) and 2 to 6 nm for sample C5 (2(b)). From the HRTEM micrographs, it is seen that there is a reduction of particle size with increasing CTAB concentration. At high concentrations, the surfactant CTAB molecules surround the PTh nanoparticle which prevents the access of thiophene monomers to nanoparticles inhibiting the secondary growth during polymerization resulting in a smaller diameter of PTh nanoparticles [18].

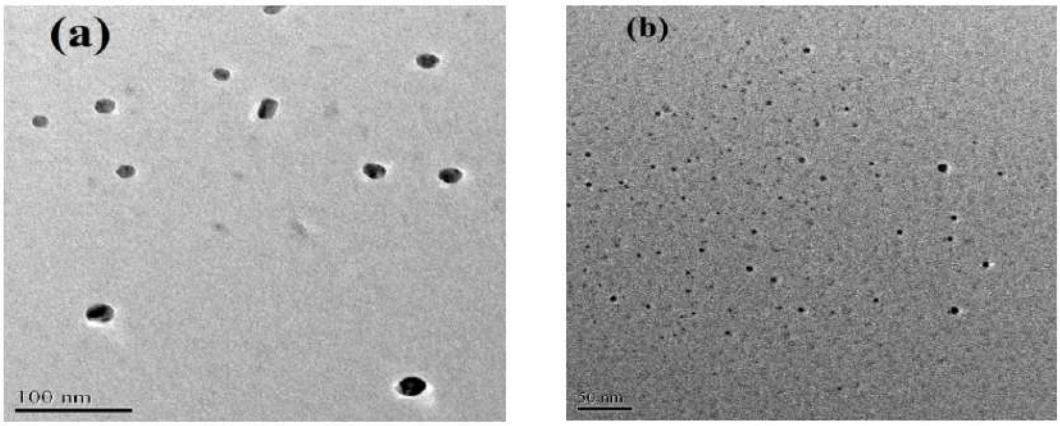

Figure 2: HRTEM micrographs of PTh nanoparticles (a) C1 and (b) C5

3.2 XRD study

Fig. 3(a) depicts XRD patterns of synthesized PTh nanoparticles. Broad diffraction peak in the 2θ range of $15^\circ - 25^\circ$ is observed for all the samples. The amorphous diffraction hump is attributed to the intermolecular $\pi - \pi$ stacking energies [19]. From the figure, it is observed that at higher CTAB concentration (C5) a new peak at around $2\theta = 26.6^\circ$ appears, which can be ascribed to the enhancement of π-conjugation length of the PTh nanoparticles [20].

3.2.1 Estimation of crystallite size (D) and lattice strain (ϵ) by using single-line approximation method

Crystallite size and strain results peak broadening and XRD patterns can be used to determine these parameters [21]. Instrumental and sample-dependent effects results the width of diffraction peak. Well annealed Cu powder was used to eliminate the instrumental broadening [22]. The single-line approximation method has been carried out employing the Voigt function considering that the Cauchy component β_C^f is due to size effect, whereas β_G^f is solely due to micro-strain [23]. According to the method, the crystallite size or domain size and the maximum value of the strain can be expressed as [24],

$$D = \frac{\lambda}{\beta_C^f \cos\theta} \tag{1}$$

and

$$\epsilon = \frac{\beta_G^f}{4\tan\theta} \tag{2}$$

In this report, although the peaks appear broad due to the amorphous nature of polythiophene, a discernible hump within the 2θ values of 15° to 30° becomes more defined upon doping, suggesting the onset of short-range

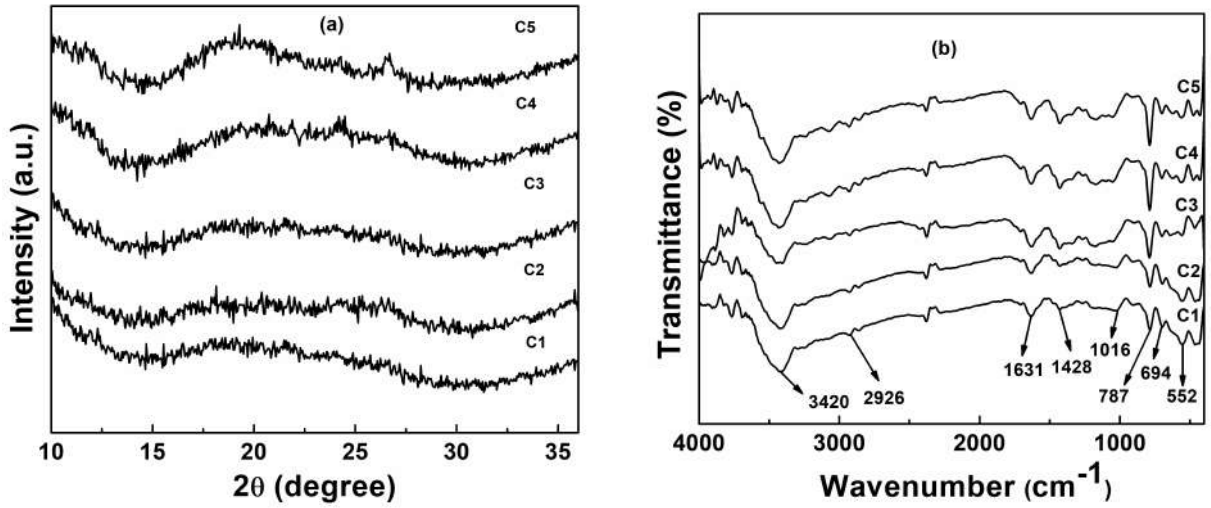

Figure 3: (a) XRD patterns of PTh nanoparticles with varying CTAB concentration and (b) FTIR spectra of PTh nanoparticles for different CTAB concentrations.

ordering of polymer chains Crystallite size and strain can be obtained from the single-line approximation method. Crystallite size (D) and strain (ϵ) values obtained from X-ray diffraction analysis is presented in Table 1. With increasing CTAB concentration, crystallite size decreases and it can be ascribed to a decrease in nanoparticles size as confirmed by the HRTEM micrograph. Dislocations and point defects may results in strain in the PTh nanoparticles [25], which are found to increase with increasing CTAB concentration. The increase of strain with increasing CTAB concentration results due to a decrease of particle size as confirmed by HRTEM.

Sample name	D(Å)	ϵ	I_{sym}/I_{asym}
C1	8.32	0.00813	0.96
C2	8.12	0.00934	0.89
C3	6.75	0.01101	0.68
C4	4.61	0.01223	0.65
C5	2.12	0.01342	0.62

Table 1: Structural parameters for the samples C1, C2, C3, C4 and C5

3.3 FTIR analysis

Fig. 3(b) represents the FTIR spectra of PTh nanoparticles for different CTAB concentrations. The O-H stretching absorption band arises at 3420 cm^{-1} and 2926 $^{-1}$ result from of water in KBr [26] and aliphatic C-H stretching vibration [27]. The C=C asymmetric and symmetric stretching vibration modes of the thiophene ring are observed at 1631 and 1428 cm^{-1}, respectively. The bands at 1016, 787, 694 and 552 cm^{-1} are attributed to the C-H in-plane deformation, C-H out-of-plane deformation, C-S bending and C-S-C ring deformation, respectively [17, 27]. The area intensity ratio, Isym/Iasym of the bands at 1428 $^{-1}$ and 1631 cm^{-1} give information about the chain length of the polymer. The lower value of the intensity ratio indicates the longer chain length [28]. From the calculated intensity ratio (I_{sym}/I_{asym}) of PTh nanoparticles, it has been observed that the intensity ratio (I_{sym}/I_{asym}) shows a decreasing trend at higher CTAB concentration, suggesting an increase in conjugation length. The obtained values are listed in Table 1. The sharp asymmetric band at 1631 cm^{-1} signifies that PTh nanoparticles are composed of long coplanar conjugated segments [28]. The increasing sharpness of the asymmetric band with increasing CTAB concentration indicates the increase of coplanar conjugated segments.

3.4 Thermal analysis

The degradation behavior of the PTh nanopartices were studied using thermogravimetric analysis (TGA). The thermogravimetric plots of PTh nanoparticles is presented in Fig. 4. The TGA studies indicate three steps of degradation. Evaporation of physically adsorbed water molecules in the polymer chains results the first step weight losses in the temperature range $30 - 150°$C. The weight loss observed in the temperature range of $330 - 495°$C is ascribed to the elimination of surfactant from the polymer shackle. The third step of weight loss begins at $495°$C due to the degradation of polymer backbone [29]. From the thermogram spectra, an enhancement of thermal stability with increasing CTAB concentration is observed. For sample C1 the weight loss is 17% up to the temperature of $495°$C whereas for sample C5 it is decreased to 11%. As confirmed by XRD analysis, the enhancement of thermal stability for higher CTAB concentration may be due to the increased crystallinity and crystallite size of the PTh nanoparticles.

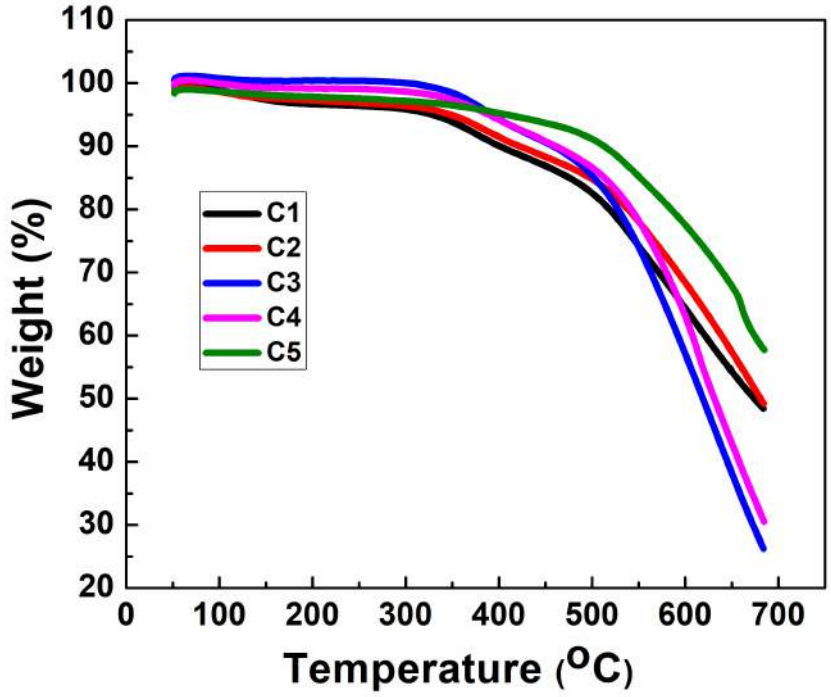

Figure 4: TGA plots of PTh nanoparticles for different CTAB concentration.

3.5 Dielectric properties analysis

The alternating electric field can polarize an electrical medium and which can be understood through the study of dielectric properties. Under the application of alternating electric field to a dielectric the polarization occurs because of displacement of electrical charges from their equilibrium. Eq. (3) describes how the dielectric parameter changes with frequency [22],

$$\epsilon^*(\omega) = \epsilon'(\omega) - i\epsilon''(\omega). \tag{3}$$

here $\epsilon'(\omega)$ and $\epsilon''(\omega)$ represents the real and imaginary components of the complex dielectric permittivity $\epsilon^*(\omega)$, respectively. Here $\epsilon'(\omega)$ measured the energy stored and the amount of energy dissipated can be obtained from $\epsilon''(\omega)$. The values of $\epsilon'(\omega)$ and $\epsilon''(\omega)$ can be obtained from the expressions,

$$\epsilon'(\omega) = \frac{Cd}{\epsilon_o A} \tag{4}$$

and the imaginary part $\epsilon''(\omega)$ as,

$$\epsilon''(\omega) = \epsilon'(\omega) \tan\delta(\omega) \tag{5}$$

where d and A represents thickness and area of the pellet, respectively. ϵ_o and $\tan\delta(\omega)$ are the permittivity in free space and loss tangent, respectively. Fig. 5(a) shows the plot of ϵ' as a function of frequency for PTh nanoparticles synthesized with varying CTAB concentrations at ambient temperature. The enhanced $\epsilon'(\omega)$ at low frequencies ($< 10^5$ Hz) due to the space-charge polarization resulting from interfacial charge buildup at the sample–electrode interfaces [30].

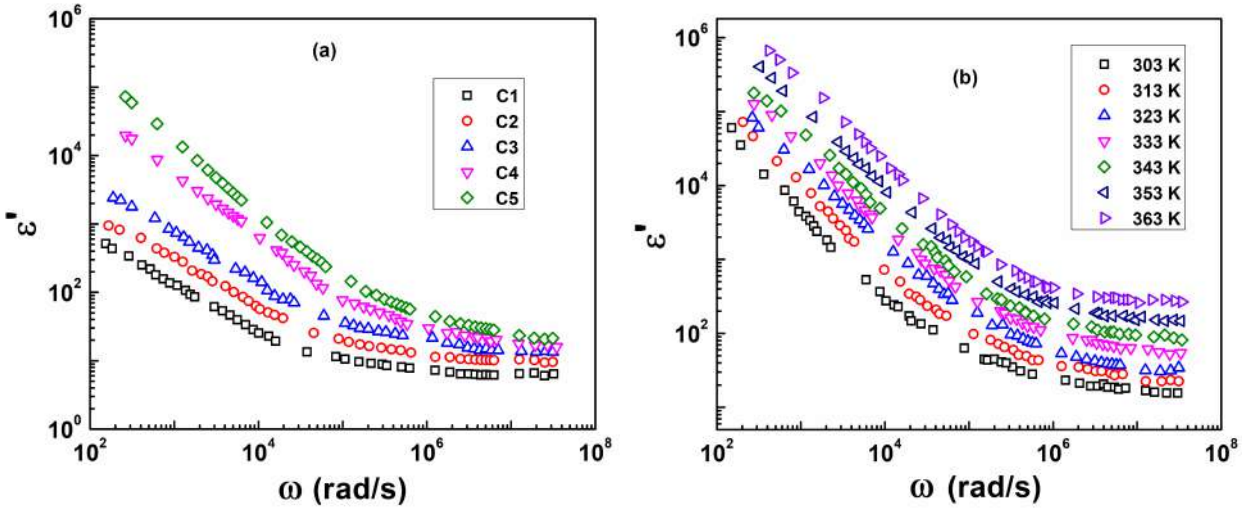

Figure 5: (a) Frequency dependence real permittivity (ϵ') of PTh nanoparticles for different CTAB concentrations at ambient temperature and (b) ϵ' vs. ω for C5 in the temperature range 303 K-363 K.

Fig. 5(b) depicts the frequency-dependent variation of $\epsilon'(\omega)$ for sample C5 at different temperatures. An increase in $\epsilon'(\omega)$ with rising temperature is observed, which is ascribed to enhanced dipolar orientation induced by greater thermal energy at elevated temperatures [31]. At higher temperatures, a pronounced increase in the dielectric constant is evident, resulting from enhanced total polarization within the system. This enhancement is attributed to the activation of both induced dipoles and thermally stimulated trapped charge carriers. With increasing temperature, the thermal energy imparted to the system facilitates polymer chain mobility, thereby reducing pinning effects that otherwise restrict charge carrier transport. The enhanced mobility promotes greater charge carrier participation in relaxation processes at a given frequency. Accordingly, the combined effects of improved dipolar orientation and increased charge carrier contribution lead to an overall rise in the dielectric constant with temperature. Conversely, at lower temperatures, restricted thermal energy suppresses both charge carrier mobility and polarization, yielding a reduced dielectric constant (ϵ') [32, 33].

3.6 Charge carriers' relaxation analysis

The dielectric permittivity only cannot explain the charge carriers' relaxation process for dielectric materials having considerable DC conductivity contribution. Charge carriers' relaxation and conduction mechanisms can be studied through the framework of Modulus formalism [34]. The complex modulus (M^*) can be articulated as,

$$M^*(\omega) = \frac{1}{\epsilon^*} = M'(\omega) + M''(\omega) \tag{6}$$

Real (M') and imaginary (M'') parts of modulus can be written as follows,

$$M'(\omega) = \frac{\epsilon'(\omega)}{\epsilon'^2(\omega) + \epsilon''^2(\omega)} \tag{7a}$$

$$M''(\omega) = \frac{\epsilon''(\omega)}{\epsilon'^2(\omega) + \epsilon''^2(\omega)} \tag{7b}$$

Fig. 6 shows the M' vs. ω plot for different CTAB concentrations at ambient temperatures. From the figure, it has been observed a very low value of M' towards lower frequency region and almost approaches zero values. For all

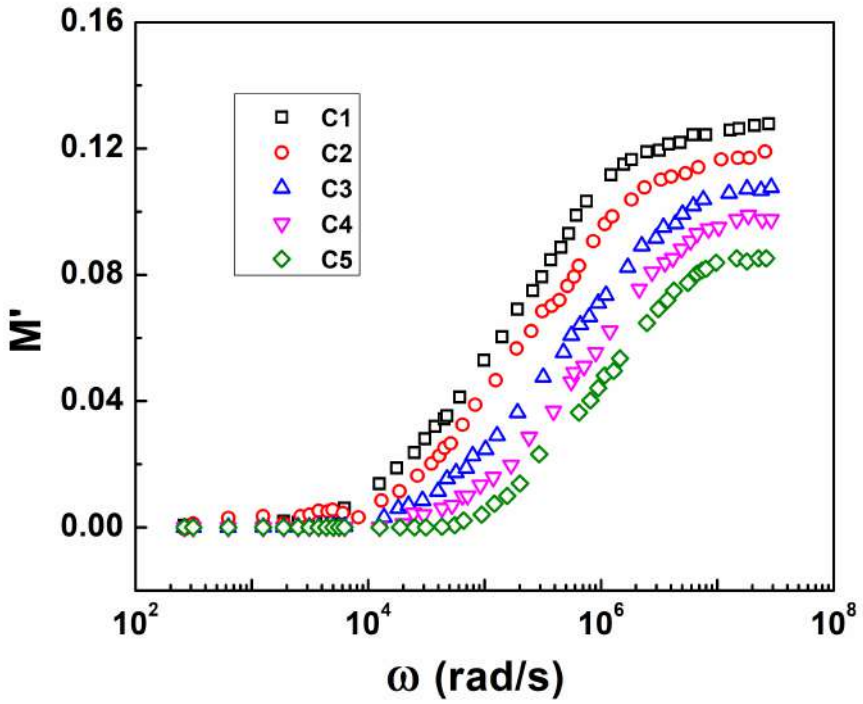

Figure 6: Frequency dependence real modulus (M') for different CTAB concentrations at ambient temperature.

the different CTAB concentrations M' shows a increasing trend with frequency and reach a maximum constant value of M_∞ for frequencies $>$ 107 rad/s. The presence of such behavior indicates that the charge transport is taking place through long-range motion of charge carriers. The frequency dependent imaginary moduli M'' for different CTAB concentrations and for different temperatrures for sample C5 are depicted in Figs. 7(a) and 7(b). From figures 7(a & b) it is observed a distinct charge carriers' relaxation peak has been observed for all the CTAB concentrations and at different temperatures for sample C5 and the relaxation peak shifts towards higher frequency for both the cases. The increase of dc conductivity may be the reason of shifting the relaxation peak towards higher frequency and it can be explained according to the relation [35],

$$\sigma = \frac{\epsilon_o \omega_c}{M''} \tag{8}$$

where ω_c is the relaxation frequency. In modulus formalism, the relaxation peaks corresponding to the switching of DC to AC conductivity under an alternating electric field [36]. The transition from long-range to short-range motion of the charge carriers is represented by the relaxation frequency (ω_c) according to relation $\omega_c \tau_c = 1$, where τ_c is the conductivity relaxation time [37]. The relaxation peak shift toward high frequency side with increasing temperature or dopant concentration suggests a decrease in relaxation time. This indicates the faster response to the external electric field, resulting the enhanced mobility or rapid polarization processes. With increasing temperature, thermal energy facilitates charge-carrier hopping between localized states by reducing potential barriers, thereby improving charge transport. Similarly, increasing CTAB concentration may lead to improved particle dispersion, reduced interfacial polarization, and creation of additional conducting pathways, all of which contribute to higher conductivity and faster relaxation dynamics.

The scaling analysis was carried out for the sample C5 in the measured temperature range of 303-363 K from the plot (M''/M''_{max}) vs. $\log(\omega/\omega_c)$ as shown in Fig. 8. Formation of single master curve suggests that the conductivity relaxation mechanism is temperature independent [38].

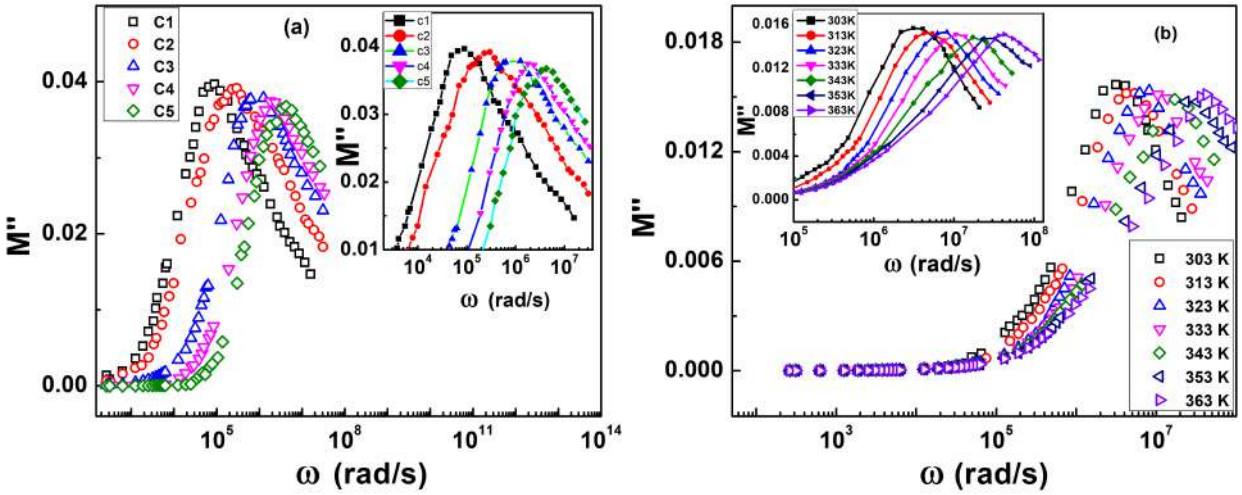

Figure 7: Frequency dependence (a) Imaginary modulus (M'') at ambient temperature for different CTAB concentration and (b) Imaginary modulus (M'') at different temperature for the sample C5.

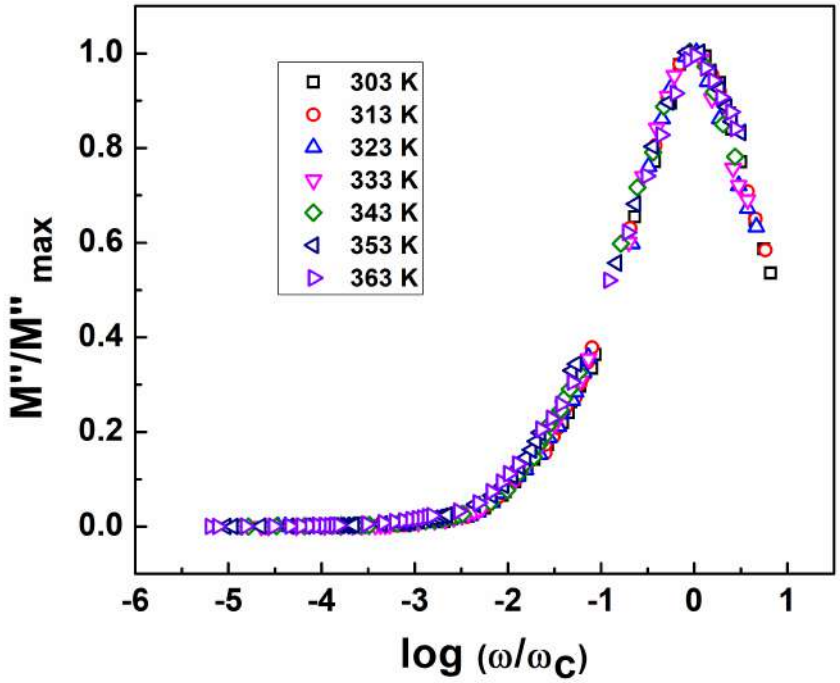

Figure 8: Scaling behavior of imaginary modulus (M'') at different temperature for the sample C5.

3.7 AC conductivity analysis

The ac conductivity can be calculated from the following expression [39],

$$\sigma(\omega) = G(\omega)\frac{d}{A} \tag{9}$$

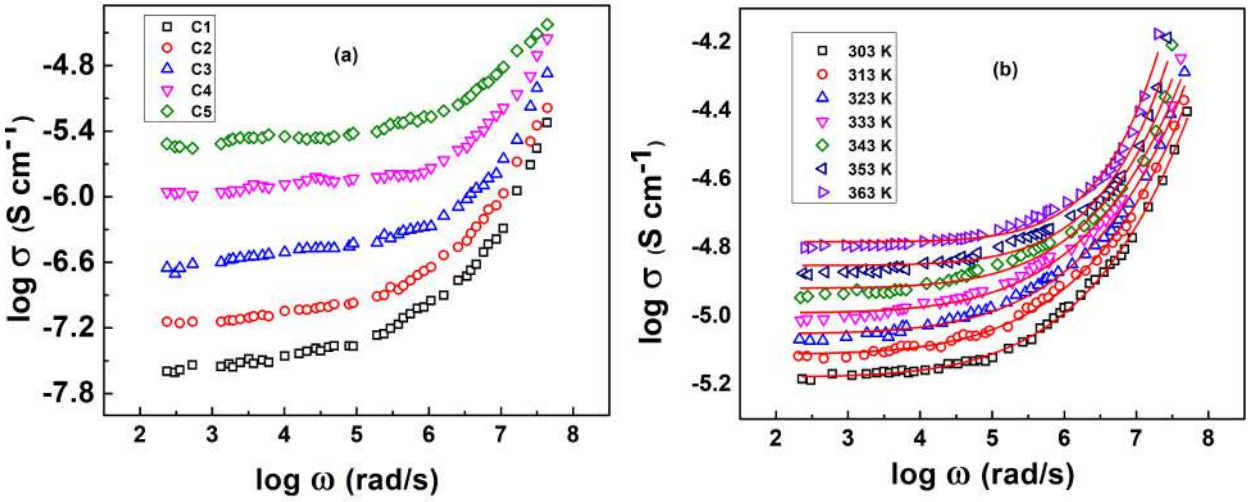

Figure 9: Plot of AC conductivity (a) for different CTAB concentration at ambient temperature and (b) for sample C5 at different temperatures (303 K - 363 K).

Here, $G(\omega)$ represents conductance. Thickness and cross-sectional area of the sample represented by d and A, respectively. Fig.9(a) depict the room temperature frequency-dependent total conductivity for different CTAB concentrations. The AC conductivity shows increasing trend frequency as well as with increasing CTAB concentrations. The total conductivity shows a increasing trend with CTAB concentrations which can be attributed to the enhanced structural ordering in the nanoparticles. Fig.9(b) shows the temperature dependent AC conductivity for sample C5. The frequency independent plateau observed in the lower frequency region arises because of DC conductivity. The shifting of plateau region towards higher frequency suggests the enhancement of DC conductivity [40].

For a particular temperature the $\sigma_{tot}(\omega)$, can be presented as follows,

$$\sigma_{tot}(\omega) = \sigma_o + \sigma(\omega) \tag{10}$$

here σ_o denotes the frequency independent conductivity. $\sigma(\omega)$ increases with frequency for amorphous semiconductor and disordered system, and follows a power law

$$\sigma(\omega) = A\omega^s \tag{11}$$

$$s = \frac{d\ln\sigma(\omega)}{d\ln\omega} \tag{12}$$

where the constant A depends on temperature. The value of frequency exponent s lies within the limit of 0 to 1. The slope $\log\sigma(\omega)$ versus $\log\omega$ plot gives the value of s [40]. For the sample C5 the values of s lie between $0.62 - 0.37$. The conduction mechanisms in disordered systems can be explained with the help of different proposed theoretical models. The behavior of frequency exponent with temperature established the type of conduction mechanism present. The decrease of s with temperature (Fig. 10(a)) implies that the charge transport is taking place through CBH mechanism. This indicates that higher temperatures facilitate carrier hopping between localized states, reducing the effective barrier height. The similar decreasing trends with temperature have been observed for the other samples as well. According to CBH model variation s with temperature is expressed as [41, 42],

$$s = 1 - \frac{6kT}{W_M - kT\ln\left(\frac{1}{\omega\tau_c}\right)} \tag{13}$$

Here W_M and τ_c represents polaron binding energy and characteristic relaxation time, respectively. In the first approximation, Eq. (13) leads to the form,

$$1 - s = \frac{6kT}{W_M} \tag{14}$$

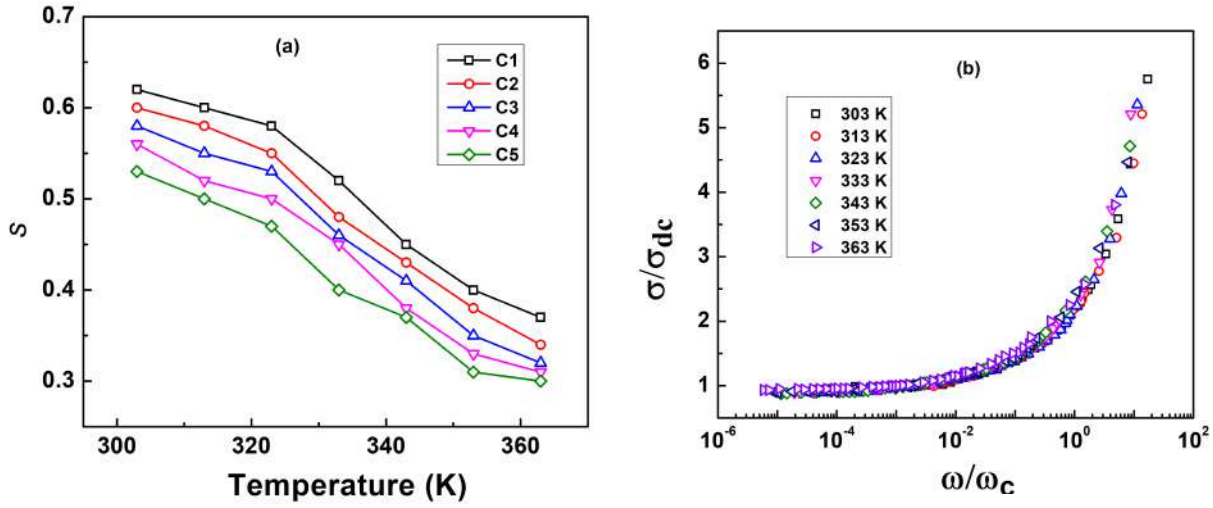

Figure 10: (a) Frequency exponent (s) vs. temperature (T) for the samples C1, C2, C3, C4 and C5 and (b) Scaling behavior of (σ/σ_{dc}) vs. (ω/ω_c) at various temperature for the sample C5.

The calculated values of polaron binding energy (W_M) are tabulated in Table 2. From the obtained values of binding energy it can be ascribed that polarons are the major charge carriers [42]. With increasing temperature, thermally activated carriers hop more easily between localized states due to the reduction of the effective barrier height. The structural modifications caused during synthesis greatly influenced on binding energy. Nanoparticles having higher structural order exhibit lower W_M values. This reduction in W_M suggest the improved of connectivity between the polymer chain networks, which results smaller separation between localized states and reduces the Coulombic interaction barriers. As a result, charge carriers require less activation energy to hop between energetically correlated sites.

Sample name	W_M(eV)
C1	0.41
C2	0.39
C3	0.37
C4	0.35
C5	0.33

Table 2: Values of W_M calculated from the ac conductivity data at 303 K for 100 Hz.

The AC conductivity is a powerful tool for understanding the dynamic processes occurring in solids, particularly in disordered materials. The time-temperature superposition principle (TTSP) plays a key role in understanding these dynamics. The single master curve obtained at different temperature leads to a scaling law known as the time temperature superposition principle [43]. The principle is based on the idea that the system behaves similarly at different temperatures but at different characteristic timescales.

The ac conductivity $\sigma(\omega)$ follows a scaling relation which can be described by the relation [37],

$$\frac{\sigma(\omega)}{\sigma_{dc}} = 1 + \left(\frac{\omega}{\omega_c}\right)^s \tag{15}$$

where, exponent s is a constant and ω_c is the characteristic frequency. This equation predicts that $\sigma(\omega)$ starts to increase as the applied frequency crosses the characteristic frequency ω_c. The values of σ_{dc}, ω_c and s have been obtained from the best fitted curves at different temperatures.

Fig. 10(b) depicts the conductivity master plot of the sample C5 for different temperatures. Here conductivity axis is scaled with respect to σ_{dc} and the frequency axis with respect to the characteristic frequency ω_c. The formation of single master curve (Fig. 10(b)) at different temperatures suggests that conduction mechanism of charge

carriers in the material is independent of temperature, and that the material is governed by universal relaxation processes [44].

4 Conclusions

In summary, we have synthesized PTh nanoparticles by the chemical oxidative polymerization method and dielectric properties are studied with varying frequency and temperature. HRTEM images confirm the formation of well-ordered nanoparticles. The new diffraction peak at $2\theta = 26.6^\circ$ in the XRD pattern at higher CTAB concentration suggest the enhancement of polymer chains ordering. In FTIR spectra the decrease of intensity ratio (I_{sym}/I_{asym}) of the band 1428 and 1631 cm^{-1} for higher CTAB concentration results due to enhancement of conjugation length. The plateau region shift towards higher frequency in the ac conductivity with increasing CTAB concentration and temperature suggest the enhancement of DC conductivity contribution. Imaginary modulus peak shifts towards higher frequency suggest the increase of conductivity. The obtained values of binding energy suggest that polarons are the major charge carriers in this system. The temperature dependent behavior of frequency exponent suggests that the charge transport is taking place through a correlated barrier hopping mechanism

References

[1] A. Javadi, A. Shockravi, M. Koohgard, A. Malek, F. A. Shourkaei, and S. Ando, European Polymer Journal **66**, 328 (2015).

[2] B. C. Roy, M. D. Gupta, L. Bhowmik, and J. K. Ray, Bulletin of Materials Science **24**, 389 (2001).

[3] K. Gupta, P. Jana, and A. Meikap, Synthetic Metals **160**, 1566 (2010).

[4] V. Q. Trung, T. T. T. Duong, N. T. Dua, N. N. Linh, L. D. Cuong, D. P. Thao, V. K. Huy, N. H. H. Phuong, N. Hien, D. K. Linh, V. Q. Manh, N. T. Chinh, T. Hoang, and L. V. Meervelt, Designed Monomers and Polymers **25**, 136 (2022).

[5] N. Asim, S. Radiman, and M. Bin Yarmo, Materials letters **62**, 1044 (2008).

[6] L. Groenendaal, F. Jonas, D. Freitag, H. Pielartzik, and J. R. Reynolds, Advanced materials **12**, 481 (2000).

[7] D. Iarossi, A. Mucci, L. Schenetti, R. Seeber, F. Goldoni, M. Affronte, and F. Nava, Macromolecules **32**, 1390 (1999).

[8] C. Wochnowski and S. Metev, Applied Surface Science **186**, 34 (2002).

[9] J. Shen, M. Kashimoto, T. Matsumoto, A. Mori, and T. Nishino, Polymer Journal **52**, 1273 (2020).

[10] S. S. Gursoy, A. Yildiz, G. C. Cogal, and O. Gursoy, Open Chemistry **18**, 974 (2020).

[11] N. N. Linh, T. T. T. Duong, N. Hien, and V. Q. Trung, Vietnam Journal of Chemistry **58**, 1 (2020).

[12] P. Hedvig, *Dielectric spectroscopy of polymers* (Akademiai Kiado, 1977).

[13] H.-T. Lee, C.-S. Liao, and S.-A. Chen, Die Makromolekulare Chemie: Macromolecular Chemistry and Physics **194**, 2443 (1993).

[14] A. Sunilkumar, S. Manjunatha, Y. Ravikiran, M. Revanasiddappa, M. Prashantkumar, and T. Machappa, Polymer Bulletin **79**, 1391 (2022).

[15] Y. A. Kulakarni, M. Jagadeesh, S. Jambaladinni, H. S. Kumar, M. Vasanthkumar, and S. Shivakumara, Journal of Materials Science: Materials in Electronics **31**, 7226 (2020).

[16] J. G. Raja, M. B. Ahamed, C. M. Hussain, and P. Era, Journal of Materials Science: Materials in Electronics **33**, 22883 (2022).

[17] S. R. P. Gnanakan, M. Rajasekhar, and A. Subramaniaa, International Journal of Electrochemical Science **4**, 1289 (2009).

[18] X. G. Li, J. Li, and M. R. Huang, Chemistry–A European Journal **15**, 6446 (2009).

[19] Y. Li, G. Vamvounis, and S. Holdcroft, Macromolecules **35**, 6900 (2002).

[20] X. G. Li, J. Li, Q. K. Meng, and M. R. Huang, The Journal of Physical Chemistry B **113**, 9718 (2009).

[21] K. Venkateswarlu, A. C. Bose, and N. Rameshbabu, Physica B: Condensed Matter **405**, 4256 (2010).

[22] S. Banerjee and A. Kumar, Journal of Applied Physics **109** (2011).

[23] T. H. de Keijser, J. I. Langford, E. J. Mittemeijer, and A. B. P. Vogels, Journal of Applied Crystallography **15**, 308 (1982).

[24] P. Saini, V. Choudhary, K. Sood, and S. Dhawan, Journal of Applied Polymer Science **113**, 3146 (2009).

[25] B. Warren and B. Averbach, Journal of Applied Physics **21**, 595 (1950).

[26] H. Gao, T. Jiang, B. Han, Y. Wang, J. Du, Z. Liu, and J. Zhang, Polymer **45**, 3017 (2004).

[27] A. Gök, M. Omastová, and A. G. Yavuz, Synthetic Metals **157**, 23 (2007).

[28] M. Akimoto, Y. Furukawa, H. Takeuchi, I. Harada, Y. Soma, and M. Soma, Synthetic Metals **15**, 353 (1986).

[29] F. Ouhib, R. C. Hiorns, R. de Bettignies, S. Bailly, J. Desbrières, and C. Dagron-Lartigau, Thin Solid Films **516**, 7199 (2008).

[30] P. Chutia and A. Kumar, Physica Status Solidi (A) **212**, 2727 (2015).

[31] T. A. Hanafy, Journal of Applied Physics **112**, 034102 (2012).

[32] E. Matveeva, R. Calleja, and V. Parkhutik, Electrochimica Acta **41**, 1351 (1996).

[33] B. G. Soares, M. E. Leyva, G. M. Barra, and D. Khastgir, European Polymer Journal **42**, 676 (2006).

[34] M. M. Ayad and E. A. Zaki, Journal of Applied Polymer Science **110**, 3410 (2008).

[35] M. G. Han and S. S. Im, Journal of Applied Polymer Science **82**, 2760 (2001).

[36] D. Almond, A. West, and R. Grant, Solid State Communications **44**, 1277 (1982).

[37] A. Karmakar and A. Ghosh, Current Applied Physics **12**, 539 (2012).

[38] D. Ray, A. Himanshu, T. Sinha, *et al.*, Indian Journal of Pure and Applied Physics **45**, 692 (2007).

[39] M. H. Harun, E. Saion, A. Kassim, M. Y. Hussain, I. S. Mustafa, and M. A. A. Omer, Malaysian Polymer Journal **3**, 24 (2008).

[40] A. Dey, S. De, A. De, and S. K. De, Nanotechnology **15**, 1277 (2004).

[41] A. K. Himanshu, R. Ray, S. El-Sayed, A. Hassen, S. K. Bandyopadhayay, and T. P. Sinha, Radiation Effects and Defects in Solids **169**, 73 (2014).

[42] S. Elliott, Advances in Physics **36**, 135 (1987).

[43] J. C. Dyre and T. B. Schrøder, Rev. Mod. Phys. **72**, 873 (2000).

[44] P. K. Karahaliou, N. Xanthopoulos, C. A. Krontiras, and S. N. Georga, Physica Scripta **86**, 065703 (2012).